UNIVERSITY OF OKLAHOMA

GRADUATE COLLEGE

EXPERIMENTAL STUDY OF PROPPANT PACK DEFORMATION

A THESIS

SUBMITTED TO THE GRADUATE FACULTY

in partial fulfillment of the requirements for the

Degree of

MASTER OF SCIENCE

By

SHANTANU TANEJA
Norman, Oklahoma
2016

EXPERIMENTAL STUDY OF PROPPANT PACK DEFORMATION

A THESIS APPROVED FOR THE
MEWBOURNE SCHOOL OF PETROLEUM AND GEOLOGICAL ENGINEERING

BY

Dr. Chandra Rai, Chair

Dr. Carl Sondergeld, Co-Chair

Dr. Deepak Devegowda

Dedicated to papa and sunny bhaiya

Acknowledgements

First and foremost, my head bows down humbly for my Father, Mr. P.K. Taneja without whose support and belief in my abilities I could not have taken my first step towards the Master's degree. All these years my brother, Rajat, was my messiah with his love and endurance. All my near and dear ones contributed, in their unique way, to keep me motivated to complete this course, step by step, successfully.

No words could best describe my heartfelt gratitude to my advisors, Prof. Chandra Rai and Prof. Carl Sondergeld, for their time and guidance during the course of my thesis at OU. They have provided me with immense opportunities to learn and constant encouragement to achieve higher. I would not have completed the project without their strong support. They have been a source of inspiration for me to reach my goals. Furthermore, they have not only made me grow academically but personally too. I would also like to sincerely thank Prof. Devegowda for his guidance during my studies.

I take this opportunity to express my sincere thanks to my IC^3 colleagues - Dr. Mark Curtis, Bruce Spears, Gary Stowe, Jeremy Jernigen, Micaela Langevin, Ali Tinni, Wyatt Wick and Anthony Ndunda for their help to run the machines efficiently at all times. I appreciate the support of Akash Damani for providing the much needed help on data. It has been a great pleasure to work with all. I also thank the Unconventional Shale Gas and Experimental Rock Physics Consortia members for their invaluable suggestions to improve my project work and financial support for making this research possible.

Thanks to my pillars of support and strength on whom I could lean to rest and revive - my friends: Deep, Dongre, Dhanya, Himanshu, Janny, Jyot, Maulin, Rohit, Sami, Sarvesh, Shreya and Vineet for their continued support during the course of my stay in Norman. They indeed made my stay delightful and enjoyable.

Once again thanks to all the above mentioned for being there for me! Also, to all those whom I may have inadvertently overlooked to mention here.

Table of Contents

Acknowledgements iv

List of Tables ix

List of Figures x

Abstract xxi

Chapter 1: Introduction to Proppant Crushing 1

1.1 Overview 1

1.2 Objectives of the research 1

1.3 Mechanisms for conductivity reduction 2

1.4 Proppant crush test 3

1.4.1 Introduction 3

1.4.2 API crush test 4

1.4.3 Single particle crush test 13

1.4.4 Constant displacement rate crush test 13

1.5 Proppant percent crush and permeability 16

1.6 Problem statement 17

Chapter 2: Experimental Procedure 18

2.1 Introduction 18

2.2 Vibratory sieve shaker 19

2.3 Low pressure pycnometer (LPP) 20

2.4 Crush test 20

2.5 Laser particle size analysis 24

Chapter 3: Dry Proppant Crush Test 26

3.1 Introduction 26

3.2 Experimental apparatus 26

3.3 Effect of hold time 28

3.4 Overview of crush test analysis 30

    3.4.1 Results 30

    3.4.2 Discussion 35

3.5 Effect of proppant concentration 45

    3.5.1 Results 45

    3.5.2 Discussion 54

    3.5.3 Investigation of repeatability 54

3.6 Effect of displacement rate 57

3.7 Effect of proppant type 60

3.8 Effect of cyclic loading 66

    3.8.1 Results 66

    3.8.2 Discussion 69

3.9 Effect of fracture morphology 69

    3.9.1 Motivation 69

    3.9.2 Crush cell modification 72

    3.9.3 Results 72

3.10 Summary 79

Chapter 4: Wet Proppant Crush Test 80

4.1 Introduction 80

4.2 Motivation 80

4.3 Effect of saturation ... 84
4.3.1 Crush cell modification ... 84
4.3.2 Test matrix ... 86
4.3.3 Experimental procedure ... 86
4.3.4 Results ... 88
4.4 Effect of pre-test treatment ... 91
4.4.1 Experimental Apparatus ... 91
4.4.2 Test matrix ... 92
4.4.3 Experimental procedure ... 92
4.4.4 Results ... 92
4.5 Summary ... 97
Chapter 5: Conclusions ... 98
Application to the Industry ... 99
References ... 102

List of Tables

Table 1: API and Modified API crush test conducted at closure stress of (a) 6000 psi and (b) 7500 psi (Freeman et al., 2009). LWC stands for light weight ceramic and IDC stands for intermediate density ceramic. 12

Table 2: Test matrix for the crush test showing the proppant type and displacement rate used for 3 different concentrations of 20/40 mesh Ottawa sand: 1, 2 and 4 lb/ft^2. 45

Table 3: Test matrix for the crush test showing the proppant type and displacement rates used for 3 different concentrations of 20/40 mesh Ottawa sand: 1, 2 and 4 lb/ft^2. 57

Table 4: Stress state for triaxial hydraulic fracturing test performed on Tennessee sandstone. Stresses are color coded to compare with arrows showing orientation of stresses in figure 54 (Damani, 2015). 71

Table 5: Test matrix for the crush test showing the proppant type and Δ used for 3 different concentrations of 20/40 mesh Ottawa sand: [1] and [4]. 72

Table 6: Test conditions used by Ghosh et al. (2013) to track silicon ion concentration as function of time. St.* - refers to stainless steel. 82

Table 7: Test matrix for the crush test showing the proppant type and displacement rate used for 3 different concentrations of 20/40 mesh Ottawa sand: 1 lb/ft^2 and 4 lb/ft^2. ... 92

List of Figures

Figure 1: Effect of various mechanisms on proppant pack conductivity reduction of Jordan sand and lightweight ceramic. Several mechanisms can reduce effective conductivity to less than 2% of API experimental test values (Palisch et al., 2007). 3

Figure 2: Comparison of percent crush reported by 11 laboratories on 16/30 brown sand at 4000 psi (Palisch et al., 2009). Percent crush varied from as low as 6% to as high as 25%. 5

Figure 3: Weight percent crushed particles for various proppants at different concentrations at 6000 psi (adapted from Howard and Fast, 1970). Note the significant difference (factor of 5) in percent crush between API crush test at concentration of 4 lb/ft^2 and monolayer of proppant, 0.25 lb/ft^2 concentration. 6

Figure 4: Conductivity at 2000 psi as function of median particle diameter (MPD) of ceramic proppants at concentration of 2 lb/ft^2 concentration – light weight ceramic (LWC), intermediate density ceramic (IDC) and bauxite ceramic (BC) (Schubarth et al., 2004). Higher median particle size corresponds to higher conductivity. 8

Figure 5: Conductivity as function of closure stress for different proppants at concentration of 2 lb/ft^2 - sand, light weight ceramic (LWC), intermediate density ceramic (IDC) and bauxite ceramic (BC) (Schubarth et al., 2004). Numbers within parenthesis indicate median particle size (mm). 8

Figure 6: For 20/40 mesh sand (a) particle size distribution as function of stress (b) changes in mass of sieve size at different stresses with respect to that of unstressed

proppant. Note the significant change in sieve size distribution at ≈ 5000 psi (Schubarth et al., 2004). 10

Figure 7: Retained median particle diameter (MPD) as function of closure stress and stress cycles for 20/40 mesh sand with median particle diameter of 0.52 mm (Schubarth et al., 2004). Schubarth et al., (2004) made a note that there is a poor test result at 6000 psi for 5 stress cycles and it needed to be rerun. 11

Figure 8: Experimental setup used by Freeman et al., (2009) to conduct testing using liquid saturated proppant at significantly high temperature. 12

Figure 9: Plot of the applied pressure derivative as function of time for RCS is divided into three regions: A) movement and grain rearrangement, B) grain crushing and C) grain rearrangement (Simo et al., 2013). 15

Figure 10: Plot of failure pressure as function of proppant concentration for 4 different proppants (Simo et al., 2013). Increasing proppant concentration is directly correlated with failure pressure. 16

Figure 11: Long term fracture conductivity as function of percent crush for 30/50 and 40/70 intermediate density ceramics and low density ceramics from various manufactures (Palisch et al., 2015). 17

Figure 12: Restch AS 200 vibratory sieve shaker with 2 sieves and a pan. The sieves are 20 and 45 mesh. 19

Figure 13: Micrometrics model II LPP Helium pycnometer for measuring proppant grain density. 20

Figure 14: MTS-312, 21 load frame with load cell and axial piston to perform crush tests 21

Figure 15: (a) Schematic cross-section of crush cell. (b) Left: Crush cell with fused silica window attached and acoustic emission sensor mounted. Microscope camera used is also shown. Right: Fused silica window is shown with a microscope image of [4] of 20/40 mesh Ottawa sand. 23

Figure 16: Modified crush cell in use. Pore fluid inlet, microscope camera, upper piston and fused silica window are also been shown. 24

Figure 17: Beckman Coulter LS 13 320 Tornado Dry Power System is used to measure the particle size distribution (particle size range varies from 0.37 to 2000 μm). 25

Figure 18: Crush cell used to study dry proppant crushing. AE transducer, microscope camera and upper piston are also shown. 27

Figure 19: Steps for assembling the crush cell-1: Schematic cross-section of crush cell. 2 and 3: Fused silica window clamped to the outside of crush cell. 4: Bottom steel face is inserted from top of crush cell. 5: Proppant is poured into the cell. 6: Upper steel face and piston is inserted. 27

Figure 20: (a) Plot of pressure (dash) and AE rate (solid) as function of time. Pressure is increased to 15000 psi and held constant for 2 minutes. (b) Magnified plot of the 2 minutes hold time region. AE rate is minimal indicating minimal crushing and rearangement. 29

Figure 21: Particle size analysis as function of pressure. σ_{crit} of concentration of 4 lb/ft^2 of 20/40 mesh Ottawa sand is 5500 psi. 31

Figure 22: Plot of pressure (line) and AE rate (square) as function of time. Red line indicates σ_{crit} for concentration of 4 lb/ft^2 of 20/40 mesh Ottawa sand. 32

Figure 23: Plot of pressure (line) and loading rate (square) as function of time. Red line indicates σ_{crit} for concentration of 4 lb/ft^2 of 20/40 mesh Ottawa sand. 32

Figure 24: Microscopic images as function pressure. Crushing starts at 6000 psi which is in accordance with particle size analysis results. Additionally, crushing is non-uniform and primarily concentrated at steel-proppant interface. 33

Figure 25: Proppant width (square) calculated from the images and computed proppant pack porosity (diamond) from the measured width are plotted as function of pressure. 34

Figure 26: Conductivity reduction as function of pressure. Conductivity reduced rapidly after 6000 psi as 20/40 mesh Ottawa sand reaches its σ_{crit}. 35

Figure 27: Three major types of hydrostatic compression behavior (Brace et al., 1978; Zhang et al., 1990). 36

Figure 28: (a) Plot of pressure as function of ΔF_c. ΔF_c represents change in width and is comparable to volume strain. (b) Characteristic hydrostatic compression for highly porous sandstones. Region indicating grain crushing and collapse is similar to that observed in (a) (Issen, 2000). 37

Figure 29: Grain-grain contact forces for: (a) isotropic loading and (b) anisotropic loading. Homogenous case has constant stiffness particles while heterogeneous case has particles of 4 different stiffnesses (Wong et al., 2004). 39

Figure 30: Grains are packed hexagonally. a) Hydrostatic load, P. b) $P_1 >> P_2$. 20/40 Ottawa sand is investigated under condition (b) where $P_1 >> P_2$ (Gallagher et al., 1974). 40

Figure 31: Fringe patterns for an interior grain as function of applied load. P_1 is applied vertically with P_2 applied horizontally. Expected fracture pattern is predicted: a) cubic b) hexagonal packing (Gallagher et al., 1974). 41

Figure 32: Acoustic emission (AE) rate and porosity change as function of effective pressure (Zhang et al., 1989). Porosity change and AE rate are well correlated. (1 MPa = 145.04 psi)... 43

Figure 33: Pore-volume strain as function of confining pressure. Note the hysteresis in pore-volume strain and the sudden increase in pore volume strain at the onset of grain crushing at 600 bars (8702.2 psi) (Zoback and Byerlee, 1976). (1 bar = 14.504 psi).... 43

Figure 34: Plot of permeability and porosity for host rock and bed parallel bands. Host rock permeability is 3 order more than permeability of bands (Aydin and Ahmadov, 2009).. 44

Figure 35: (a) Particle size analysis as function of pressure for concentration of 1 lb/ft^2. σ_{crit} is 2500 psi. (b) Loading rate (circle) and AE rate (line) as function of pressure. Red line indicates σ_{crit} for concentration of 1 lb/ft^2 of 20/40 mesh Ottawa sand.................. 48

Figure 36: (a) Particle size analysis as function of pressure for concentration of 2 lb/ft^2. σ_{crit} is 4000 psi. (b) Loading rate (circle) and AE rate (line) as function of pressure. Red line indicates σ_{crit} for concentration of 2 lb/ft^2 of 20/40 mesh Ottawa sand.................. 49

Figure 37: (a) Particle size analysis as function of pressure for concentration of 4 lb/ft^2. σ_{crit} is 5500 psi. (b) Loading rate (circle) and AE rate (line) as function of pressure. Red line indicates σ_{crit} for concentration of 4 lb/ft^2 of 20/40 mesh Ottawa sand.................. 50

Figure 38: Percent crush as function of pressure and concentration of 20/40 mesh Ottawa sand. Percent crush is less at concentration of 4 lb/ft^2 in comparison to percent

crush at concentration of 1 and 2 lb/ft^2. Note fines start to be generated at higher pressure with increased concentration. 51

Figure 39: Loading rate as function of load for two different concentrations – concentration of 1 and 4 lb/ft^2. Notice the pressure at which loading rate starts to decrease is different for two concentrations. 51

Figure 40: Microscope images of concentration of 1 and 4 lb/ft^2 at 15000 psi. Crushing is uniform in case of concentration of 1 lb/ft^2. Crushing is non-uniform and primarily concentrated at steel-proppant interface for concentration of 4 lb/ft^2. 52

Figure 41: Compaction and porosity reduction as function of pressure for concentration of (a) 1 lb/ft^2 (b) 4 lb/ft^2. Compaction and porosity reduction is greater for concentration of 1 lb/ft^2 than 4 lb/ft^2. 53

Figure 42: Loading rate as function of time for three different concentrations: (a) 1 lb/ft^2, (b) 2 lb/ft^2 and (c) 4 lb/ft^2. The test is quite repeatable for the three concentrations. 55

Figure 43: Loading rate as function of load for three different concentrations: (a) 1 lb/ft^2, (b) 2 lb/ft^2 and (c) 4 lb/ft^2. The test is quite repeatable for the three concentrations (± 300 psi). 56

Figure 44: (a) Loaded particle size analysis as function of pressure for concentration of 2 lb/ft^2 of 20/40 mesh Ottawa sand at $\Delta_{11.5}$. σ_{crit} is 4000 psi. (b) Loading rate (circle) and AE rate (line) as function of time at $\Delta_{11.5}$. Red line indicates σ_{crit} for concentration of 2 lb/ft^2 of 20/40 mesh Ottawa sand. 58

Figure 45: (a) Loaded particle size analysis as function of pressure for concentration of 4 lb/ft^2 of 20/40 mesh Ottawa sand at $\Delta_{11.5}$. σ_{crit} is 5500 psi. (b) Loading rate (circle) and

AE rate (line) as function of time at $\Delta_{11.5}$. Red line indicates σ_{crit} for concentration of 4 lb/ft^2 of 20/40 mesh Ottawa sand. 59

Figure 46: (a) Loading rate (circle) and AE rate (line) as function of time for CarboNRT proppant at concentration of 2 lb/ft^2. Loading rate just starts to decrease at σ_{crit} = 5000 psi. (b) Particle size analysis at 15000 psi and native proppant for CarboNRT. Fines start generating well before 15000 psi. At 15000 psi, the mean particle size reduces from 791 μm to 577 μm.......... 62

Figure 47: (a) Loading rate (circle) and AE rate (line) as function of time for Ottawa sand at concentration of 2 lb/ft^2. Loading rate starts to decrease at σ_{crit} ≈ 4000 psi. (b) Particle size analysis at 15000 psi and native proppant for Ottawa sand. Fines start generating well before 15000 psi. At 15000 psi, the mean particle size reduces from 678 μm to 442 μm. 63

Figure 48: (a) Loading rate (circle) and AE rate (line) as function of time for CarboHSP proppant at concentration of 2 lb/ft^2. Loading rate just starts to decrease at σ_{crit} ≈ 14000-14500 psi. (b) Particle size analysis at 15000 psi and native proppant for CarboHSP. Fines start generating around 14000 psi. 64

Figure 49: (a) Loading rate (circle) and AE rate (line) as function of time for CarboProp proppant at concentration of 2 lb/ft^2. Loading rate just starts to decrease at σ_{crit} ≈ 14000-14500 psi. (b) Particle size analysis at 15000 psi and native proppant for CarboProp. Fines start generating around 15000 psi. 65

Figure 50: Load and AE rate as function of time at concentration of 2 lb/ft^2 of 20/40 mesh Ottawa sand. Dotted blue represents pressure increase to 15000 psi, then decrease to 15000 psi and then, increase to 15000 psi at constant $\Delta_{11.5}$. Solid blue is AE rate

corresponding to dotted blue. Dashed green represents increase in load to 15000 psi on the proppant pack in which crushed proppant was taken out of crush cell and mixed. Solid green is AE rate corresponding to dashed green. 68

Figure 51: Particle size distribution for post-test proppant (concentration of 2 lb/ft^{2}of 20/40 mesh Ottawa sand) obtained at “1”, “2” and “3” compared to native particle size distribution. Proppant is significantly crushed at “1” compared to native proppant size distribution. No significant difference in proppant crushing in post-test proppant obtained at “1”, “2” and “3”. 68

Figure 52: Retained median particle diameter (MPD) as function of closure stress and stress cycles for 20/40 mesh sand with MPD of 0.52 mm(Schubarth et al., 2004)........ 69

Figure 53: Schematic of a hydraulic fracture with mating surface showing exaggerated roughness (adapted from Kassis and Sondergeld, 2010). Width varies along the fracture causing proppant concentration variation... 70

Figure 54: SEM image of hydraulically fractured Tennessee sandstone Left: 32 mm away from the injection borehole. Fracture with is fairly uniform. Right: 25 mm away from center of injection. Fractured quartz grains obstructing the flow path of proppant (Damani, 2015)... 71

Figure 55: Left: Dry Tennessee sandstone with arrows indicating stress orientation and injection borehole (thicker arrows = σ_H, smaller arrows at 45^o indicate a fluid pressure = σ_h). Hydraulic fracture is visible. Right: Fracture width as function of distance away from injection borehole. Fracture width varies from 46.5 µm to 3.3 µm (Damani, 2015). 71

Figure 56: Modified crush cell piston to test proppant crushing when proppant concentration is variable. Thickness in middle is 4 times the mean diameter of 20/40 mesh Ottawa sand (≈700 µm). 73

Figure 57: Loading rate (circle) and AE rate (line) as function of time for concentration of: (a) 1 lb/ft^2 and (b) 4 lb/ft^2. Duration of the test is longer with increase in proppant concentration. 74

Figure 58: For concentration of 1 lb/ft^2, comparison of curved face and flat face responses for: (a) loading rate as function of time (b) particle size analysis at 3000 psi (c) particle size analysis at 5000 psi (d) particle size analysis at 9000 psi. 76

Figure 59: For concentration of 4 lb/ft^2, comparison of curved face and flat face responses for: (a) loading rate as function of time, (b) particle size analysis at 5000 psi and (c) particle size analysis at 9000 psi. 77

Figure 60: Microscope images as function of pressure for a curved piston: Top – 1 lb/ft^2 and Bottom – 4 lb/ft^2. Crushing for both concentration of 1 and 4 lb/ft^2 is non-uniform and concentrated at steel-proppant interface and in the region where proppant concentration is the lowest and stresses are the greatest. 78

Figure 61: Petrophysical and mechanical properties of Barnett shale used to study long-term proppant pack conductivity. Shale 1 is carbonate-rich and shale 2 is clay-rich. Shale 2 has relatively higher porosity and lower Total Organic Carbon (TOC) (Ghosh et al., 2013). 81

Figure 62: Silicon ion concentration as function of time for (a) Test 1 (b) Test 2. Concentration stabilizes for the tests in the long run (Ghosh et al., 2013). 82

Figure 63: Illustration of pressure solution and compaction mechanism. High stresses at grain-grain contact leads to dissolution of silica and then precipitation in pore space leading to reduction in porosity (Weaver et al., 2009). 83

Figure 64: Pressure solution and compaction model simulation to obtain porosity loss in quartz pack as a function of time (Lee et al., 2009). 83

Figure 65: Modified crush cell in use. Pore fluid inlet, microscope camera, upper piston and window are shown. 84

Figure 66: Steps for assembling the modified crush cell. Teflon seal and sealant was used to minimize fluid leakage. 1: Schematic cross-section of crush cell. 2: Bottom steel face is inserted. 3: Upper piston and face with teflon seal is inserted 4: Proppant is poured from the side. 5: Sealant is applied. 6 and 7: Fused silica window is clamped to outside of crush cell. 8: Axial pressure is increased to 2000 psi. 9: Pore pressure is increased to 50 psi using distilled water. 85

Figure 67: Particle size distribution for unstressed proppant and dry proppant at concentration of 4 lb/ft^2 of 20/40 mesh Ottawa sand with the $\Delta_{3.8}$ at 3000 psi. No significant difference in particle size distribution. 86

Figure 68: Microscope images as function axial load and pore pressure. 1 and 2 are captured as function of axial load increase. The proppant pack underwent compaction with increase in axial load. 3, 4 and 5 are captured as function of increase in pore pressure. 6 confirms uniform distribution of pore fluid at 50 psi. Minimal crushing, marked by red circles, is observed at 8000 psi. 87

Figure 69: Pressure (dash) and AE rate (solid) as function of time. Pore pressure was increased to 50 psi when the axial load was maintained stable at 2000 psi. AE rate is found to be minimal compared to dry proppant experiments.. 88

Figure 70: Loading rate as function of load for tests conducted dry and saturated at concentration of 4 lb/ft^2. For test conducted saturated, loading rate does not show significant variation as function of load. 89

Figure 71: Compaction for dry and saturated tests at concentration of 4 lb/ft^2. Trends are significantly different and may be attributed to reduced friction at grain to grain contacts in saturated test. 90

Figure 72: Particle size distribution for dry and saturated test at concentration of 4 lb/ft^2. Very little difference between saturated and dry crush tests particle size...................... 91

Figure 73: Container filled with 20/40 mesh Ottawa sand and distilled water used to study pre-test treatment effects. 93

Figure 74: Loading rate (circle) and AE rate (line) as function of time for treated proppant at concentration of (a) 1 lb/ft^2 (b) 4 lb/ft^2. 94

Figure 75: For concentration of 1 lb/ft^2, comparison of treated and dry proppant test responses for: (a) loading rate as function of time (b) particle size analysis at 5000 psi and (c) particle size analysis at 9000 psi. 95

Figure 76: For concentration of 4 lb/ft^2, comparison of treated and dry proppant test responses for: (a) loading rate as function of time (b) particle size analysis at 5000 psi and (c) particle size analysis at 9000 psi. 96

Abstract

Unconventional reservoirs, especially shales are drilled horizontally and hydraulically fractured for economical production. Proppant is carried and placed with the use of fracturing fluid to maintain fracture conductivity once the fracture is initiated. It has been observed that fracture conductivity degrades overtime due to several mechanisms such as proppant crushing, embedment, diagenesis and fines migration. To evaluate the performance of various proppants under reservoir stress conditions, American Petroleum Institute (API) proposed the proppant crush test, where load rate is maintained constant, to determine amount of fines generated in terms of "percent crush" by weight. However, the current standard procedure to measure crush resistance of proppants does not represent the realistic field conditions as it is based on measurement at high proppant concentration (4 lb/ft^2), ambient temperature and dry condition.

To study the proppant behavior under stress, we conducted experiments at constant displacement rate to determine the critical pressure of a proppant pack with the aid of acoustic emission activity detection and particle size analysis. Critical pressure (σ_{crit}) is defined as the pressure at which particles finer than the specified proppant size distribution start being generated as determined through particle size analysis**.** This is also the pressure for onset of grain crushing. In addition to acoustic emission activity and particle size analysis, images of proppant were captured as function of pressure. With the help of bulk density, grain density and images, porosity was calculated as function of pressure. Proppants used in this study are 20/40 mesh Ottawa sand and 20/40 mesh ceramic proppants: carboHSP, carboNRT and carboProp.

Our objective is to systematically study the effects of proppant concentration, fracture morphology, proppant type, cyclic loading, saturation and pre-test treatment on σ_{crit} of the selected common proppants.

When proppant is tested dry and at ambient temperature, it is observed that loading rate, calculated from load data, and acoustic emission activity rate as function of load and time provide an indication of σ_{crit}. σ_{crit} depends on proppant concentration, proppant type and displacement rate. It is observed for dry 20/40 mesh Ottawa sand that higher proppant concentration is correlated with a higher σ_{crit}. For 4 lb/ft^2 concentration, images of dry 20/40 mesh Ottawa sand captured as function of pressure show that crushing is non-uniform and primarily takes place at the steel-proppant interface. For 1 lb/ft^2 concentration, images show that crushing is uniform. Using images for the dry 4 lb/ft^2 concentration of 20/40 mesh Ottawa sand, we calculate a porosity reduction of 25% and proppant pack conductivity reduction of 14% due to compaction with pressure increase to 13000 psi. Similarly for the dry 1 lb/ft^2 concentration of 20/40 mesh Ottawa sand, we observe porosity reduction of 33% and conductivity reduction of 18% due to compaction to a pressure of 13000 psi. We conclude that higher proppant concentration corresponds to less porosity and conductivity reduction.

To understand the effect of fracture morphology on proppant crushing, the crush cell piston was modified so as to obtain differential proppant concentration as function of crush cell width. This study was motivated by observation of changes in fracture width on hydraulically fractured Tennessee sandstone under triaxial conditions in laboratory.

Loading rate as function of load indicates that differential concentration of dry 20/40 mesh Ottawa sand shows relatively low crush resistance in comparison to uniform concentration of dry 20/40 mesh Ottawa sand. Particle size analysis performed at discrete pressures supports our inferences from loading rate as function of load. Images for dry 4 lb/ft^2 concentration of 20/40 mesh Ottawa sand indicate that crushing is non-uniform and primarily takes place at steel-proppant interface and the region where the proppant concentration is relatively low and stress is relatively high. For dry 1 lb/ft^2 20/40 mesh Ottawa sand, crushing is non-uniform and primarily takes place in the region where the proppant concentration is relatively low and grain to grain stresses are relatively high. These observations indicate that fracture width modulation would play a role in differential crushing of proppant, thereby, affecting fracture conductivity.

Proppant crush tests were further extended to study the effect of cyclic loading on dry 20/40 mesh Ottawa sand. This study was conducted to investigate the effect of re-fracturing or well shut-in which would cause stress cycling on the already placed proppant pack in the reservoir. Cyclic loading experiment is conducted on dry 4 lb/ft^2 concentration of 20/40 mesh Ottawa sand after it is subjected to 15000 psi twice at constant displacement rate. Acoustic emission activity rate as function of time indicates that proppant pack does not undergo crushing in the 2nd cycle when the proppant pack has already been subjected to 15000 psi in the 1st cycle. Using particle size analysis conducted at the end of 1st and 2nd cycle, it is concluded that stress cycling does not significantly increase crushing.

The proppant crush cell was further modified to conduct the test on fluid saturated proppant packs. The apparatus was connected to metering pump to maintain a pore pressure of 50 psi on 4 lb/ft^2 concentration of 20/40 mesh Ottawa sand while stress on proppant pack was increased to 11000 psi at constant displacement rate. Imaging showed uniform fluid distribution in pores at 50 psi. Loading rate and acoustic activity rate as function of time and load were inconclusive. Particle size analysis indicated that 20/40 mesh Ottawa sand crushed, and, there was insignificant difference in particle size distribution at 11000 psi between dry 4 lb/ft^2 concentration of 20/40 mesh Ottawa sand and 20/40 mesh Ottawa sand exposed to fluid. However, there was significant effect of reduction in frictional resistance between grain-grain contact which led to a significant change in the compaction trend between wet and dry tests.

To investigate the effect of exposure to high temperature fluids on proppant crushing, 20/40 mesh Ottawa sand was exposed to distilled water for 3 days at 100 ^{o}C. The 20/40 mesh Ottawa sand was then dried and crush test was performed on this heat and water treated proppant. Loading rate as function load indicates that treated 20/40 mesh Ottawa sand at 1 lb/ft^2 concentration shows significantly less crush resistance in comparison to test conducted on dry 20/40 mesh Ottawa sand. However, particle size distribution at 9000 psi of untreated and treated proppant at higher concentration of 4 lb/ft^2 showed relatively small differences. Loading rate data showed no significant difference between treated and untreated proppant.

In conclusion, we propose a new proppant crush test procedure which honors realistic field conditions i.e. low proppant concentration, uneven surface topography and fluids at elevated temperature. The standard API crush test overestimates fracture conductivity. Observing loading rate and acoustic emission activity rate as function of load while conducting test at constant displacement rate is recommended.

Chapter 1: Introduction to Proppant Crushing

1.1 Overview

Objectives of the study are defined in the next section. **Section 1.3** reviews various mechanisms of proppant pack conductivity reduction. Previous efforts are reviewed in **Section 1.4**. Three different methodologies for proppant crush tests are reviewed in detail. It should be noted that all the crush tests are conducted on dry proppant packs, i.e. proppant pack not exposed to pore fluid. The test proposed by American Petroleum Institute (API) is used as a benchmark by the industry to compare various proppants and to infer performance in terms of crushing. **Section 1.5** reviews the literature relating proppant crush tests to fracture conductivity. The last section (**Section 1.6**) defines the problem statement for the study. In the remainder of this thesis, concentration of proppant is represented with the symbol [], for example, [4] would refer to 4 lb/ft^2 concentration.

1.2 Objectives of the research

The principle goal of this study was to systematically study the effect of proppant concentration, fracture morphology, cyclic loading, saturation and pre-test treatment on proppant behavior under stress. To delineate further, the objectives of the research are:

a) To review different proppant crush tests proposed by various researchers.
b) To develop a methodology to determine critical pressure or onset of grain crushing with performing post-test sieving.
c) To validate a new proposed methodology using particle size analysis, imaging and studies conducted by previous researchers.

d) To recommend changes to the current practices for proppant crush testing.

1.3 Mechanisms for conductivity reduction

Fracture conductivity can degrade over time through several mechanisms. One of the mechanisms that contributes to this decrease in fracture conductivity is proppant crushing. Additionally, proppant embedment (Guo et al., 2012), diagenesis (LaFollette and Carman, 2010; Weaver et al., 2007; Duenckel et al., 2012; Ghosh et al., 2013) and fine migration are other mechanisms that affect the proppant pack conductivity. Guo et al., (2012) and Wick, (2015) studied the reduction in formation conductivity by formation creep. Palisch et al., (2007) investigated multiphase flow, inertial flow, gel damage, fines migration and cyclic loading, and suggested that these can reduce effective conductivities to less than 2% of API experimental test values. They also showed that lower proppant concentration, i.e. < [2.25] which is recommended by API, would cause reduction in conductivity. Throughout this thesis, I will use the symbol [x] to represent the x lb/ft^2 proppant concentration. **Figure 1** shows simulated cumulative reduction in conductivity summarized by Palisch et al., (2007).

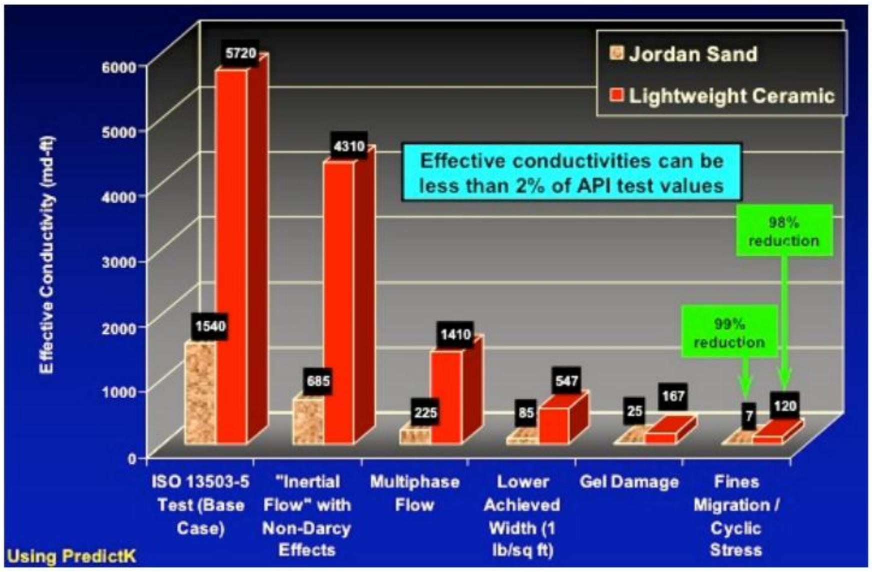

Figure 1: Effect of various mechanisms on proppant pack conductivity reduction of Jordan sand and lightweight ceramic. Several mechanisms can reduce effective conductivity to less than 2% of API experimental test values (Palisch et al., 2007).

1.4 Proppant crush test

1.4.1 Introduction

The API crush test was established to evaluate proppant crushing through a measure called "percent crush" by weight (Palisch et al., 2009; Simo et al., 2013). API suggested that the test should be conducted at high proppant concentration and ambient temperature which are far removed from realistic field conditions (Palisch et al., 2009). Raysoni et al., (2013) proposed single particle crush test primarily used in ceramic industry and showed its application to study crush strength of proppant. However, a single particle crush test would not be able to encompass effects of multiple layers of proppant, thereby, limiting its use to studying crush strength of monolayer of proppant. Higher concentrations of proppant enables better stress distribution among individual proppant particles. Simo et al., (2013) studied proppant crush strength using a different methodology of increasing the load at constant displacement rate rather than constant load rate as suggested by the API. Simo et al., (2013) indicated that proppant behavior under stress could be studied from the load data by calculating loading rate but did not validate this inference by analyzing particle size post-test.

1.4.2 API crush test

API proposed the crush test (API RP 56; ISO 13503-2) to estimate the fines generated under specific uniaxial stress conditions in terms of “percent crush” by weight. The methodology as proposed by API is as follows:

(I) in order to ensure that grain size is in specific range prior to testing, proppant sample is pre-sieved. If we are testing 20/40 mesh Ottawa sand, then it is expected that 90% of all the proppant is smaller than 20 mesh and greater than 40 mesh;

(II) it should be noted that proppant pack is tested at the same volume concentration but at different mass concentrations due to different grain densities of proppant. API proposed that proppants should be tested at high concentration ≈ [4];

(III) stress is increased at a rate of 2000 psi/min until the target stress is reached after, the sieved proppant is loaded in to proppant crush cell (cell that is 2 inches in diameter and 3.5 inches in height with Rockwell C hardness greater than 42). The target stress on the proppant pack is maintained for 2 minutes;

(IV) proppant is unloaded from the crush cell and sieved. The mass of the proppant which is smaller than the native proppant is reported as “crushed material” (if we are testing 20/40 mesh proppant, then post-test proppant that is smaller than 40 mesh is reported). This mass of crushed material is divided by the total mass to determine the “percent crush”.

To check crush test repeatability, crush tests were performed on 16/30 mesh brown sand at 4000 psi by 11 different laboratories using this methodology (Palisch et al., 2009). **Figure 2** shows the results of these tests performed thrice by each lab (Palisch et al., 2009). Following the procedure discussed above, sieved proppant pack was loaded in crush cell and stress was increased at rate of 2000 psi/min. Consequently, the load was increased to 4000 psi in 2 minutes and held constant at 4000 psi for another 2 minutes. The pre-test particle size distribution of proppant was same for the 11 different laboratories to investigate the variability produced by differences in testing procedures. This study was conducted by API and it shows that percent crushed varies from ≈ 6% to 25% following the API prescribed procedure. The average percent of crushed particles was 14.8%. The crush percentage also varied within lab 4 for 3 different crush test performed. For lab 4, crush percent for the 3 tests varies from 14.7% to 24.5%. The inconsistency between lab measurements might arise due to how the proppant was loaded in crush cell – hand loaded or mechanically.

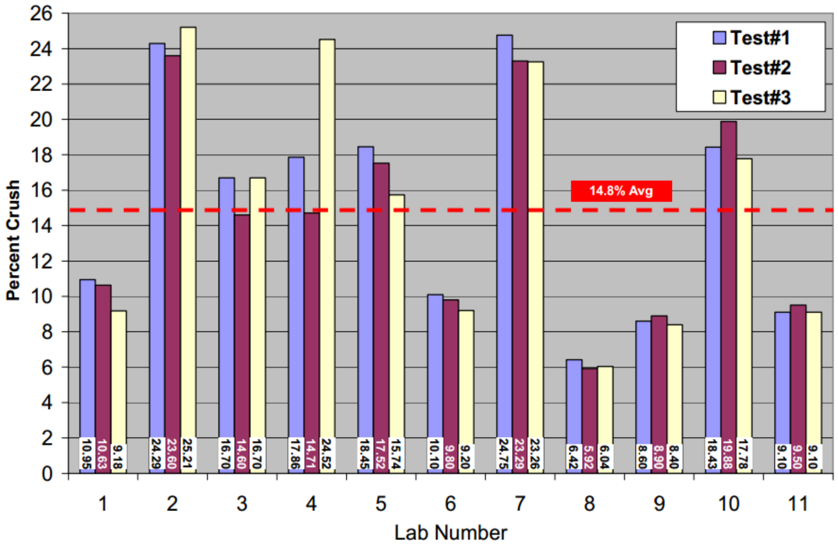

Figure 2: Comparison of percent crush reported by 11 laboratories on hand loaded 16/30 brown sand at 4000 psi (Palisch et al., 2009). Percent crush varied from as low as 6% to as high as 25%.

Howard and Fast (1970) conducted the crush test on sand, light weight ceramics and resin coated sand to study the effect of proppant concentration on “percent crush”. The test was carried out at different proppant concentrations ranging from as low as [0.25] to as high as [8] at 6000 psi pressure. They also indicated that a monolayer of proppant would have proppant concentration of [0.2] which is less than the minimum concentration at which they conducted the crush test. However, it should be noted that the proppant concentration of [1] and lower used in this testing is much closer to realistic field conditions. **Figure 3** shows percent crush as function of proppant concentration for the sand, light weight ceramics and resin coated sand, the percent crush is highest at [0.25] sand and least at [8]. In addition, we see a strong decline in percent crush with increasing proppant concentration for all the three proppants tested. The results from Howard and Fast (1970) were motivation to study the crush test at realistic field conditions of proppant concentration.

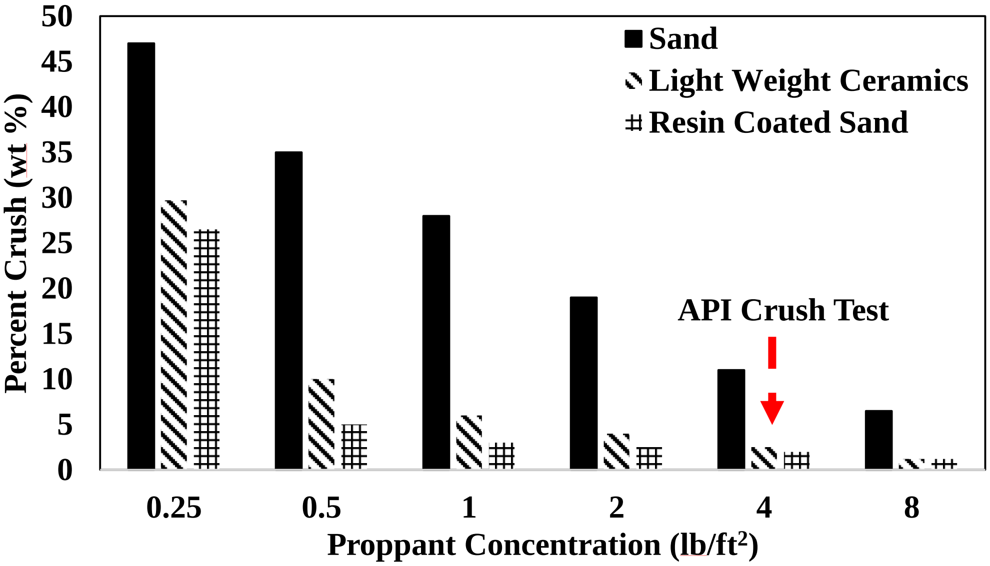

Figure 3: Weight percent crushed particles for various proppants at different concentrations at 6000 psi (adapted from Howard and Fast, 1970). Note the significant difference (factor of 5) in percent crush between API crush test at concentration of 4 lb/ft^2 and monolayer of proppant, 0.25 lb/ft^2 concentration.

Schubarth et al., (2004) conducted test on [2] of 20/40 mesh sand and various ceramic proppants to study correlation between median particle diameter of proppant and conductivity. Tests were conducted at constant load rate of 1000 psi/min and held constant at the target stress for 5 minutes. Tests were conducted in a similar manner as proposed by API, but at a lower concentration than the API standard. The loading rate was kept lower than the API testing method and the hold time was extended.

Schubarth et al., (2004) studied conductivity, defined as product of fracture width and permeability, and proposed that proppant pack conductivity should be function of median particle diameter and broadness of the sieve distribution ($PD\Phi$ in **Equation 1**, see page 9) which was initially suggested by Berg (1970) for permeability of well sorted and high porosity sandstone formations. Schubarth et al., (2004) correlated conductivity at 2000 psi to median particle diameter of ceramic proppants at ambient conditions. Conductivity at 2000 psi was chosen primarily based on the reasoning that ceramic proppant pack would experience "very little crushing", thus allowing correlation to be made to median particle diameter at ambient conditions. A plot of conductivity at 2000 psi versus median particle diameter for different ceramic proppants is shown in **Figure 4**. Note that conductivity at a low axial load of 2000 psi is strongly correlated with median particle size at ambient conditions. However, it was noted by the author that with increasing axial load, conductivity would also be dependent on proppant crushing characteristics. Conductivity as a function of closure stress is presented in **Figure 5** where it is observed that proppant particles with similar median particle diameter at ambient conditions show similar conductivity at 2000 psi. However, we observe a decrease in conductivity with increase in pressure which can be attributed to change in median particle size, which in turn is dependent on crush characteristics of proppant.

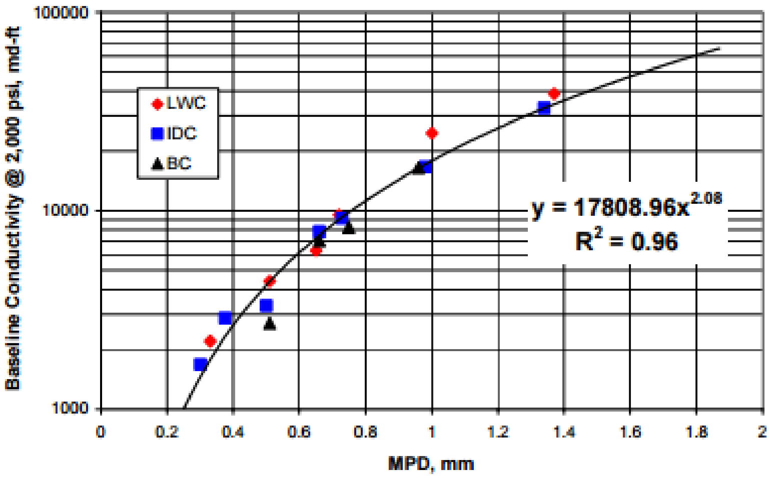

Figure 4: Conductivity at 2000 psi as function of median particle diameter (MPD) of ceramic proppants at concentration of 2 lb/ft^2 concentration – light weight ceramic (LWC), intermediate density ceramic (IDC) and bauxite ceramic (BC) (Schubarth et al., 2004). Higher median particle size corresponds to higher conductivity.

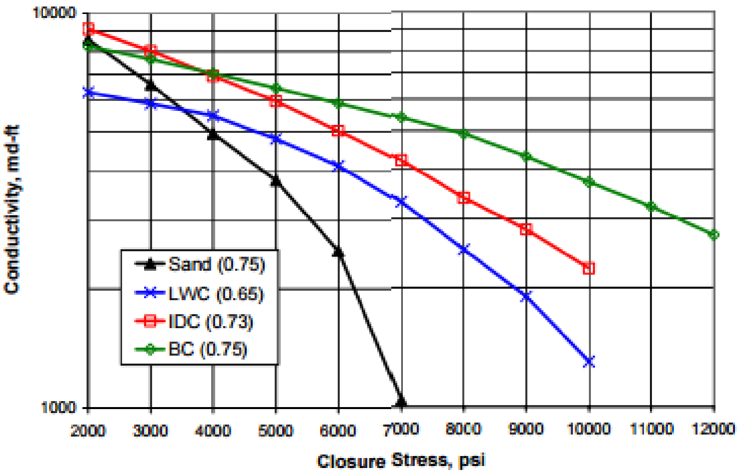

Figure 5: Conductivity as function of closure stress for different proppants at concentration of 2 lb/ft^2 - sand, light weight ceramic (LWC), intermediate density ceramic (IDC) and bauxite ceramic (BC) (Schubarth et al., 2004). Numbers within parenthesis indicate median particle size (mm).

In order to investigate crushing characteristics as function of closure stress, load was increased to a target stress and sieving was performed as a function of target stress in this study. Sieve distribution of 20/40 mesh sand with median particle diameter of 0.52 mm as function of pressure is shown in **Figure 6**. **Figure 6** shows changes in the mass of sieve size at different stresses with respect to that of unstressed proppant. **Figure 6** shows that significant fines, i.e. particles below the 40 mesh, start generating at pressure between 4000 and 5000 psi. Schubarth et al., (2004) did not comment on the relation of reduction in the median particle diameter of proppant to the conductivity, as shown in **Figure 5**.

Schubarth et al., (2004) also studied the effect of stress cycling on proppant crushing using a fully servo controlled hydraulic rock mechanics test machine. To investigate this effect, the procedure above mentioned is repeated for 5 and 20 cycles. **Figure 7** shows the effect of stress cycling on 20/40 mesh sand with median particle diameter of 0.52 mm. The median particle diameter at specific target stress changes with stresses cycling. According to Schubarth et al., (2004), permeability of the fracture calculated using Berg's (1970) correlation (**Equation 1**) would change minimally with changes in median particle diameter.

$k = (5.1 * 10^{-6})\, n^5\ 10^{-6}\ Md^2\ e^{-1.385 PD\Phi}$……………………………………...….(1)

Where:

k: permeability,

n: porosity,

Md: median particle diameter,

$PD\Phi$: difference between *Md* and P_{90} size.

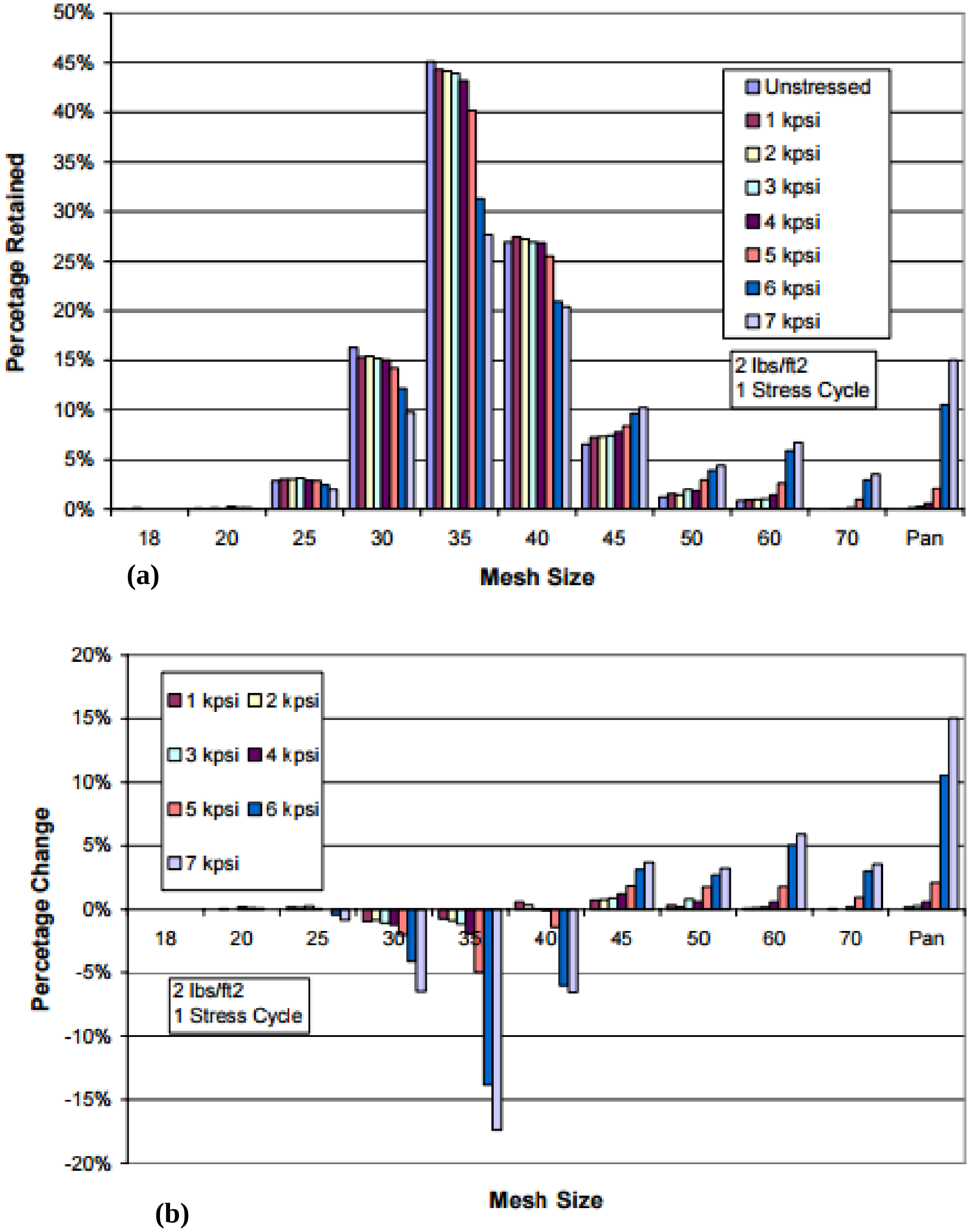

Figure 6: For 20/40 mesh sand (a) particle size distribution as function of stress (b) changes in mass of sieve size at different stresses with respect to that of unstressed proppant. Note the significant change in sieve size distribution at ≈ 5000 psi (Schubarth et al., 2004).

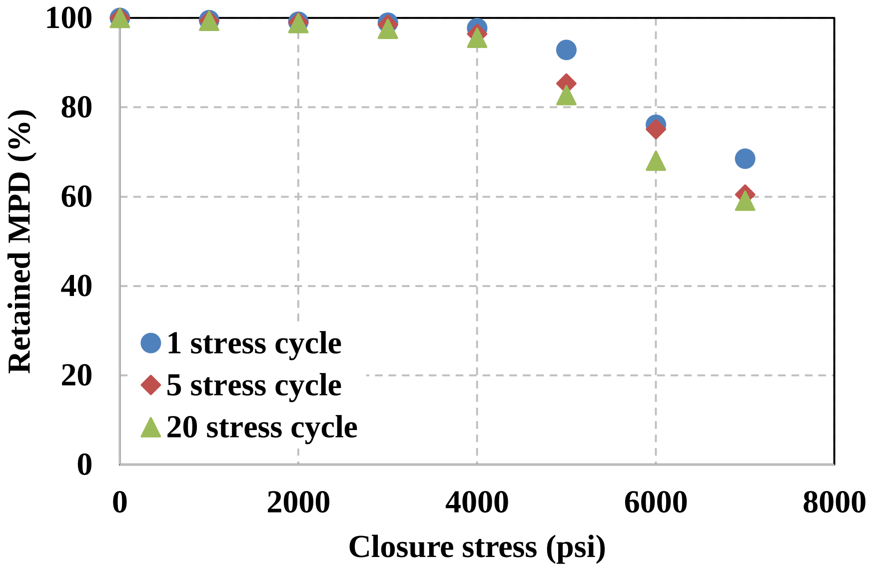

Figure 7: Retained median particle diameter (MPD) as function of closure stress and stress cycles for 20/40 mesh sand with median particle diameter of 0.52 mm (Schubarth et al., 2004). Schubarth et al., (2004) made a note that there is a poor test result at 6000 psi for 5 stress cycles and it needed to be rerun.

Freeman et al., (2009) discusses a modified API crush test at significantly higher temperature on liquid-saturated proppant. Freeman et al.'s (2009) apparatus is shown in **Figure 8**. Tests were conducted on Intermediate Density Ceramic (IDC) and Light Weight Ceramic (LWC), and sieve analysis on the entire mass of post-test proppant was carried out to determine the median particle diameter. Tests were conducted in accordance to API specifications. Another set of tests with similar closure stress and temperature conditions as API tests were conducted with silica saturated fluid flowing during and after the test; the total fluid exposure time was 4 hours. **Table 1** compares the test conducted using similar closure stress and temperature conditions but different methodologies. Fines generation below 40 mesh are quite similar for LWC and IDC at closure stress of 6000 and 7500 psi using the API methodology. However, when the proppant pack was exposed to fluid, fines below 40 mesh increased by more than a factor of 2 for closure stress of 6000 psi and temperature of 200 ^{o}F and became more than 3.5 times for closure stress of 7500 psi and temperature of 250 ^{o}F. At closure stress of 7500 psi and 250 ^{o}F, the median particle diameter reduced which was reflective of additional grain failure as noted by the author. However, the question again is whether these tests are repeatable?

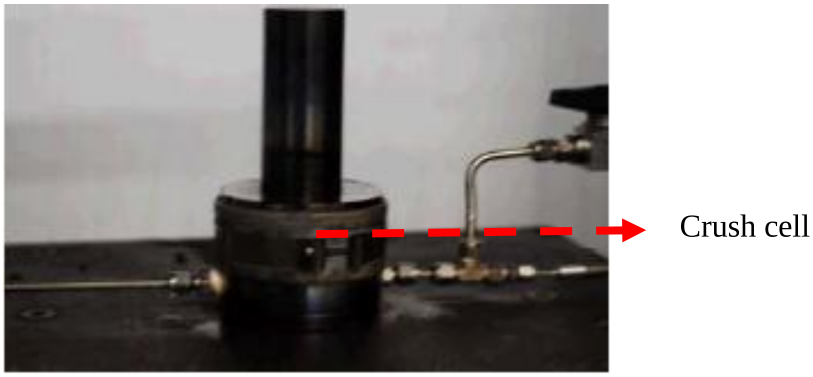

Figure 8: Experimental setup used by Freeman et al., (2009) to conduct testing using liquid saturated proppant at significantly high temperature.

Table 1: API and Modified API crush test conducted at closure stress of (a) 6000 psi and (b) 7500 psi (Freeman et al., 2009). LWC stands for light weight ceramic and IDC stands for intermediate density ceramic.

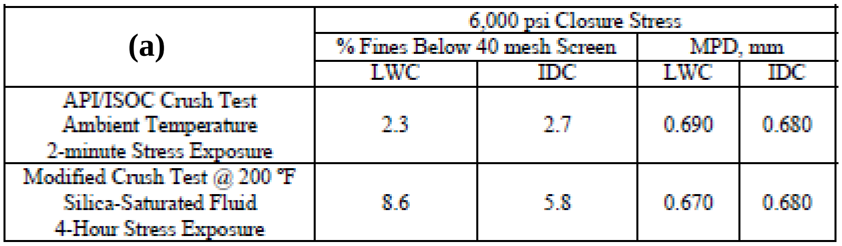

(a)	6,000 psi Closure Stress			
	% Fines Below 40 mesh Screen		MPD, mm	
	LWC	IDC	LWC	IDC
API/ISOC Crush Test Ambient Temperature 2-minute Stress Exposure	2.3	2.7	0.690	0.680
Modified Crush Test @ 200 °F Silica-Saturated Fluid 4-Hour Stress Exposure	8.6	5.8	0.670	0.680

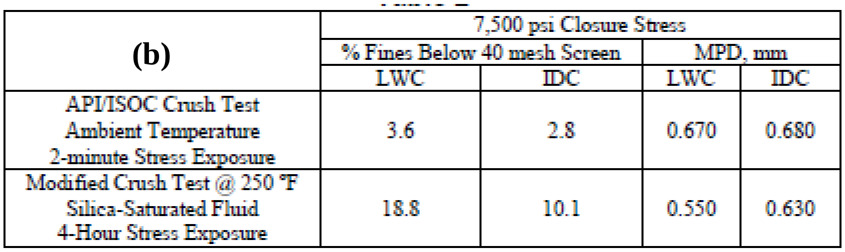

(b)	7,500 psi Closure Stress			
	% Fines Below 40 mesh Screen		MPD, mm	
	LWC	IDC	LWC	IDC
API/ISOC Crush Test Ambient Temperature 2-minute Stress Exposure	3.6	2.8	0.670	0.680
Modified Crush Test @ 250 °F Silica-Saturated Fluid 4-Hour Stress Exposure	18.8	10.1	0.550	0.630

1.4.3 Single particle crush test

Raysoni et al., (2013) proposed the use of single grain crush test and compared results of API crush tests to single particle crush test. They further used single particle crush tests to study effect of diagenesis on crush strength of proppant. This section reviews the single particle crush test primarily used in the ceramic industry - ASTM C1239-07, a standard practice document published by American Society for Testing and Materials (ASTM) for estimating uniaxial strength using a Weibull distribution.

Raysoni et al., (2013) have given a detailed procedure to study the proppant crush strength. First, at least 30 proppant particles are selected based on their uniform size and shape with limitations on particle sphericity. Second, the diameter of each proppant particle is measured by microscopic grain size analysis. Third, the test is conducted to determine the maximum force required to crush individual grains. Finally, the crush strength of proppant particles is determined statistically using Weibull distributions. They show that single grain crush tests show good repeatability. They noted that the stress states that the proppant particle experiences in the API and single particle crush test are significantly different. Single grain crush tests presents us with an understanding of crushing characteristics of monolayer of proppant with isolated proppant grains.

1.4.4 Constant displacement rate crush test

Simo et al., (2013) proposed a new crush test method to study the behavior of proppant pack under stress. Simo et al., (2013) designed this crush test to investigate the characteristics of the proppant packs as a whole by studying the load rate as function of time. The test is carried out on dry proppant packs at ambient temperature conditions. The test cell used is in compliance with API cell dimension and hardness The bottom piston of the cell is displaced at constant rate. The constant piston displacement is controlled by a metering pump and computer which records the applied load. A load is recorded every 5 seconds and converted to stress using area over which load is applied (area of proppant pack).The pressure derivative with respect to time (loading rate) is calculated and plotted as function of time at every 500 psi increase in axial pressure. **Figure 9** shows a typical plot obtained for resin coated sand (RCS) (Simo et al., 2013).

Simo et al. (2013) divided a typical plot shown in **Figure 9** in three regions. In region A, the loading rate increases as function of time and then, becomes stable in region B. In region C, loading rate increases again but at a lower rate than region A. Simo et al. (2013) inferred that the loading rate increase in region A was indicative of grain movement and rearrangement. Similarly, they inferred that stable loading rate in region B was indicative of grain deformation and crushing. Region C (with an increasing loading rate) was identified as the grain rearrangement region once proppant grains were crushed. The end of region B was identified as the failure stress at which the proppant pack was unable to bear any more load and loading rate continued to increase with respect to time.

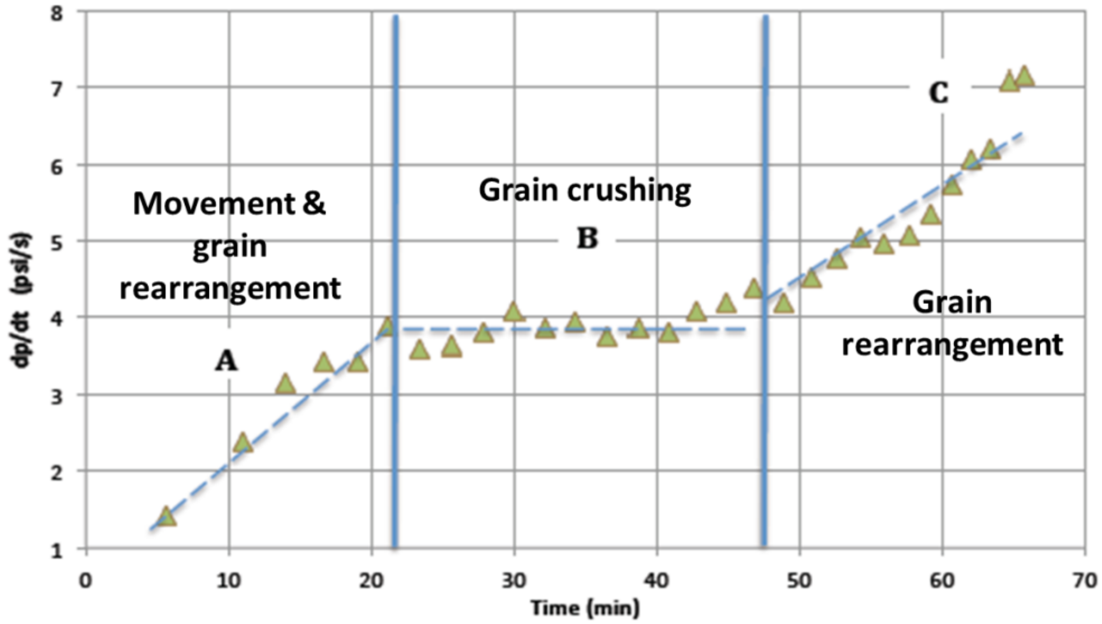

Figure 9: Plot of the applied pressure derivative as function of time for RCS is divided into three regions: A) movement and grain rearrangement, B) grain crushing and C) grain rearrangement (Simo et al., 2013).

Using this methodology, Simo et al., (2013) determined the failure stresses for 30/50 Ohio sand, 30/50 resin coated Ohio sand, 40/70 Ohio sand and 40/70 resin coated Ohio sand at [0.5] to [4]. The failure stress as function of proppant concentration for the 4 different proppants is shown in **Figure 10**. Note that the proppant pack fails at higher stress for higher proppant concentrations. It is also noted by Simo et al., (2013) that resin coated Ohio sand performs better than simple Ohio sand. This increased strength is reflective of changes in mechanical properties of Ohio sand attributed to resin coating.

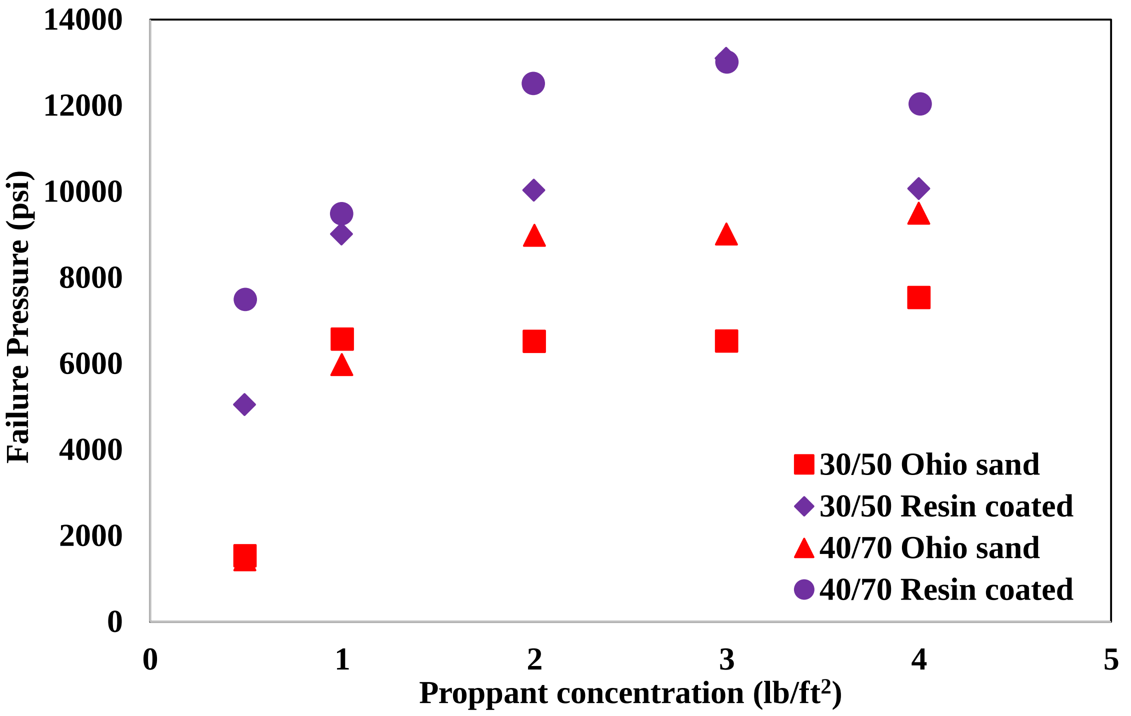

Figure 10: Plot of failure pressure as function of proppant concentration for 4 different proppants (Simo et al., 2013). Increasing proppant concentration is directly correlated with failure pressure.

1.5 Proppant percent crush and permeability

Schubarth et al., (2004) correlated median particle diameter with permeability (see **Figure 4**). Berg, (1970) proposed the use of median particle diameter and broadness of sieve distribution ($PD\Phi$ in **Equation 1**) to predict permeability of well sorted and high porosity sandstones. Permeability is directly dependent on median particle size. Using the correlation proposed by Berg, (1970) (**Equation 1**, see page 9), Schubarth et al., (2004) discussed predicting the changes in conductivity as function of closure stress using the particle size distribution.

Pearson et al., (2014) discussed how to use the proppant crush test and investigated percent crush as function of long term conductivity, i.e. 48 hours from the start of the experiment (Palisch, 2015) . **Figure 11** shows the plot of long term fracture conductivity as function of percent crush for 30/50 and 40/70 intermediate density ceramics and low density ceramics from various manufactures. They concluded from **Figure 11** that percent crush is a poor indicator of long term fracture conductivity.

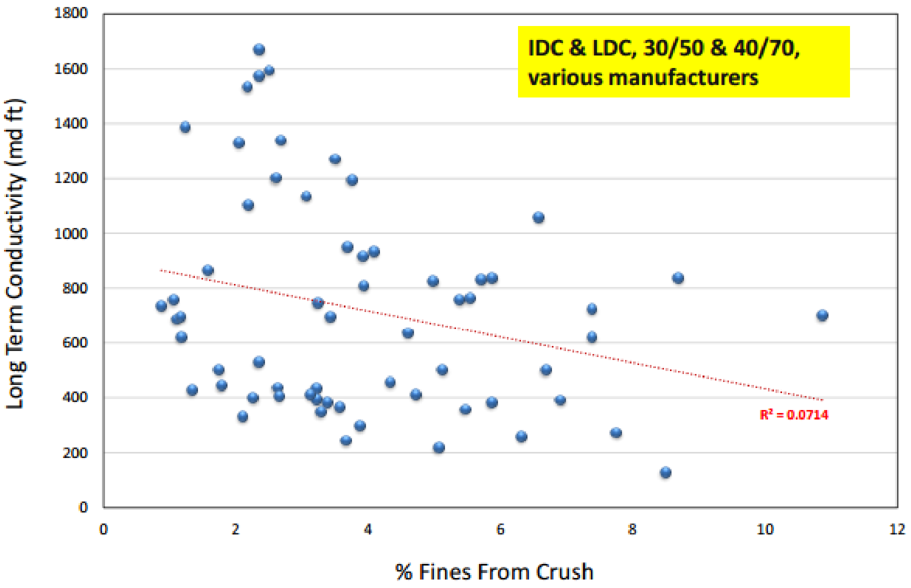

Figure 11: Long term fracture conductivity as function of percent crush for 30/50 and 40/70 intermediate density ceramics and low density ceramics from various manufactures (Palisch et al., 2015).

1.6 Problem statement

Taking into consideration different crush tests performed by various researchers, a goal of the study was to understand how proppant crushing takes place in bulk – [1] versus [4]. Proppant crushing, in bulk, controls flow behavior and compaction of these packs. Compaction at realistic field conditions can be incorporated in reservoir simulation models to estimate the time dependence of fracture conductivity and production more accurately. Understanding of how proppant crushes in bulk would also help to understand boundary effects that might be unknowingly introduced in API crush tests which might not be representative of realistic field conditions.

Chapter 2: Experimental Procedure

2.1 Introduction

A brief overview of the experimental procedure is provided in this chapter. Subsequent sections in this chapter deal with specific equipment used to conduct this test.

Experimental procedure is as follows:

1. Proppant sample is sieved to ensure that the grain size is within the specific range prior to test. If we are testing 20/40 mesh proppant, then 90% of all the proppant should be smaller than 20 mesh and greater than 40 mesh. Sieving is carried out using a vibratory sieve shaker (Restch AS 200). The Restch AS 200 shaker will be discussed in **Section 2.2**.
2. To determine the grain volume a specific proppant occupies at a specific concentration, grain density of the proppant was measured using low pressure helium pycnometer (Micrometrics model II). Using the mass of the specific proppant at a specific concentration, the grain volume can be computed from grain density (grain volume is used in the calculation of porosity). The low pressure pycnometer (LPP) will be discussed in **Section 2.3**.
3. Proppant was weighed to achieve a specific concentration. Crush test was then performed on the weighed proppant using our custom designed crush cell. Crush tests were carried out using mechanical testing machine (MTS – 312, 21). The crush cell was designed to allow microscope imaging during applied axial load. Acoustic emission (AE) activity was also monitored during the test. The mechanical testing machine, crush cell, microscope camera and acoustic emission sensor will be discussed in **Section 2.4**.

4. Post-test proppant (crushed) is analyzed using laser dry particle size analysis (Beckman Coulter LS 13 320) to determine the generation of fines. This is discussed in the last section – **Section 2.5**.

2.2 Vibratory sieve shaker

A Restch AS 200 shaker was used for sieving the proppant pre-test. **Figure 12** shows Restch AS 200 in use. Two sieves as shown in **Figure 12** were used for the purpose of sieving 20/40 mesh proppant to obtain particle size in specific sieve distribution. The sieve stack is brought to motion and particles undergo 3-dimensional movement by spring-mass system operated by an electromagnetic drive (Restch, 2015). Sieving was carried out for an hour on an average and amplitude was set to 60 rpm for all the tests to yield reproducible results.

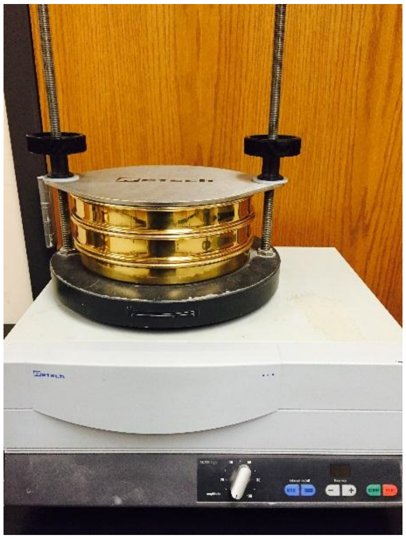

Figure 12: Restch AS 200 vibratory sieve shaker with 2 sieves and a pan. The sieves are 20 and 45 mesh.

2.3 Low pressure pycnometer (LPP)

The LPP intrument from Micrometrics works on the principle of Boyle's Law using helium at a low pressure of 20 psi. Grain volume and thereby grain density is obtained by measuring the pressure drop with and without the proppant samples in the LPP (He crushed porosity) cell (Karastathis, 2007; Shukla, 2013). **Figure 13** shows the LPP machines used.

Figure 13: Micrometrics model II LPP Helium pycnometer for measuring proppant grain density.

2.4 Crush test

Before a crush test is started, a specific mass of proppant needed for a test proppant concentration is weighed. The crush test experimental apparatus has been modified and is different in dimensions specified by API or used by Simo et al., (2013). The crush cell is 1 inch in length and width in comparison to crush cell used by API which is 2 inches in diameter. A loading frame (MTS-312, 21) was used to apply axial force. Upper piston used with a Omega LCHD-20K load cell with a pressure rating of 20,000 lbf and bottom piston is ENERPAC-RLC-502. **Figure 14** shows Omega LCHD-20K and ENERPAC-RLC-502 mounted on the load frame MTS-312, 21.

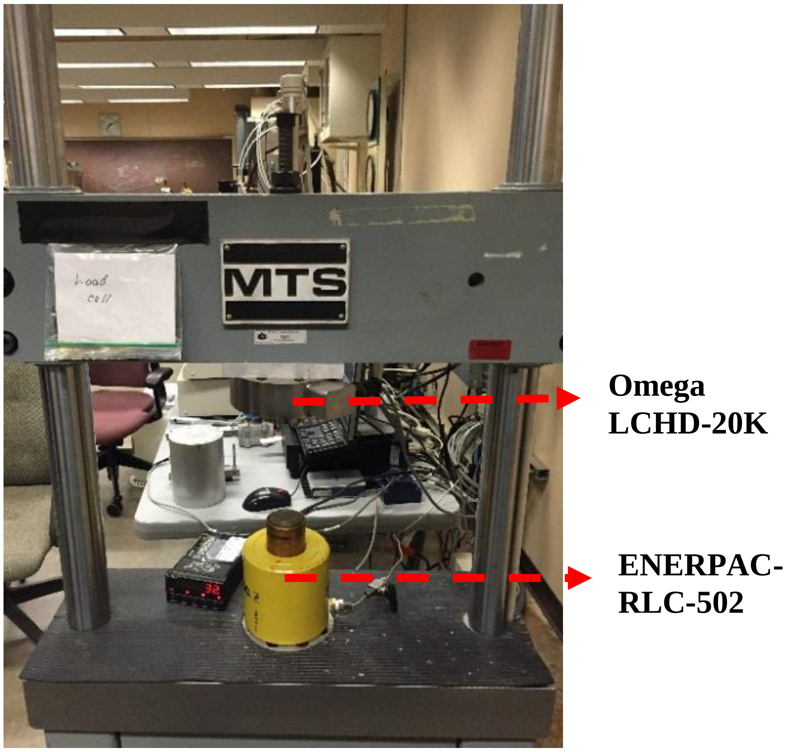

Figure 14: MTS-312, 21 load frame with load cell and axial piston to perform crush tests

In addition, we have a fused silica window on one side of crush cell through which we can capture images. The fused silica window was attached to the crush cell with C-clamps. The crush cell with fused silica window attached is shown in **Figure 15**. The metal for crush cell (aluminum) was chosen to have similar mechanical properties as the fused silica so as to have similar boundary conditions on all the sides. However, it should be noted that upper and bottom piston hardness is in accordance with API - steel having Rockwell C hardness > 42. **Figure 15** shows schematic of crush cell will all different attachments.

The microscope camera used to capture images of proppant is Celstron 5 MP. **Figure 15** shows the Celestron microscope in use and images of the proppant pack. The acoustic activity generated due to crushing as well as rearrangement is monitored using an acoustic emission (AE) sensor mounted on one side of the crush cell. A single 1 MHz piezoelectric transducer was mounted and acoustic activity was captured using the Chechi Handyscope HS4 unit and software Chechi Leach developed by Applied Seismology Consultants. Load data using Omega LCHD-20K and AE was measured every 2 seconds (and were synchronized). Loading rate was calculated from load data averaged over 50 seconds. The hydraulic cylinder is powered by a Teledyne Isco DX100^{TM} pump programmed to apply load to produce a constant displacement rate. Load was increased to a target stress and was not held constant for 2 minutes as suggested otherwise by API. The reasons for doing so would be discussed in next chapter.

To study the effect of pore fluid, the crush cell was modified to conduct testing on proppants subjected to water as pore fluid. A 1/8 inch diameter inlet was drilled on one side of the crush cell and the pressure was maintained with another Teledyne Isco DX100^{TM} syringe pump. **Figure 16** shows the modified crush cell with the pore fluid inlet. **Chapters 3** and **4** have detailed sections on how the crush cell was assembled. The crush cell was assembled differently for tests conducted on dry proppant and proppant pack exposed to fluid.

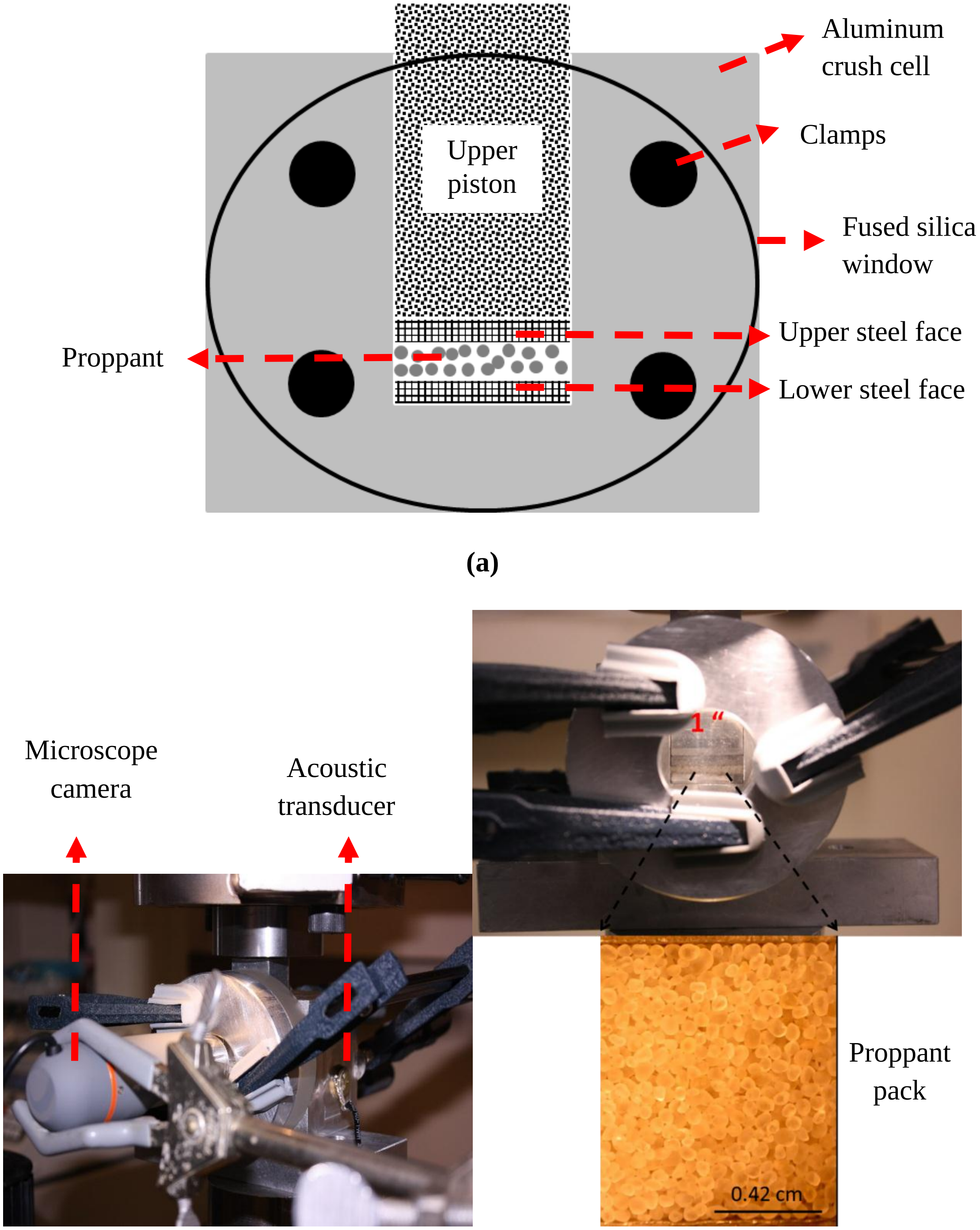

(a)

(b)

Figure 15: (a) Schematic cross-section of crush cell. (b) Left: Crush cell with fused silica window attached and acoustic emission sensor mounted. Microscope camera used is also shown. Right: Fused silica window is shown with a microscope image of [4] of 20/40 mesh Ottawa sand.

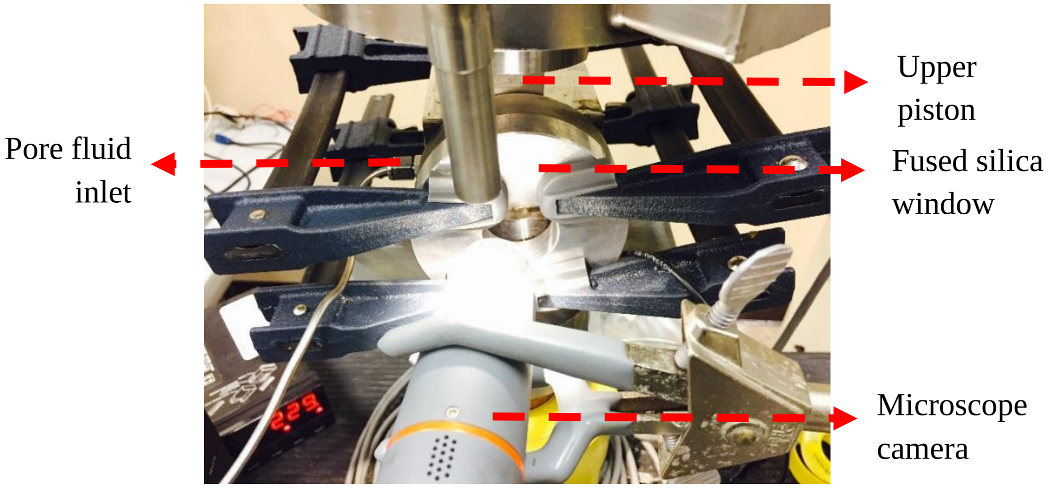

Figure 16: Modified crush cell in use. Pore fluid inlet, microscope camera, upper piston and fused silica window are also been shown.

2.5 Laser particle size analysis

Beckman Coulter LS 13 320 Tornado Dry Power System (DPS) was used to measure particle size distributions. Using the principles of light scattering, LS 13 320 works by analyzing the scattering pattern formed by light intensity as function of scattering angle for particle of different sizes (Beckman Coulter, 2011). Smaller particles scatter at larger angles and vice versa (Beckman Coulter, 2011). Composite scattering pattern is a combination of scattering pattern of constituent particles of different sizes in the sample (Beckman Coulter, 2011). Assuming spherical particle, size is determined by applying the deconvolution to composite scattering pattern based on Fraunhofer or Mie theory of light scattering. LS 13 320 DPS is shown in **Figure 17**.

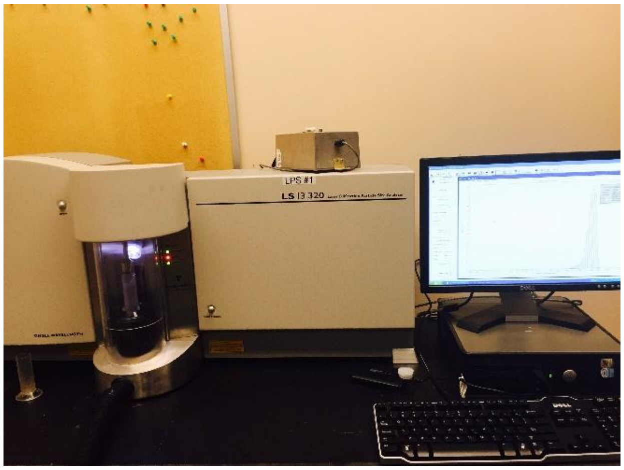

Figure 17: Beckman Coulter LS 13 320 Tornado Dry Power System is used to measure the particle size distribution (particle size range varies from 0.37 to 2000 µm).

Chapter 3: Dry Proppant Crush Test

3.1 Introduction

A dry proppant crush test refers to a test conducted on proppant pack with no liquid in the pack. This chapter covers results from dry proppant crush tests and discussions of critical pressure. Critical pressure (σ_{crit}) is the pressure for onset of grain crushing. It is also defined as the pressure at which fines smaller than the original particle size distribution start to be generated. In the next section (**Section 3.2**), apparatus used to conduct testing on dry proppant is described in detail. In the third section (**Section 3.3**), the effect of hold time (2 minutes as suggested by API) is investigated. In subsequent sections, we discuss the effect of proppant concentration (**Section 3.5**), displacement rate (**Section 3.6**), proppant type (**Section 3.7**), cyclic loading (**Section 3.8**) and fracture morphology (**Section 3.9**) on σ_{crit}. The test matrix used to study the above mentioned effects is described in their respective sections. In the remainder of this thesis, constant displacement rate is represented with the symbol Δ. $\Delta_{3.8}$ refers to displacement rate of 3.8 x 10^{-3} inch/min. Similarly, $\Delta_{11.5}$ indicates 11.5 x 10^{-3} inch/min displacement rate. Remember notation [x] refers to x lb/ft^2.

3.2 Experimental apparatus

A fully assembled apparatus is shown in **Figure 18**. **Figure 19** shows schematically the assembly of the crush cell; the fused silica window is clamped to the outside of the crush cell and then bottom steel platen is inserted. Proppant of specific mass needed to achieve the test concentration is poured into the crush cell from the top. The load on the proppant in increased once top steel platen and piston are inserted.

Difference between how the crush cell was assembled for different tests is discussed in **Chapter 4** as cell assembly can potentially change how the proppant pack reacts within the crush cell.

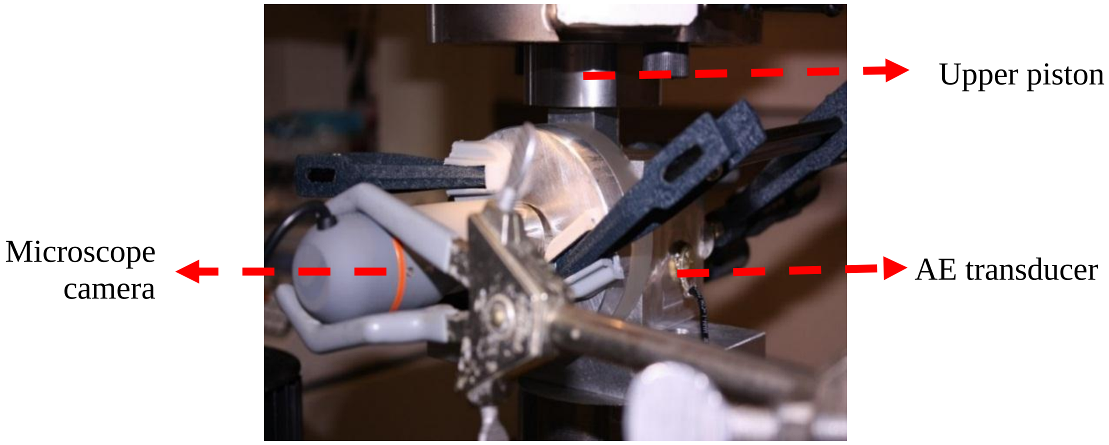

Figure 18: Crush cell used to study dry proppant crushing. AE transducer, microscope camera and upper piston are also shown.

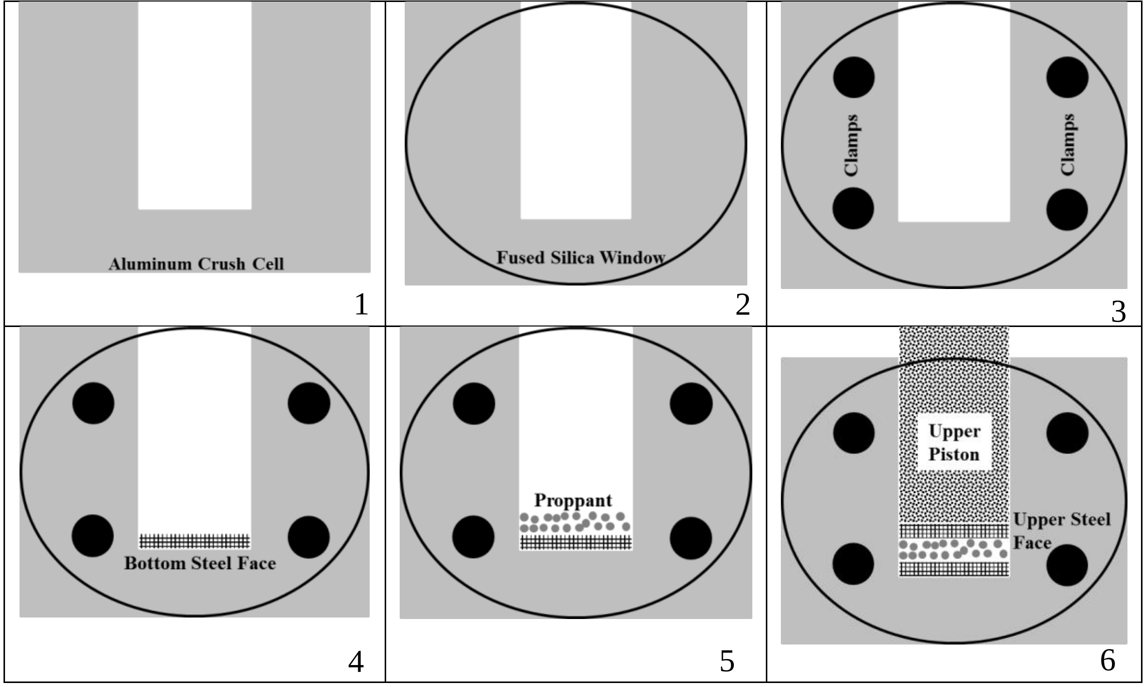

Figure 19: Steps for assembling the crush cell-1: Schematic cross-section of crush cell. 2 and 3: Fused silica window clamped to the outside of crush cell. 4: Bottom steel face is inserted from top of crush cell. 5: Proppant is poured into the cell. 6: Upper steel face and piston is inserted.

3.3 Effect of hold time

The crush test to determine σ_{crit} was performed by keeping the same experimental procedure described in **Chapter 2**:

(1) sieving to achieve a specific proppant size distribution,

(2) pouring the proppant in to the crush cell,

(3) increasing the load to 15000 psi at constant displacement rate and

(4) performing particle size analysis at discrete pressures.

In our tests, in addition to increasing the load to maintain constant displacement rate, instead of constant loading rate (suggested by API), the stress was not held for 2 minutes at the target stress. A study was undertaken to examine the effect of the 2 minute hold time on the AE rate assuming AE rate is representative of particle rearrangement and crushing. The study was performed on [2] of 20/40 mesh Ottawa sand at $\Delta_{11.5}$. **Figure 20** shows the plot of pressure and AE rate as function of time. The pressure was increased to 15000 psi and then held constant for 2 minutes (see **Figure 20**). Additionally, it is observed that AE rate is relatively greater in the region where the load is increased to 15000 psi in comparison to minimal AE rate in the region where the load is held constant for 2 minutes at 15000 psi. From AE rate as function of time, I inferred that most of the grain crushing and rearrangement takes place during the loading process. Thus, all the tests in this and the next chapter are conducted by increasing the load to 15000 psi and then unloading it without holding proppant pack at specific target stress for 2 minutes. More tests are needed at different displacement rates, proppant concentration and proppant types to conclude that hold time of 2 minutes is not required.

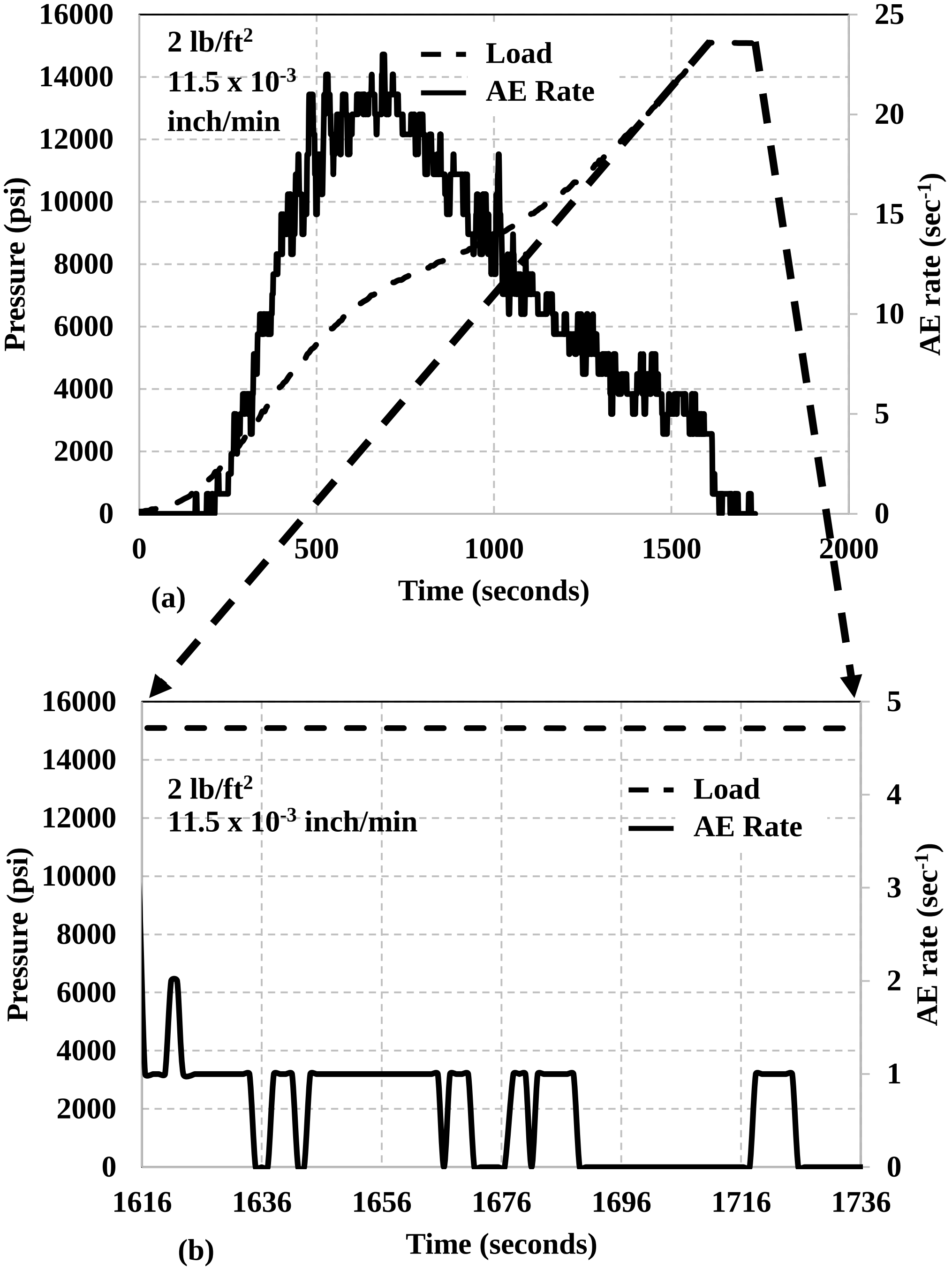

Figure 20: (a) Plot of pressure (dash) and AE rate (solid) as function of time. Pressure is increased to 15000 psi and held constant for 2 minutes. (b) Magnified plot of the 2 minutes hold time region. AE rate is minimal indicating minimal crushing and rearangement.

3.4 Overview of crush test analysis

3.4.1 Results

A crush test carried out on 20/40 mesh Ottawa sand at [4] and $\Delta_{3.8}$ is discussed. The methodology used in this single test is the basis for other crush tests. Stress on the proppant pack is increased to 15000 psi as depicted in **Figure 22**. Particle size analysis (see **Figure 21**) was also carried out at progressively higher pressures over the range from 2500 psi to 14000 psi. For particle size analysis, unstressed proppant was used for each run and stress was increased at constant displacement rate to specific target stresses and particle size analysis was performed. Note that the pre-test particle size distributions for each run were quite similar. **Figure 21** shows that at [4] of 20/40 mesh Ottawa sand fines begin to generate at 5500 psi. We observe a bimodal distribution of proppant when stress is increased to 14000 psi. We refer to the two dominant particle size as smaller and larger dominant particle size. It is also observed that there is a shift in larger dominant particle size peak when comparing post-test proppant pack at 14000 psi to a pre-test proppant pack (native proppant). σ_{crit} for 20/40 mesh Ottawa sand at [4] is determined to be 5500 psi.

Changes in AE rate (see **Figure 22**) start at about 1000 seconds into the test. The AE rate reached a peak around at 1700 seconds and then gradually decreased. The σ_{crit} of 5500 psi of 20/40 mesh Ottawa sand at [4] is indicated on the plot of stress and AE rate as function of time with the red line. **Figure 22** shows stress and AE rate are qualitative indicators of σ_{crit}.

The loading rate varies as function of time when the load on proppant pack is increased at constant displacement rate (see **Figure 23**). The loading rate peaks, then decreases to a minimum and finally increases at a lower rate than the initial increase (this is considered as characteristic response for loading rate). The loading rate increases over the region where particles rearrange but do not crush, as determined by particle size analysis (see **Figures 21** and **23**). **Figures 21** and **23** shows the loading rate starts to decrease and proppant pack reaches σ_{crit} which leads to the generation of fines.

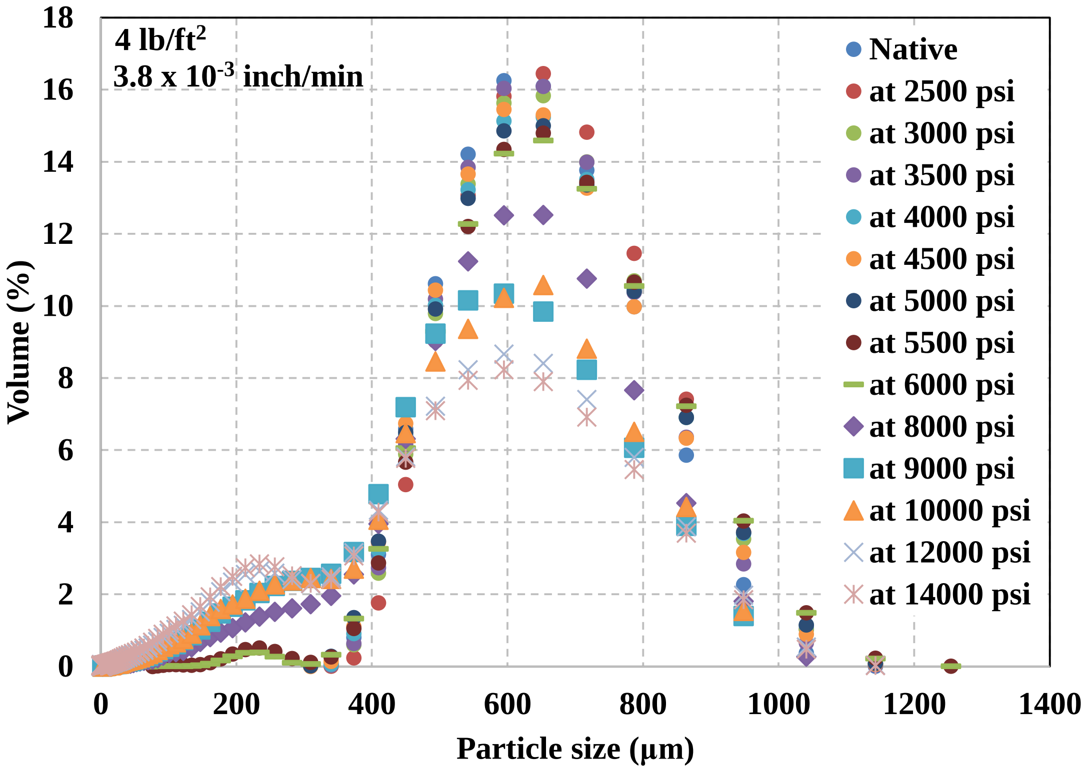

Figure 21: Particle size analysis as function of pressure. σ_{crit} of concentration of 4 lb/ft^2 of 20/40 mesh Ottawa sand is 5500 psi.

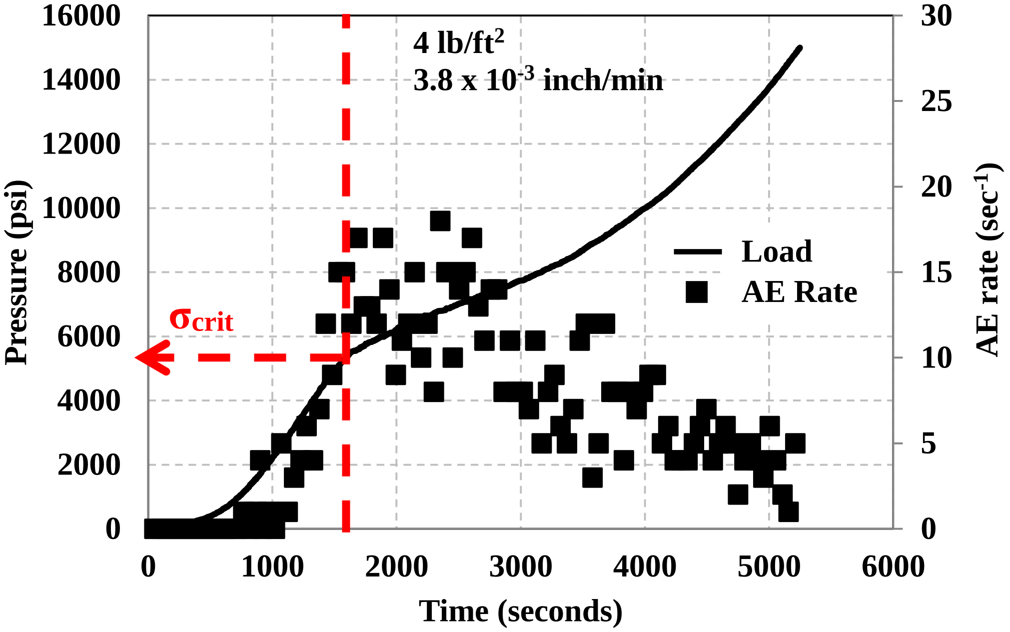

Figure 22: Plot of pressure (line) and AE rate (square) as function of time. Red line indicates σ_{crit} for concentration of 4 lb/ft^2 of 20/40 mesh Ottawa sand.

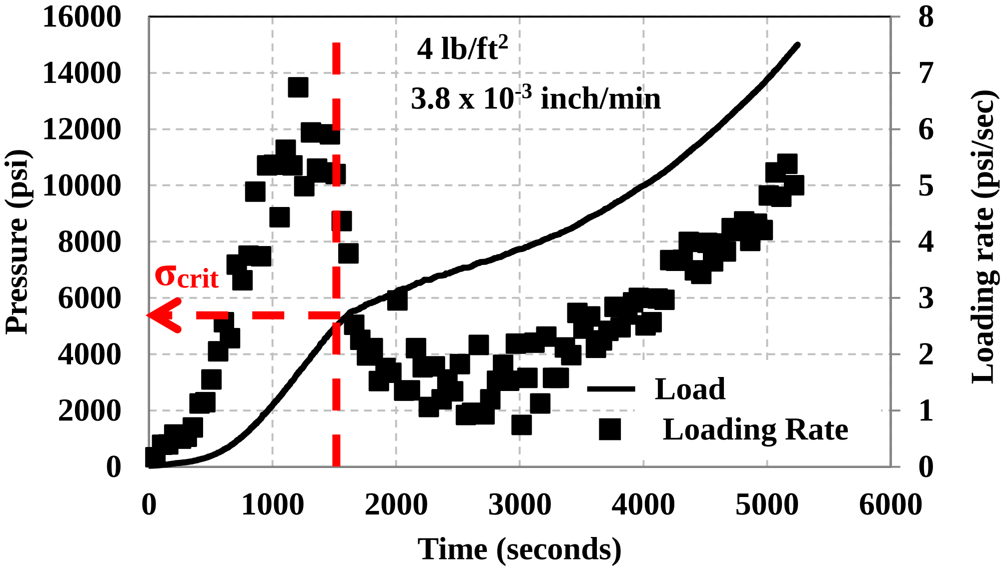

Figure 23: Plot of pressure (line) and loading rate (square) as function of time. Red line indicates σ_{crit} for concentration of 4 lb/ft^2 of 20/40 mesh Ottawa sand.

Using the microscope images (see **Figure 24**) of 20/40 mesh Ottawa sand at [4], we studied changes in proppant pack as function of stress. **Figure 24** shows 20/40 mesh

Ottawa sand starts to generate fines at 6000 psi which is in accordance with particle size analysis results. Images show that proppant pack starts to compress when the pack has reached σ_{crit} (5500 psi) and while loading rate starts to decrease (see **Figure 23**). Visual observation confirms that proppant pack continues to compact after σ_{crit} is reached. Thus, the decrease in loading rate (as function of time) is a qualitative indicator of compaction. In addition, we observe that the proppant crushes non-uniformly and preferentially at the steel-proppant interface.

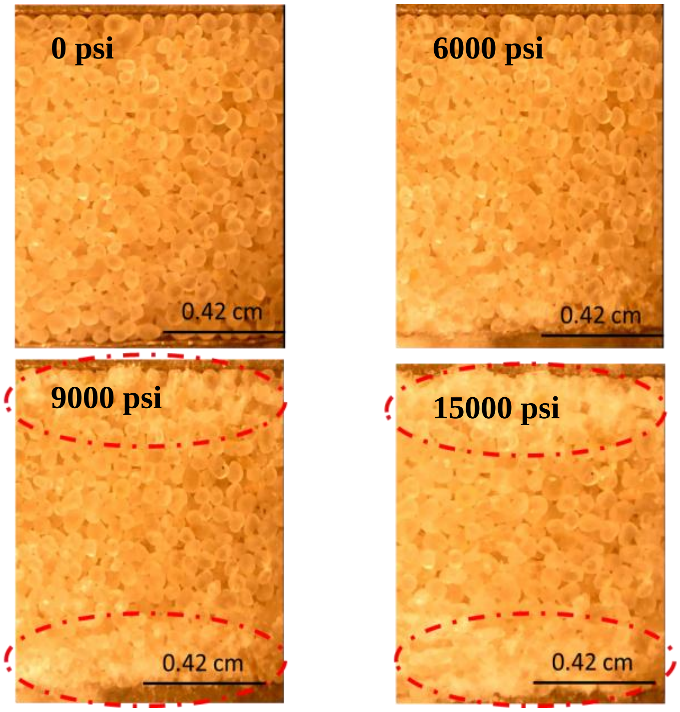

4 lb/ft^2 3.8 x 10^{-3} inch/min

Figure 24: Microscopic images as function pressure. Crushing starts at 6000 psi which is in accordance with particle size analysis results. Additionally, crushing is non-uniform and primarily concentrated at steel-proppant interface.

Microscope images were used to study the width of proppant pack as function of stress. Width is plotted as function of pressure in **Figure 25**. This width (height) was used to compute the bulk volume of the proppant pack knowing the cross-sectional area of the proppant pack (crush cell length and width). The grain density was experimentally determined, using a low pressure helium pycnometer, to be 2.65 gm/cc for 20/40 mesh Ottawa sand. The grain density was used to compute grain volume knowing the mass of the proppant. Porosity as function of pressure was computed using the calculated bulk volume and grain volume. **Figure 25** shows reduction in porosity from 39% at 100 psi to 26% at 14000 psi.

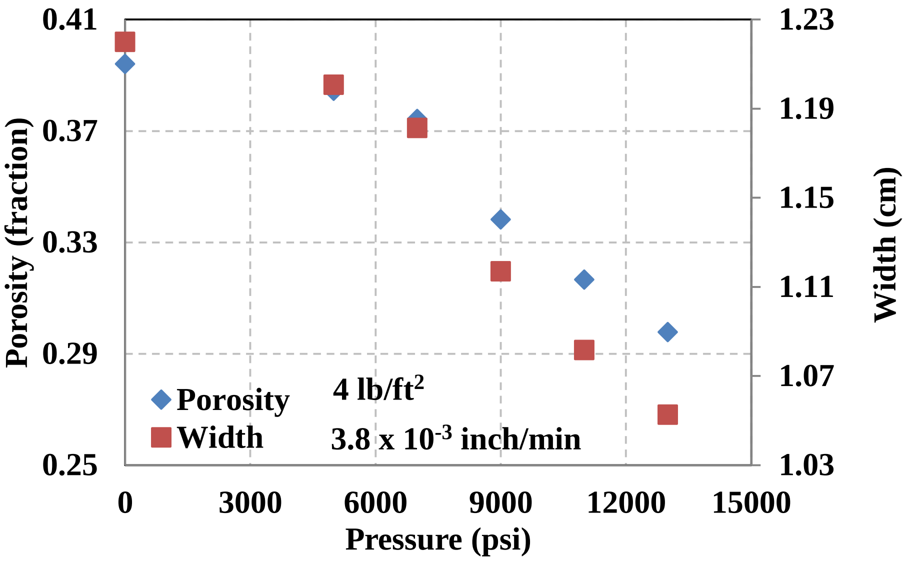

Figure 25: Proppant width (square) calculated from the images and computed proppant pack porosity (diamond) from the measured width are plotted as function of pressure.

Width was used to compute the reduction in fracture conductivity, F_c (see **Equation 2**), as function of pressure (see **Figure 25**). F_c is defined as:

$F_c = k_f * W$ ……………………………………………………………………...(2)

Where:

k_f: fracture permeability,

W: fracture width.

Permeability of fracture was assumed to be constant and width of the fracture was used to compute reduction in conductivity. Conductivity reduction, ΔF_c, is plotted as function of pressure in **Figure 26**; note that conductivity is reduced by 2 percent at 6000 psi solely due to grain rearrangement. We calculated a sudden decrease in conductivity with increase in pressure beyond 6000 psi. F_c decreases by more than 10 percent at 10000 psi due to crushing and rearrangement of proppant. It appears that [4] of 20/40 mesh Ottawa sand can perform optimally to a closure stress of 6000 psi, beyond 6000 psi, crushing and fines generation become a concern.

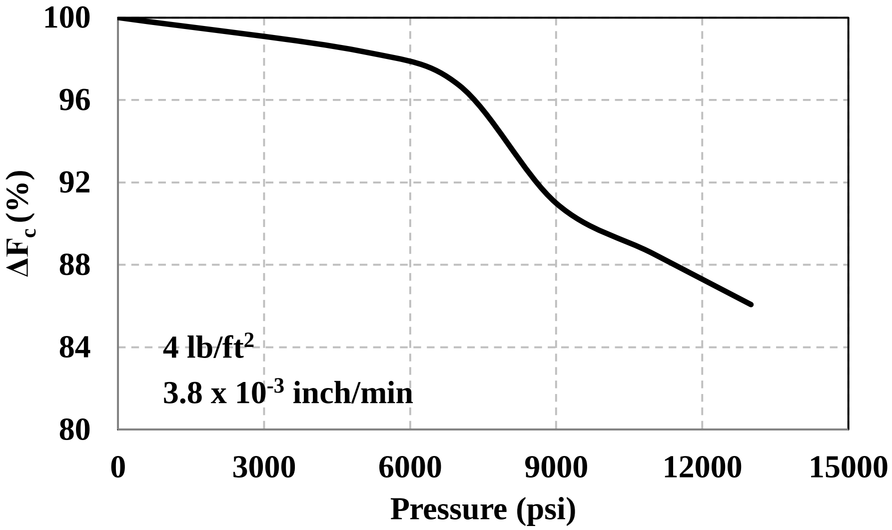

Figure 26: Conductivity reduction as function of pressure. Conductivity reduced rapidly after 6000 psi as 20/40 mesh Ottawa sand reaches its σ_{crit}.

3.4.2 Discussion

Hydrostatic and uniaxial compression testing has been carried out on both uncemented and cemented granular aggregates. Highly porous sandstones are included in the class of cemented granular aggregates. Extensive research has been carried out on highly porous sandstones using hydrostatic compression tests. Hydrostatic compression tests were carried out by measuring the change in volume of sample while stepwise increasing the confining pressure but maintaining a constant pore pressure (Zhang et al., 1990).

Previous researchers (Zoback and Byerlee, 1976) have also studied the behavior of granular materials under stress with the aim of quantifying fluid flow properties. Brace et al. (1978) reviewed the literature and indicated that compaction behavior under hydrostatic stress conditions can be classified into three major categories (see **Figure 27**). First compaction behavior (I) is indicative of microcrack dominated low porosity rock. Second compaction behavior (II) is indicative of intermediate porosity rocks. Third compaction behavior (III) has similar loading response shown in **Figure 22** for 20/40 mesh Ottawa sand at [4]. Brace et al., (1978) characterized the third compaction curve as that for highly porous sandstones. The plot of hydrostatic pressure versus volumetric strain (see **Figure 27**) is non-linear initially which is followed by linear trend till the inflection point, P_i. The volume decrease with pressure is indicative of irrecoverable compaction once the inflection point, P_i, is reached. This irrecoverable compaction was attributed to grain crushing occurring beyond the inflection point for these highly porous sandstones (Zhang et al., 1990). The inference of grain crushing was supported by microscopic observations of sandstones after exposure to pressures higher than the inflection point (Zhang et al., 1990).

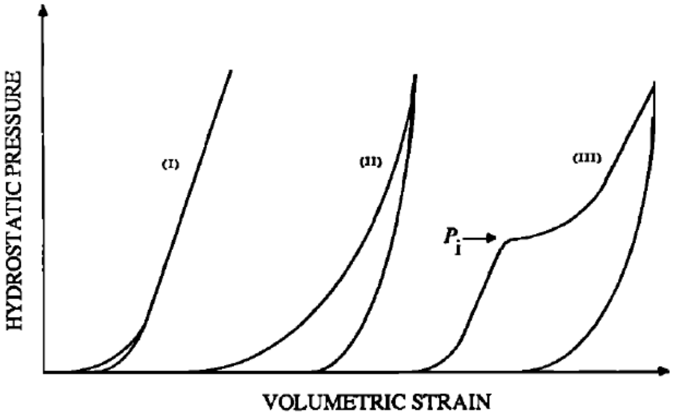

Figure 27: Three major types of hydrostatic compression behavior (Brace et al., 1978; Zhang et al., 1990).

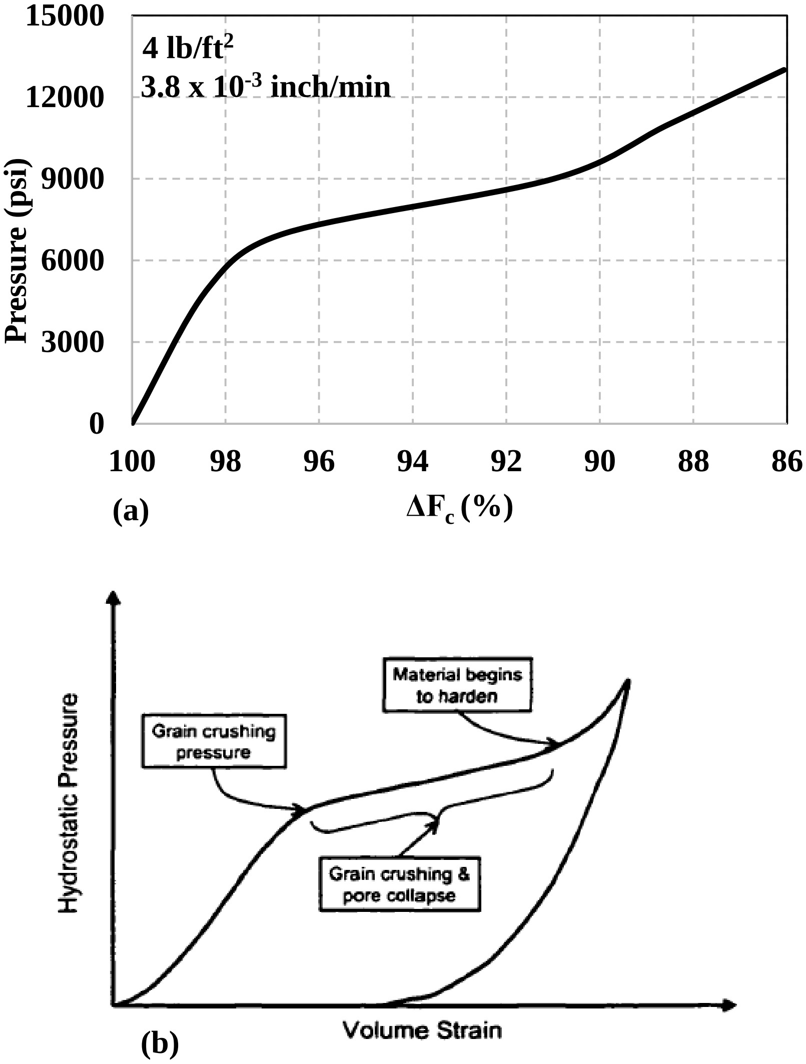

Figure 28: (a) Plot of pressure as function of ΔF_c. ΔF_c represents change in width and is comparable to volume strain. (b) Characteristic hydrostatic compression for highly porous sandstones. Region indicating grain crushing and collapse is similar to that observed in (a) (Issen, 2000).

Further hydrostatic compression testing was carried out by Zhang et al., (1990) on sandstones with porosity as high as 35%. For sandstones with porosity greater than 20%, Zhang et al., (1990) observed the third compaction behavior shown in **Figure 27**. **Figure 28 (a)** shows the plot of pressure as function of ΔF_c. ΔF_c represents change in width and is comparable to volume strain. **Figure 28 (b)** depicts the characteristic hydrostatic pressure and volumetric strain curve with different regions labelled (Issen, 2000). Comparing **(b)** and **(a)**, we observe that there is a similar linear trend before reaching the inflection point. Particle size analysis indicated that 20/40 mesh Ottawa sand at [4] starts to crush at 5500 psi, i.e., the inflection point (see **Figure 28 (a)**). Zhang et al., (1990) suggested that grain crushing provided additional degrees of freedom for grains to rotate and thus compact more densely by moving into intergranular pore space. However, it should be noted that the test conducted by Zhang et al., (1990) was carried out by maintaining constant pore fluid pressure of 10 MPa (1450 psi). The presence of pore fluid tends to reduce frictional resistance at grain-grain contacts and promote movement.

Zhang et al., (1990) also modeled grain crushing using the Hertzian theory and they note that Hertzian theory is only applicable for the elastic range, i.e., before the inflection point. Hertzian theory fails to account for grain rotation and crushing, and thus, cannot explain behavior after the infection point. Using the Hertzian theory, it was determined with assumption of a number of grain contact = 8.84 by Zhang et al., (1990) that σ_{crit} at which fracture initiates at grain-grain contact is inversely dependent on product of porosity and grain radius.

Note that the above mentioned hydrostatic compression tests were conducted on sandstones which is different from uniaxial strain compression testing of uncemented granular aggregates. The test conducted on 20/40 mesh Ottawa sand is carried out under uniaxial compression and lateral confinement. Wong et al. (2004) showed the difference in the state of stress in two dimensional (2-D) array of particles when load is isotropic and anisotropic. Isotropic load is representative of hydrostatic loading while anisotropic loading is representative of uniaxial strain compressive testing. **Figure 29** shows that when uncemented granular aggregates are loaded under anisotropic stress conditions, grains not only experience compressive stresses as in the cases of hydrostatic loading, but grains also experience tensile forces (negative values in **Figure 29**). Grains failure could take place in two modes: compression and tension.

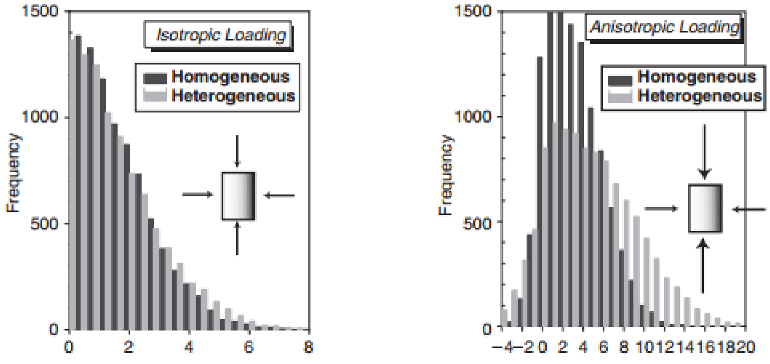

(a) **(b)**

Figure 29: Grain-grain contact forces for: (a) isotropic loading and (b) anisotropic loading. Homogenous case has constant stiffness particles while heterogeneous case has particles of 4 different stiffnesses (Wong et al., 2004).

Tang and Hudson, (2010) simulated breakage of single irregular particle under diametral loading without and with confinement. Researchers carried out simulation to study shear stress fringe contours, normalized stress distribution, and load and released energy during failure as function of applied displacement. For the tests conducted without and with confinement, they noted that a large load drop and energy release coincides with the fracture initiation. We observed similar results for loading rate and AE rate in **Figure 25**. They indicated that single particle under confinement fails in more ductile manner compared to particle without confinement, causing particle under confinement to fail at a greater load.

Gallagher et al., (1974) conducted testing on uncemented granular spherical particle (CR-39) aggregates to study how the stress is transmitted across the grain contacts under hydrostatic and uniaxial load using photoelasticity. Grains in contact had similar mechanical properties which is similar to test conducted on 20/40 mesh Ottawa sand. Gallagher et al., (1974) also showed how the particle arrangement would be affected by hydrostatic or uniaxial stress which would lead to different stress distribution among particles. **Figure 30** shows a hexagonal array of same sized particles with isotropic and anisotropic loading. In the case of isotropic loading, load is distributed among 5 grains in 2-D by an interior grain. While load is distributed among only 3 grains in 2-D by interior grain in the case of anisotropic loading. Fracture patterns for cubic packing and hexagonal packing using the extension-fracture criterion was predicted by Gallagher et al., (1974). **Figure 31(left)** shows the fracture patterns for cubing packing as function of applied load. **Figure 31(right)** illustrates the fracture pattern developed in hexagonal packing.

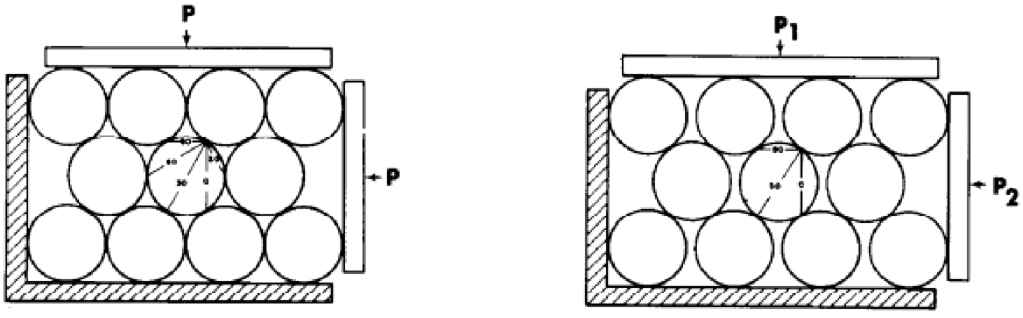

(a) **(b)**

Figure 30: Grains are packed hexagonally. a) Hydrostatic load, P. b) $P_1 >> P_2$. 20/40 Ottawa sand is investigated under condition (b) where $P_1 >> P_2$ (Gallagher et al., 1974).

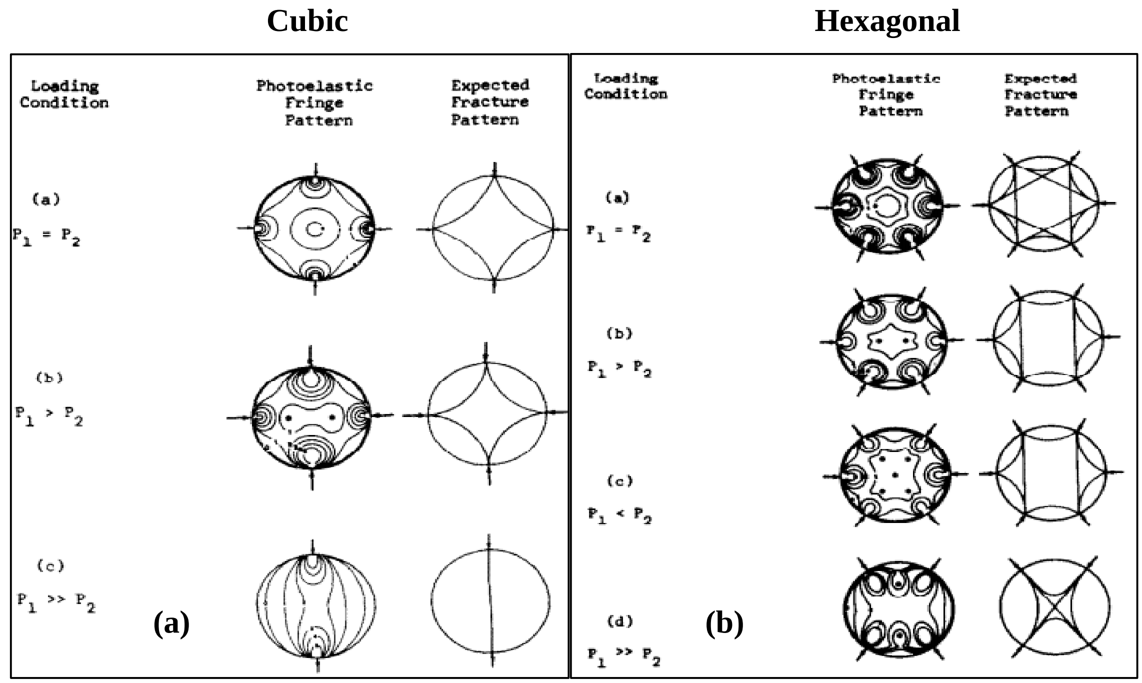

Figure 31: Fringe patterns for an interior grain as function of applied load. P_1 is applied vertically with P_2 applied horizontally. Expected fracture pattern is predicted: a) cubic b) hexagonal packing (Gallagher et al., 1974).

The fringe pattern in **Figure 31** shows that stress is concentrated primarily at grain-grain contacts and thus, fractures initiate there. Additionally, grains are expected to fracture differently when the applied vertical load is significantly higher than the horizontal load. When the grains are packed hexagonally, the fringe pattern shown in **Figure 31** correlates well with contact lines shown in **Figure 30**. The state of stress will control how and where a fracture initiates at the grain-grain contacts.

Note that test conducted on 20/40 mesh Ottawa sand is different from tests reported in literature on sandstone due to cemented grain. Cementation of granular material is another parameter that has been studied extensively. David et al., (1998) made synthetic sandstones by mixing silica sand grains and silica gel using hot-pressing technique proposed by den Brok et al., 1997 (see Wong et al., 2004). Hydrostatic tests were conducted on synthetic rocks with different volumetric cement concentration: 3 and 5%. It was observed from hydrostatic tests that σ_{crit} increases with increase in the volume of cement. Uncemented granular aggregates would have relatively lower value of σ_{crit} as compared to cemented granular aggregate.

In addition to investigating compression tests, previous researchers have also observed increased AE with grain crushing (Zhang et al., 1990; Talwani et al., 1973). Talwani et al., (1973) conducted hydrostatic compression testing on uncemented quartz sand where they observed sudden AE with increased bulk compressibility at 600 bars (8702.2 psi) which was attributed to the onset of grain crushing. Zhang et al. (1989) investigated grain crushing and AE in highly porous sandstone (Boise sandstone, $\Phi = 35\%$). Porosity change and the AE rate for a hydrostatic test on Boise sandstone is shown as function of effective pressure (see **Figure 32**). The AE rate increases when there is sudden decrease in porosity. Grain crushing was confirmed by post-test microscope observations and was related to the decrease in porosity (Zhang et al., 1990). This sudden change in porosity has also been observed by Zoback and Byerlee, (1976) while conducting hydrostatic compression experiments on uncemented quartz sand; results are shown in **Figure 33**. We observed similar results in **Figure 25**.

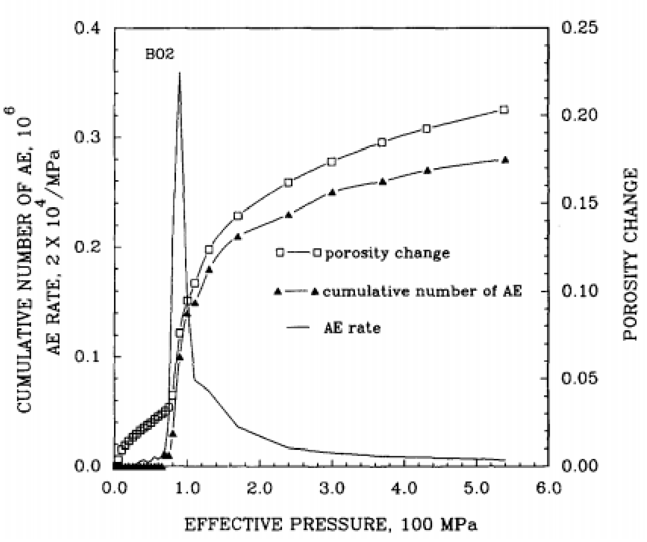

Figure 32: Acoustic emission (AE) rate and porosity change as function of effective pressure (Zhang et al., 1989). Porosity change and AE rate are well correlated. (1 MPa = 145.04 psi)

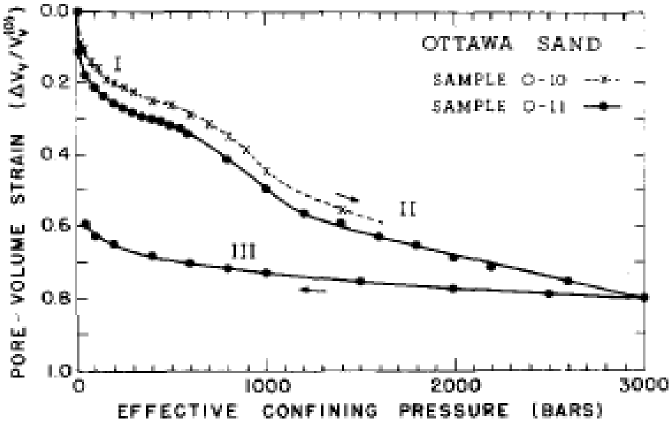

Figure 33: Pore-volume strain as function of confining pressure. Note the hysteresis in pore-volume strain and the sudden increase in pore volume strain at the onset of grain crushing at 600 bars (8702.2 psi) (Zoback and Byerlee, 1976). (1 bar = 14.504 psi)

Literature on compaction bands was reviewed due to observations presented in **Figure 24**. Issen and Rudnicki, (2001) investigated the conditions for formation of compaction bands. Compaction bands are localized planar zones that form perpendicular to compressive principal stress caused by purely compressive deformation (Issen and Rudnicki, 2001). Their occurrence was observed by previous researchers in highly porous sandstones. These dense zones act as barrier to flow within reservoirs. Permeability and porosity of these bands were compared to the host rock by Aydin and Ahmadov, (2009). Their study was carried out on aeolin sandstones. A plot of permeability versus porosity shows that permeability of host rock is at least 3 order greater than the permeability of bed parallel bands (see **Figure 34**). Tang and Hudson, (2010), when studying single particle breakage through simulation models, indicated that zones of localized deformation in the vicinity of upper and lower loading platens were formed partly due to constraint effects. It is a possible that these zones formed in 20/40 mesh Ottawa sand in **Figure 24** arose due to boundary conditions - mismatch in mechanical properties of quartz sand and stainless steel. However, note that the stainless steel face was used in accordance with API procedure that recommends the use of material having hardness > 42 Rockwell C. Thus, experimentation should be conducted using material having mechanical properties more appropriate to realistic field conditions. But if compaction bands do exist, these would act as barriers to fluid flow from the reservoir to the fracture.

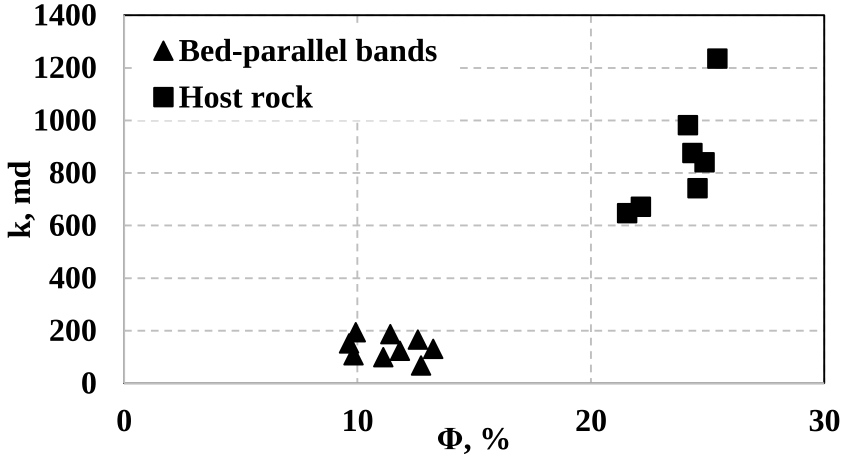

Figure 34: Plot of permeability and porosity for host rock and bed parallel bands. Host rock permeability is 3 order more than permeability of bands (Aydin and Ahmadov, 2009).

The question becomes: under what stress conditions should proppant be tested? For this study where proppants are loaded uniaxially under lateral confinement, we would still observe a σ_{crit} when the grains start to fracture. σ_{crit} will be dependent on both the individual grains and the pack. The reason for influence of proppant pack on σ_{crit} is that a higher proppant concentration will distribute the stress among a greater number of grains in comparison to lower proppant concentration and change the pack response. We next investigate the σ_{crit} by varying the proppant concentration.

3.5 Effect of proppant concentration

3.5.1 Results

20/40 mesh Ottawa sand was tested at three different concentrations – [1], [2] and [4] while keeping the displacement rate constant to study the effect of proppant concentration on σ_{crit}. The test matrix is shown in **Table 2**.

Table 2: Test matrix for the crush test showing the proppant type and displacement rate used for 3 different concentrations of 20/40 mesh Ottawa sand: 1, 2 and 4 lb/ft^2.

Proppant type →	**20/40 mesh Ottawa sand**		
Displacement rate ↓	**[1]**	**[2]**	**[4]**
$\mathbf{\Delta_{3.8}}$	✓	✓	✓

The loading rate and AE rate as function of time for different proppant concentrations - [1], [2] and [4] were also studied and plots are shown for each in **Figures 35(a), 36(a)** and **37(a)**, respectively. Particle size analyses as function of axial pressure for [1], [2] and [4] are shown in **Figures 35(b), 36(b)** and **37(b)**, respectively. The characteristic response for loading rate and AE rate as function of time is similar for the three different concentrations. The loading rate increases initially to reach peak loading rate after which it decreases. After reaching the minimum, loading rate again increases but at a lower rate than initial increase. AE rate increases when loading rate is increasing as function of time and reaches peak when the loading rate is decreasing as function of time.

Particle size analysis was carried out for tests at progressively higher pressures over the pressure range of 2000 psi to 15000 psi. Native proppant for each run was selected such that particle size distribution was nearly similar. We followed consistent procedure throughout the test:

(1) native proppant was used for each run,

(2) stress was increased at constant displacement rate to the specific target stress and

(3) particle size distribution was analyzed after achieving the target stress.

The σ_{crit} for different concentrations (i.e. 2500 psi for [1], 4000 psi for [2] and 5500 psi for [4]) was determined from particle size distributions (see **Figures 35(b), 36(b)** and **37(b)**). Red lines in **Figures 35(a), 36(a)** and **37(a)** indicates the σ_{crit} for respective concentrations. The σ_{crit} occurs in the region where loading rate starts to decrease and AE rate increases. Zhang et al., (1990) indicated that grain crushing provides additional degrees of freedom for rotation and movement, the pack is able to compact more subsequently pressure increases gradually at a constant displacement rate which results in loading rate decrease as function of time. Compaction of proppant pack has been confirmed visually (see **Figures 24** and **41**). It is the combined characteristic response of loading rate and AE rate with time which can provide quantitative indication of σ_{crit} as loading rate and AE rate correlate well with particle size analysis.

The loading rate as function of load for different concentrations was analyzed and plots for [1] and [4] are shown in **Figure 39**. Note the pressure after which the loading rate starts to decrease is ≈ 2500-3000 psi for [1] and ≈ 5000-5500 psi for [4]. σ_{crit} determined for different concentrations coincides with pressure determined through loading rate. In conclusion, loading rate change (as function of load) is quantitative indicator of σ_{crit}.

Percent crush as function of axial pressure (using data from **Figures 35(b), 36(b)** and **37(b)**) is shown in **Figure 38**. Fines here refer to particles smaller than 40 mesh. The quantity of fines generated at [4] is less than generated at [2] over the entire pressure range (see **Figure 38**). Similarly, fines generated at [2] are less as compared to [1]. Fewer fines are generated with increase in concentration over the entire pressure range. Note that fines start to generate at 2500 psi for [1], 4000 psi for [2] and 5500 psi for [4]. In summary, σ_{crit} increases with increase in proppant concentration.

Microscope images captured as function of pressure for different concentrations aid in visualizing proppant behavior in bulk, i.e., how different concentrations respond to applied pressure. Two images at axial pressure of 15000 psi are shown in **Figure 40**; the left image represents [1] and right image represents [4]. The [4] proppant pack is ≈ 4 times as thicker than [1] assuming packing is same. The 20/40 mesh Ottawa sand crushed uniformly at [1]; while at [4], grains crushed non-uniformly and preferentially at steel- proppant interface.

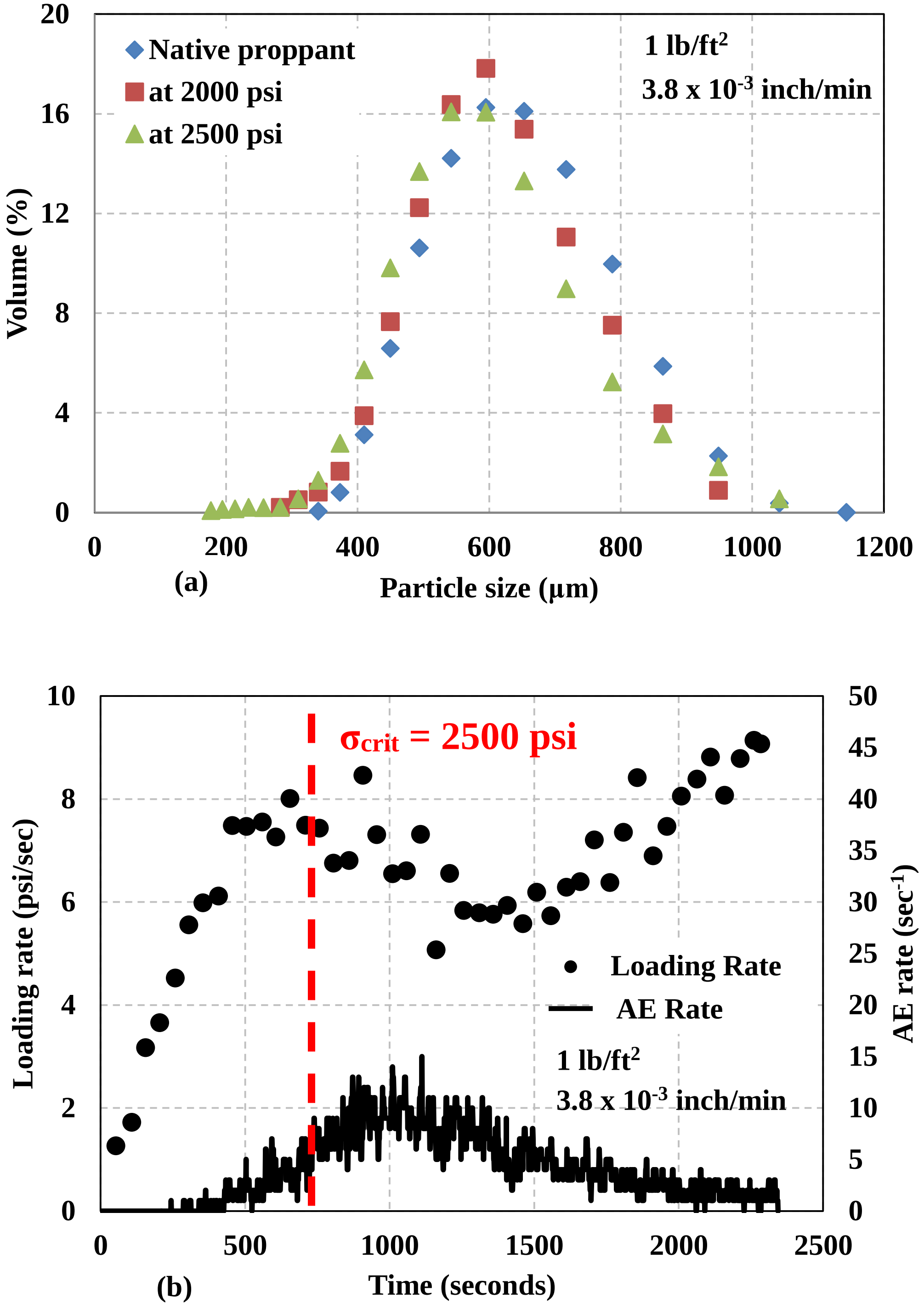

Figure 35: (a) Particle size analysis as function of pressure for concentration of 1 lb/ft^2. σ_{crit} is 2500 psi. (b) Loading rate (circle) and AE rate (line) as function of pressure. Red line indicates σ_{crit} for concentration of 1 lb/ft^2 of 20/40 mesh Ottawa sand.

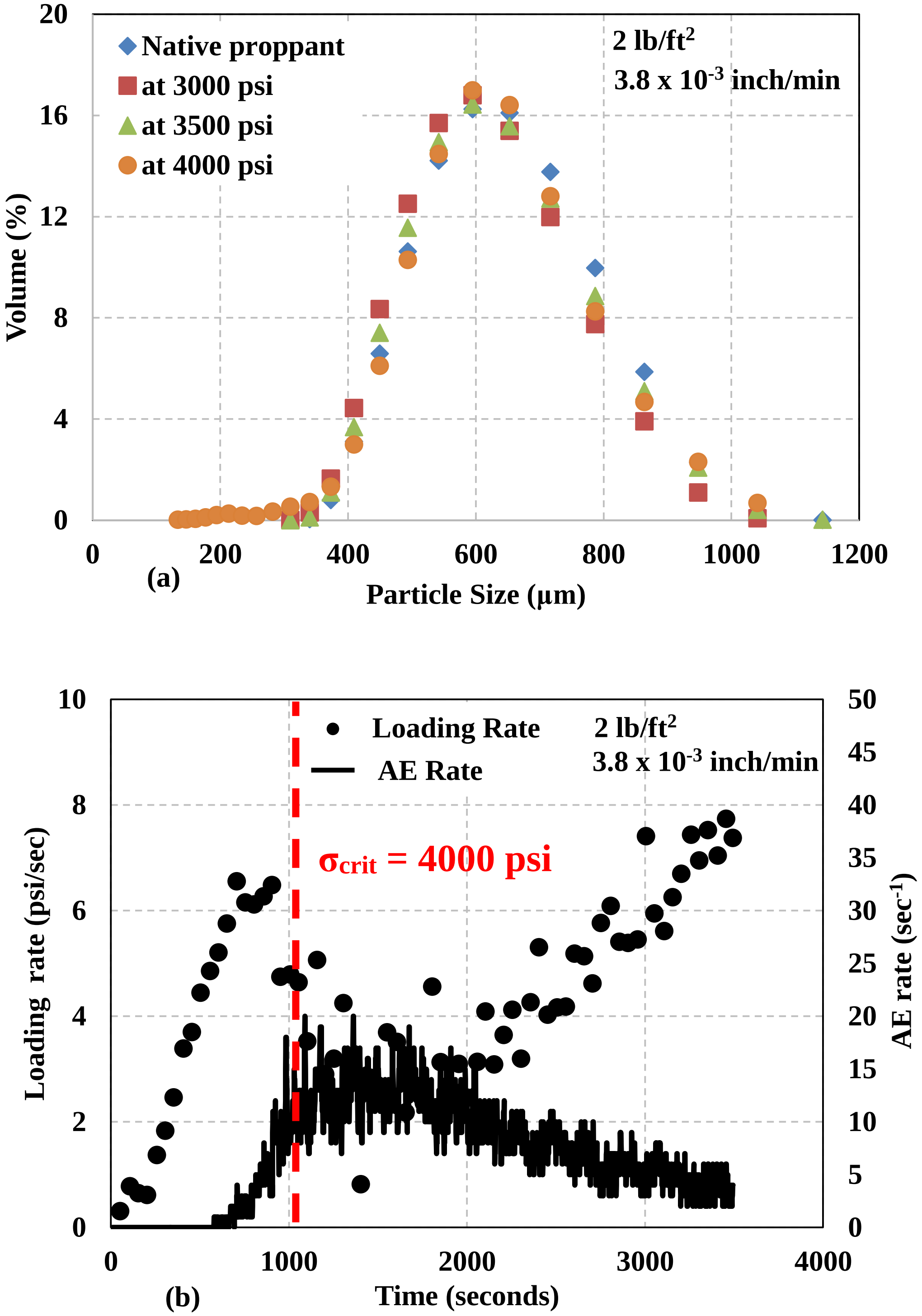

Figure 36: (a) Particle size analysis as function of pressure for concentration of 2 lb/ft^2. σ_{crit} is 4000 psi. (b) Loading rate (circle) and AE rate (line) as function of pressure. Red line indicates σ_{crit} for concentration of 2 lb/ft^2 of 20/40 mesh Ottawa sand.

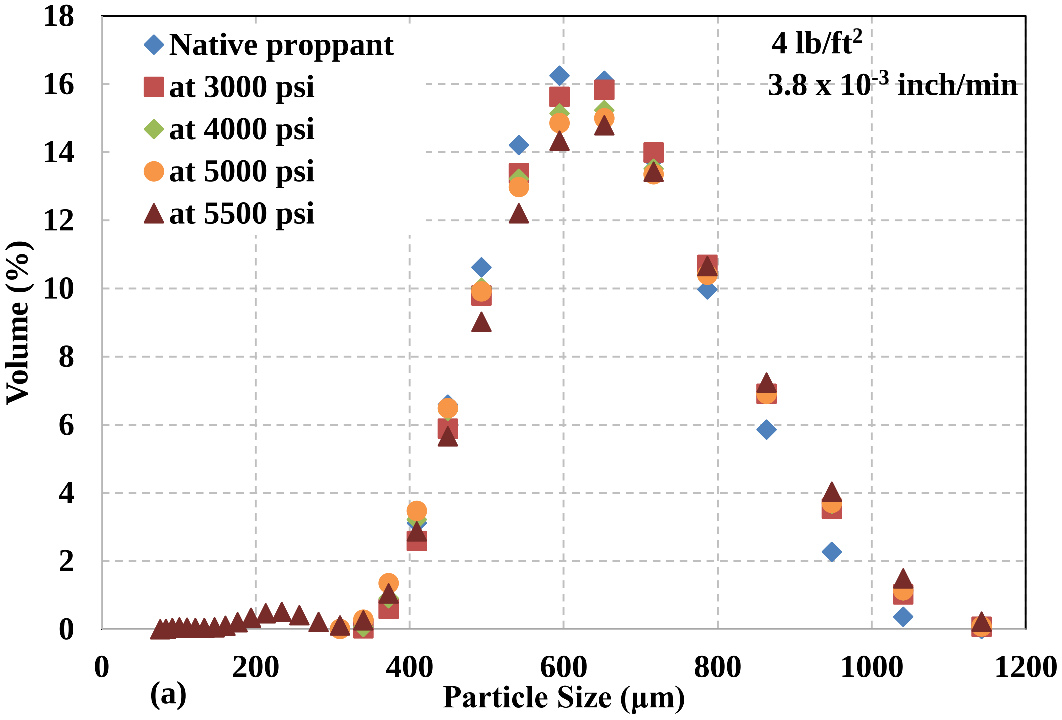

(a)

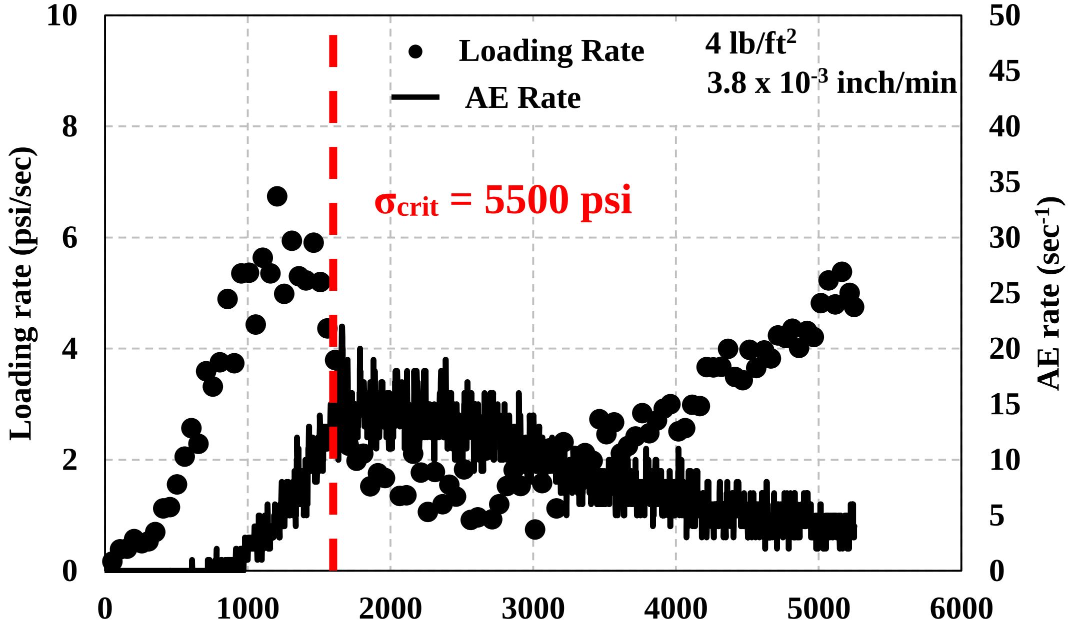

(b)

Figure 37: (a) Particle size analysis as function of pressure for concentration of 4 lb/ft^2. σ_{crit} is 5500 psi. (b) Loading rate (circle) and AE rate (line) as function of pressure. Red line indicates σ_{crit} for concentration of 4 lb/ft^2 of 20/40 mesh Ottawa sand.

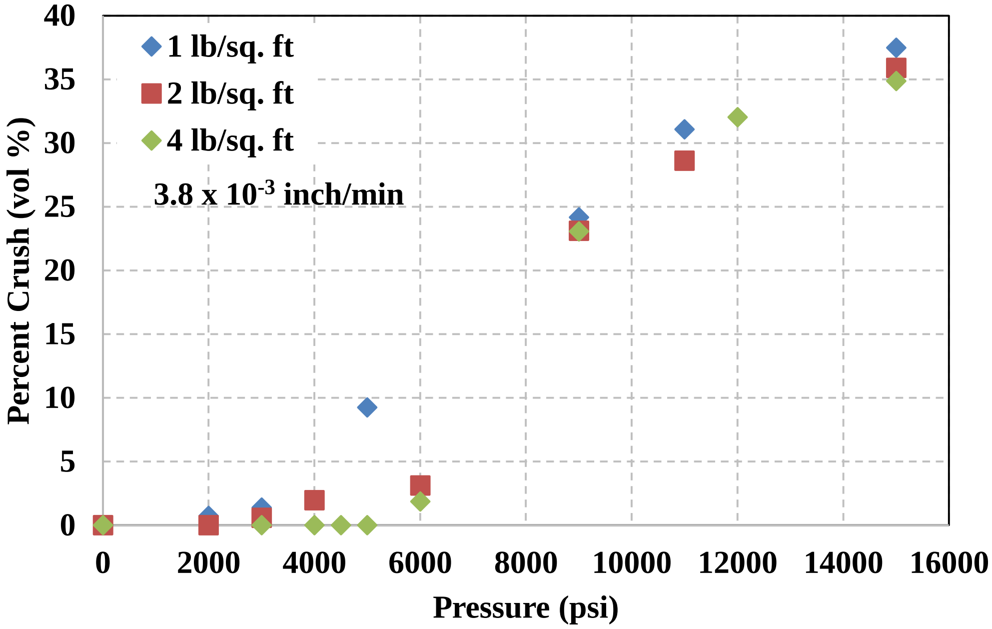

Figure 38: Percent crush as function of pressure and concentration of 20/40 mesh Ottawa sand. Percent crush is less at concentration of 4 lb/ft^2 in comparison to percent crush at concentration of 1 and 2 lb/ft^2. Note fines start to be generated at higher pressure with increased concentration.

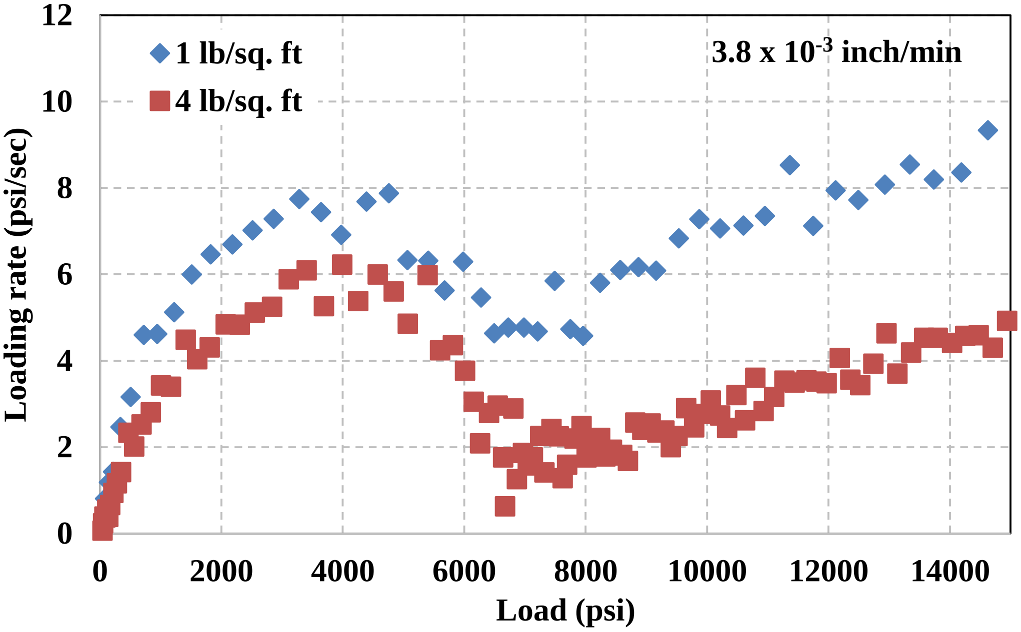

Figure 39: Loading rate as function of load for two different concentrations – concentration of 1 and 4 lb/ft^2. Notice the pressure at which loading rate starts to decrease is different for two concentrations.

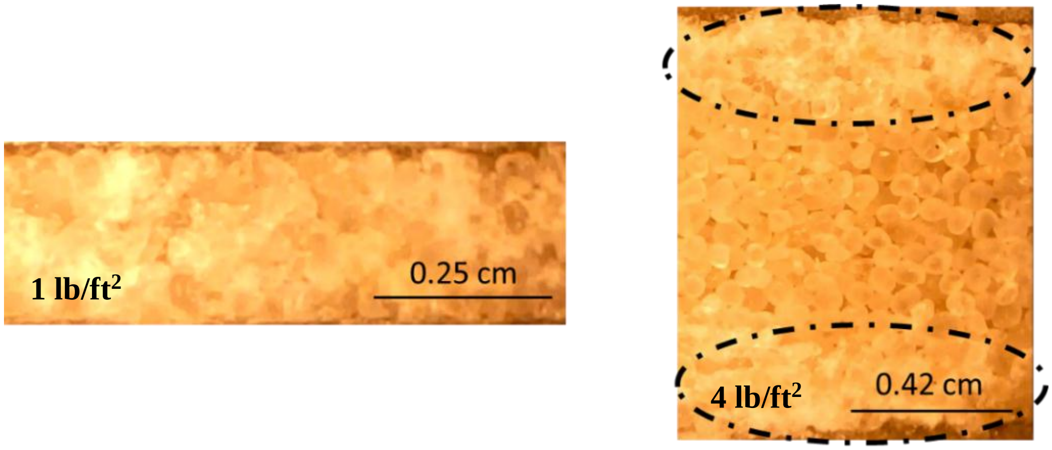

3.8 x 10^{-3} inch/min

Figure 40: Microscope images of concentration of 1 and 4 lb/ft^2 at 15000 psi. Crushing is uniform in case of concentration of 1 lb/ft^2. Crushing is non-uniform and primarily concentrated at steel-proppant interface for concentration of 4 lb/ft^2.

Microscope images (see **Figure 40**) were used to measure the proppant pack width as function of axial pressure. This width (height) was used to compute the bulk volume of the proppant pack (knowing the crush cell cross-sectional area). Porosity as function of pressure was computed using the bulk volume and grain volume (computed from grain density and mass). Porosity reduction and compaction for [1] and [4] are plotted as function of pressure in **Figure 41**. The porosity decreased by 33.3% (at 13000 psi) of the initial porosity (at 100 psi) for [1] of 20/40 mesh Ottawa sand. Similarly for [4] of 20/40 mesh Ottawa sand, the porosity decreased by 25% (at 13000 psi) of the initial porosity (at 100 psi). The decrease in porosity with increase in pressure is greater for [1] than [4]; lower concentration experiences a greater percentage decrease in porosity. The width retained for [1] is 82.3% (at 13000 psi) of initial width (at 100 psi) and for [4], 86% (at 13000 psi) of initial width (at 100 psi) is retained; lower proppant concentration experiences greater compaction.

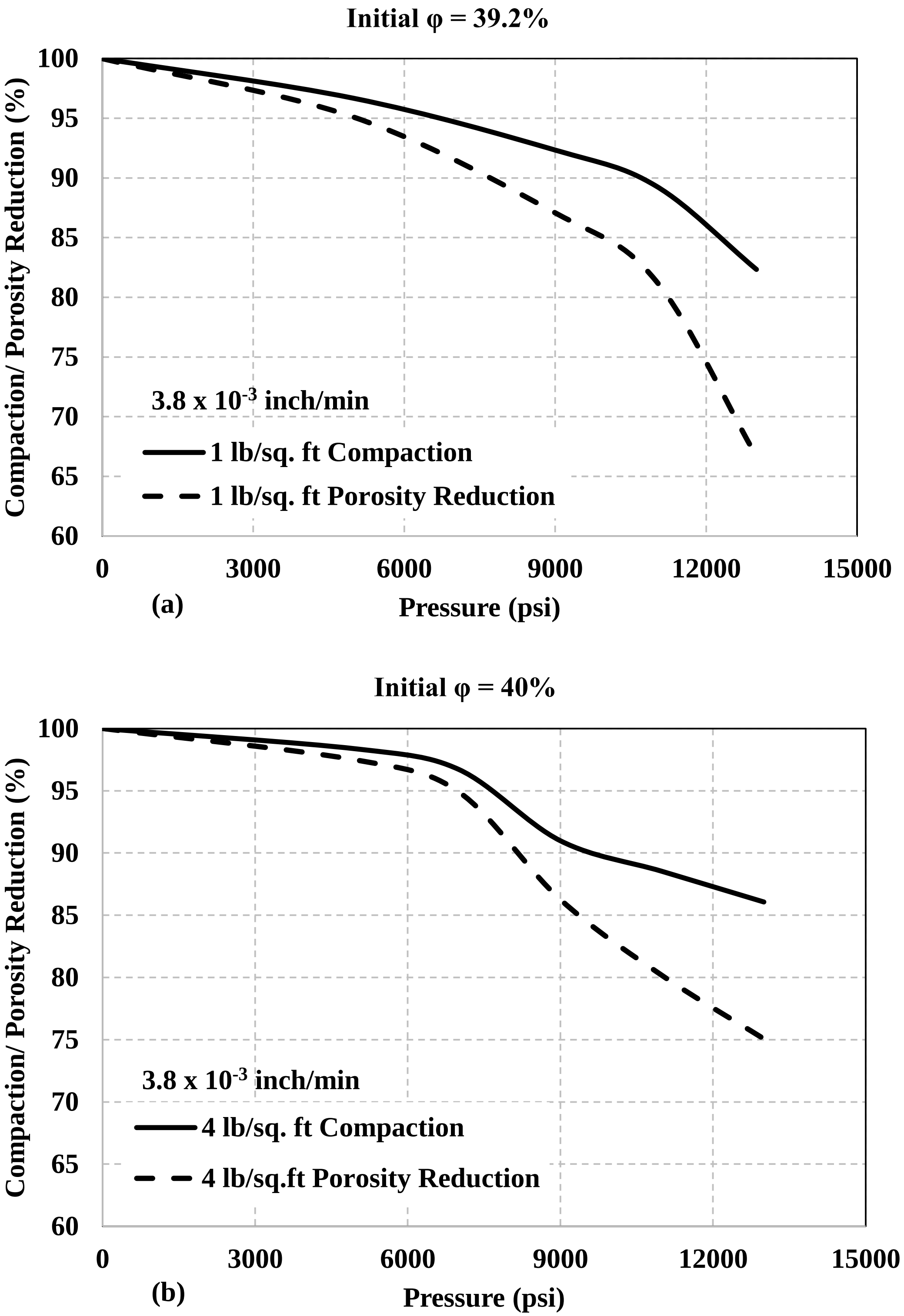

Figure 41: Compaction and porosity reduction as function of pressure for concentration of (a) 1 lb/ft^2 (b) 4 lb/ft^2. Compaction and porosity reduction is greater for concentration of 1 lb/ft^2 than 4 lb/ft^2.

3.5.2 Discussion

We concluded that the σ_{crit} at which grain starts to fracture is function of proppant concentration (see **Section 3.4.2**). There were other second-order effects such sorting and heterogeneity that were not considered in the model to predict the pressure at which grains start to crush (Zhang et al., 1990). However, the proppant pack concentration has a substantial effect on σ_{crit}; a model incorporating proppant concentration is needed.

3.5.3 Investigation of repeatability

Tests on different proppant concentrations with constant $\Delta_{3.8}$ were conducted thrice to investigate the repeatability of σ_{crit}. Results of the tests for [1], [2] and [3] are shown in **Figures 42 and 43**. The plots are scaled identically for comparison and interpretation. Tests conducted on [1] take less time to reach 15000 psi compared to [4] tests. The duration of the tests indicate how steep the load increase is for different proppant concentrations; higher loading rate for lower proppant concentration and vice-versa. Note that the plot gives similar indication for the σ_{crit} for all the three concentrations (see **Figure 43**). From **Section 3.5.1**, σ_{crit} is coincident with a decrease in loading rate; a similar behavior is observed in **Figure 43**. There are some variations between the three test runs which can be attributed to second-order effects. σ_{crit} at which proppant starts to crush is quite repeatable (± 300 psi).

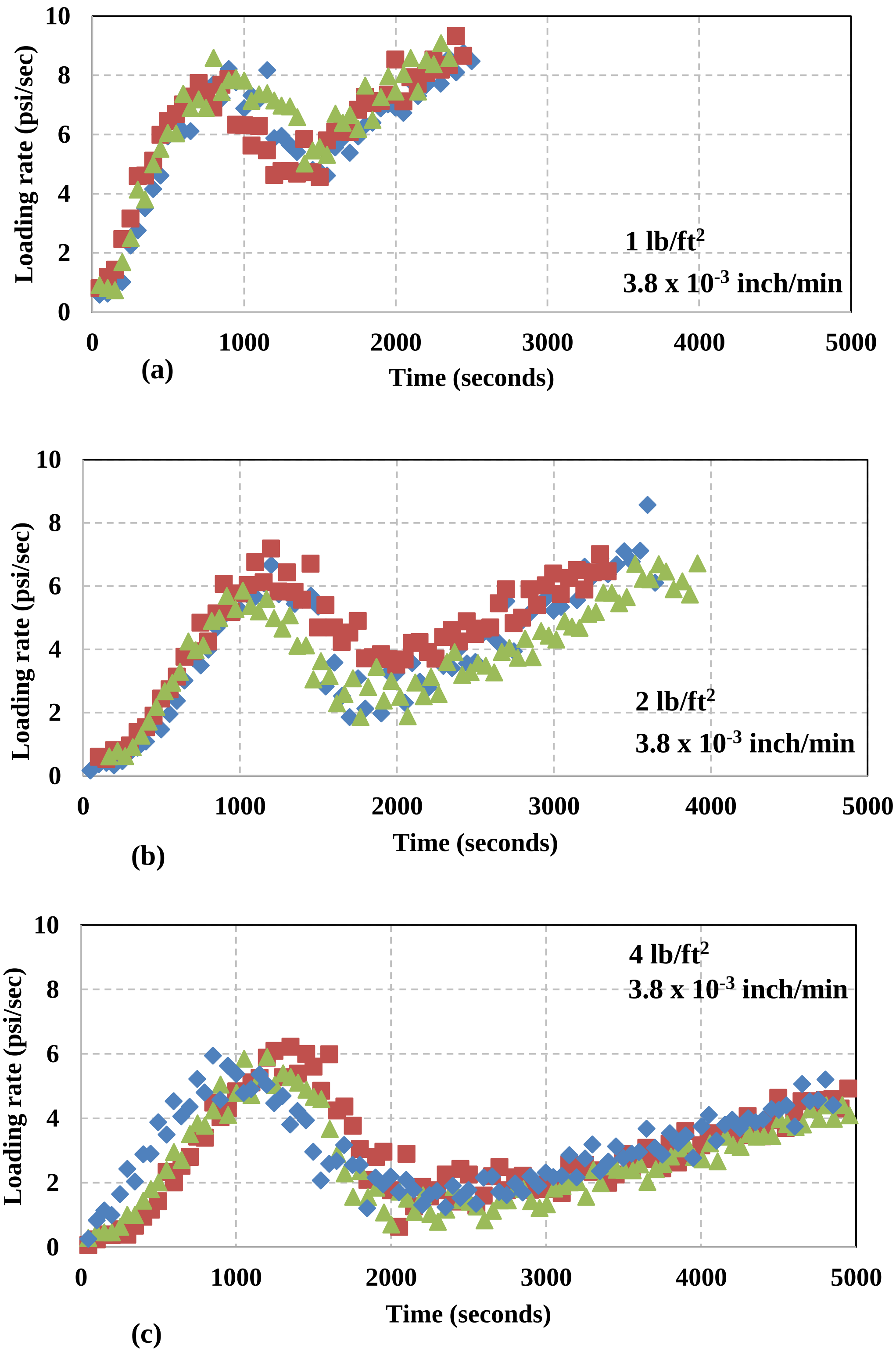

Figure 42: Loading rate as function of time for three different concentrations: (a) 1 lb/ft^2, (b) 2 lb/ft^2 and (c) 4 lb/ft^2. The test is quite repeatable for the three concentrations.

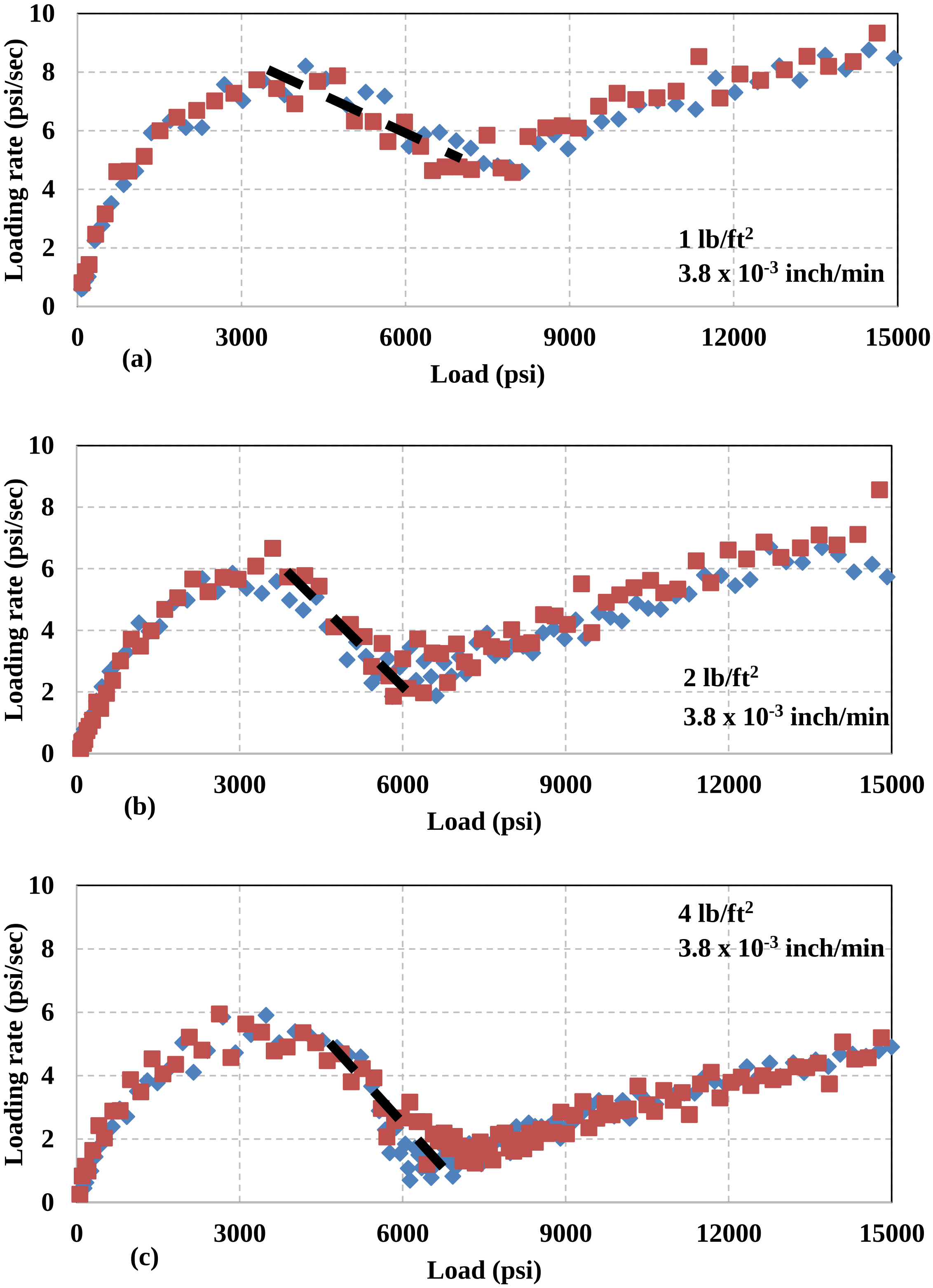

Figure 43: Loading rate as function of load for three different concentrations: (a) 1 lb/ft^2, (b) 2 lb/ft^2 and (c) 4 lb/ft^2. The test is quite repeatable for the three concentrations (± 300 psi).

3.6 Effect of displacement rate

20/40 mesh Ottawa sand was tested at two displacement rates to study the effect on σ_{crit}. Comparison of different displacement rates are made at two different concentrations: [2] and [4]. The test matrix is shown in **Table 3**.

Table 3: Test matrix for the crush test showing the proppant type and displacement rates used for 3 different concentrations of 20/40 mesh Ottawa sand: 1, 2 and 4 lb/ft^2.

Proppant type →	**20/40 mesh Ottawa sand**		
Displacement rate ↓	**[1]**	**[2]**	**[4]**
$\Delta_{3.8}$	✓	✓	✓
$\Delta_{11.5}$		✓	✓

A displacement rate of $\Delta_{3.8}$ was using in previous tests on 20/40 mesh Ottawa sand to investigate the effect of proppant concentration. The displacement rate was increased to thrice the initial rate to $\Delta_{11.5}$ to evaluate the effect of loading rate. **Figures 44(a)** and **45(a)** shows particle size analysis as function of pressure; loading rate and AE rate as function of time are shown in **Figures 44(b)** and **45(b)** for [2] and [4], respectively. Test durations were reduced with increased displacement rate (see **Figures 38, 39, 44 and 45**). Loading rate and AE rate have similar characteristic response to the test conducted at lower displacement rate. The σ_{crit} of 20/40 mesh Ottawa sand for different concentrations at increased displacement rate is determined through the particle size analysis. Red lines in **Figures 44** and **45** indicate σ_{crit} for respective concentrations. Note that at $\Delta_{11.5}$ and [2] of 20/40 mesh Ottawa sand starts to crush at a similar pressure of 4000 psi as for $\Delta_{3.8}$ (see **Figures 38 and 44**). Similarly, at $\Delta_{11.5}$ and [4] of 20/40 mesh Ottawa sand starts to crush at a similar pressure of 5500 psi as for $\Delta_{3.8}$ (see **Figures 39**

and 45). It appears from these tests that displacement rate might not be a factor in conducting proppant crush test. However, further research is required to determine the effect of displacement rate on crush strength of proppant.

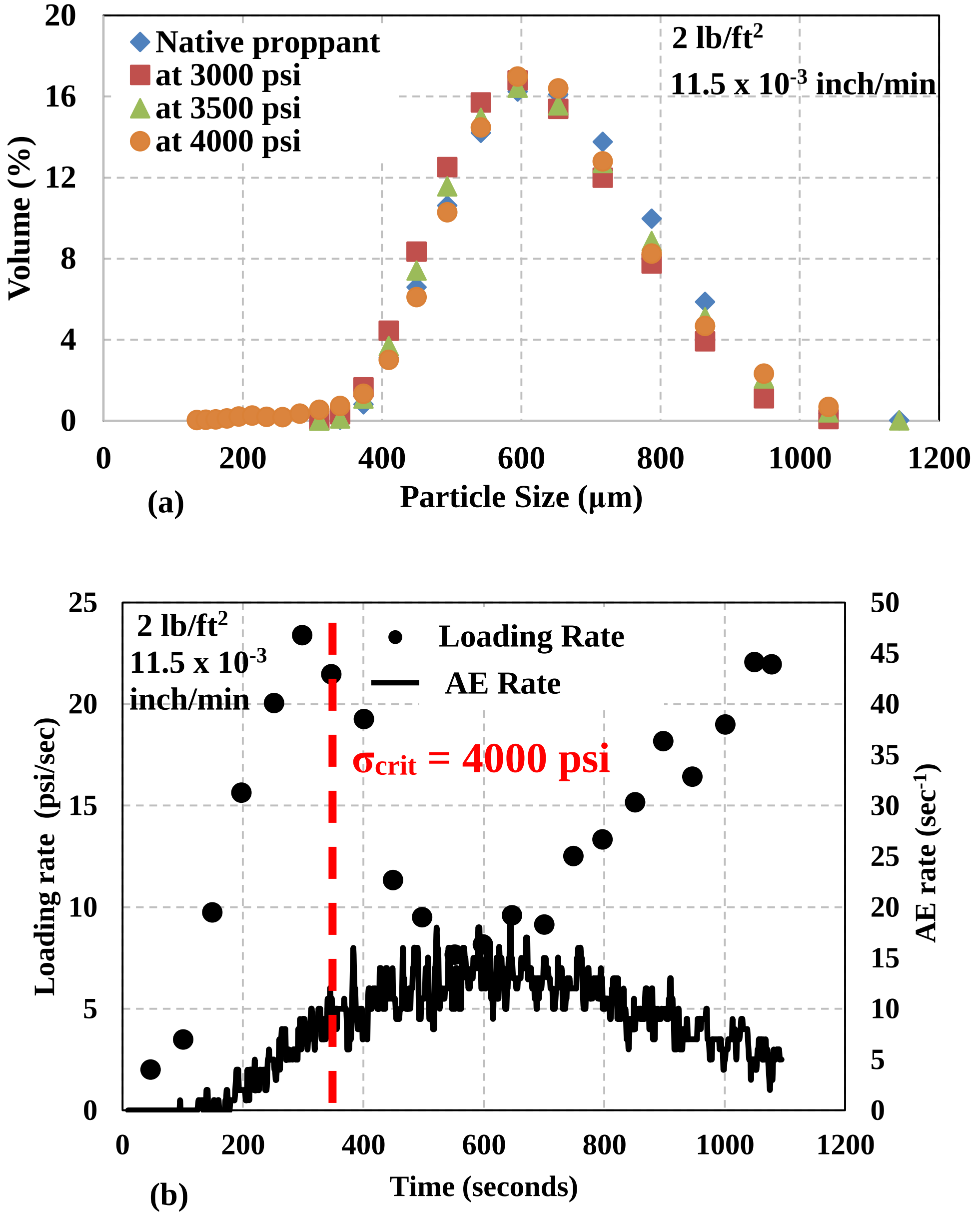

Figure 44: (a) Loaded particle size analysis as function of pressure for concentration of 2 lb/ft^2 of 20/40 mesh Ottawa sand at $\Delta_{11.5}$. σ_{crit} is 4000 psi. (b) Loading rate (circle) and AE rate (line) as function of time at $\Delta_{11.5}$. Red line indicates σ_{crit} for concentration of 2 lb/ft^2 of 20/40 mesh Ottawa sand.

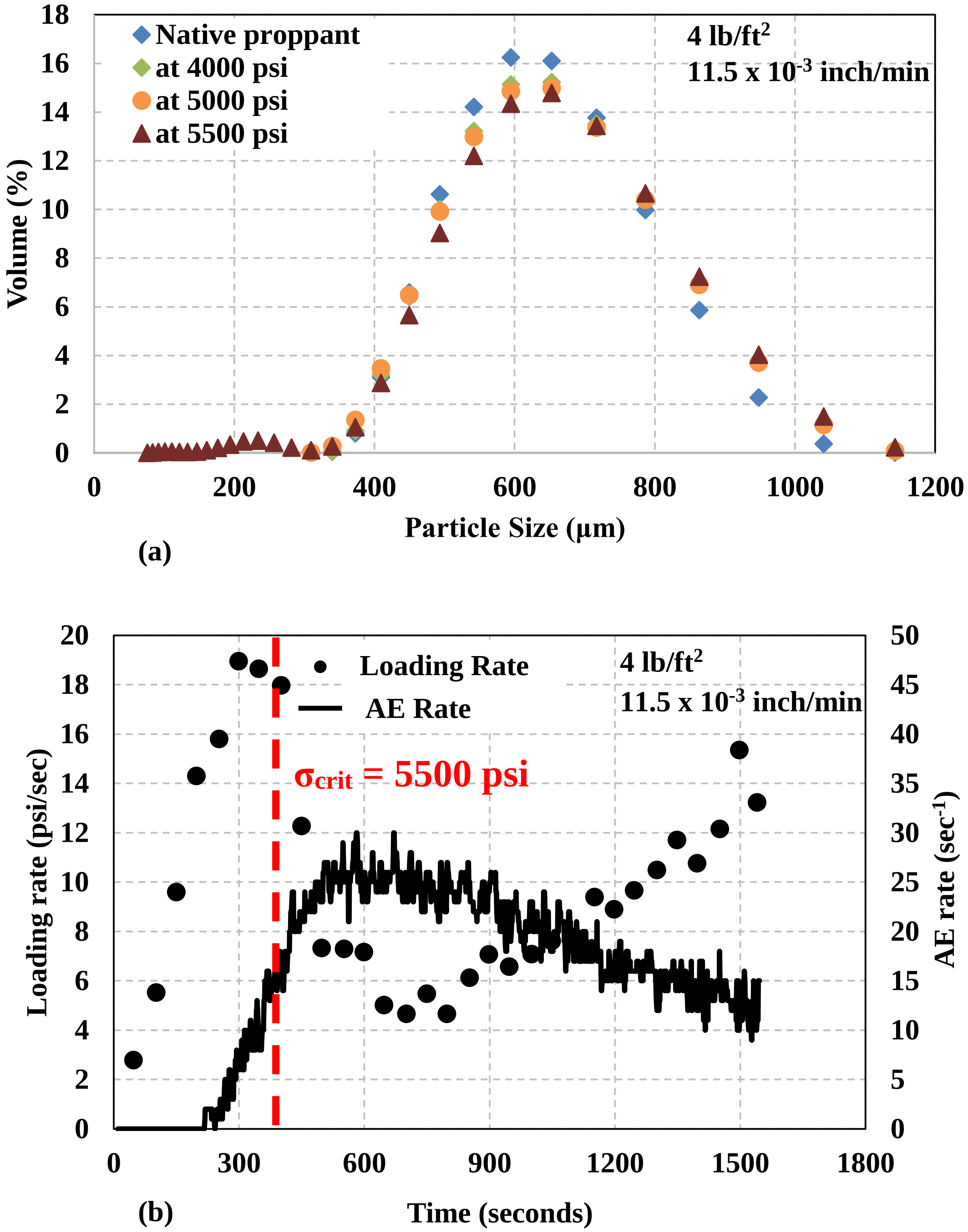

Figure 45: (a) Loaded particle size analysis as function of pressure for concentration of 4 lb/ft^2 of 20/40 mesh Ottawa sand at $\Delta_{11.5}$. σ_{crit} is 5500 psi. (b) Loading rate (circle) and AE rate (line) as function of time at $\Delta_{11.5}$. Red line indicates σ_{crit} for concentration of 4 lb/ft^2 of 20/40 mesh Ottawa sand.

3.7 Effect of proppant type

Four different proppants were tested: CarboNRT, Ottawa sand, CarboHSP and CarboProp - to determine dependence of σ_{crit} on proppant type. CarboNRT, CarboHSP and CarboProp were obtained from trial samples provided by the vendor, Carboceramics. All the proppants mentioned above are 20/40 mesh proppants but with different particle size distributions. The testing of different proppants was carried out to investigate the application of our methodology.

The proppant concentration used for these tests is the same for all four proppants i.e. [2]. Load is increased at constant $\Delta_{11.5}$. Higher displacement rate was used because the observations were similar to $\Delta_{3.8}$ but is a shorter test time. **Figures 46, 47, 48 and 49** shows loading rate and AE rate as function of time; particle size distribution as function of pressure for CarboNRT, Ottawa sand, CarboHSP and CarboProp, respectively.

The characteristic responses for loading rate and AE rate for CarboNRT are similar to that of Ottawa sand. However, note that the duration of each test is different and duration depends on the characteristics of each proppant's crush resistance. Behavior should also be dependent on proppant concentration but we only tested at [2]. The decrease in loading rate after reaching peak loading rate can be interpreted as the proppant pack undergoing grain crushing and subsequently compaction. Zhang et al., (1990) indicated that grain crushing provides additional degrees of freedom for rotation and movement, and hence, the pack is able to compact more; subsequently pressure increases gradually at a constant displacement rate which results in a loading rate decrease as function of time, see **Section 3.5.1**). Post-test particle size analysis showed that CarboNRT (see **Figure 46**) and Ottawa sand (see **Figure 47**) underwent crushing at 15000 psi. The crushed proppant pack has a bimodal particle size distribution for CarboNRT and Ottawa sand; thereby, confirming our inference from loading rate and AE rate as function of time. For CarboNRT, the mean particle size decreased from 791 μm (native) to 577 μm at 15000 psi. Similarly, the mean particle size decreased from 678 μm (native) to 442 μm at 15000 psi for Ottawa sand.

For CarboHSP and CarboProp, we observe that the loading rate starts to decrease after reaching the peak loading rate. But, we do not observe continued decrease in loading rate followed by an increase after reaching the minimum. The decrease in loading rate with time captures grain rearrangement associated with grain crushing (see **Section 3.5.1**). The observation of the decrease in loading rate after reaching peak loading rate is suggestive of the onset of grain crushing and subsequent compaction. σ_{crit} for CarboHSP and CarboProp at [2] is about 14000 psi. Similarly, AE rate also increases with time but does not decrease (different from AE rate with time for CarboNRT and Ottawa sand). Particle size analysis confirms this. Particle size distribution as function of pressure shows mean particle size reduction from 746 μm (native) to 709 μm at 15000 psi for CarboHSP and 736 μm (native) to 676 μm at 15000 psi for CarboProp. Ceramic HSP and Ceramic Prop undergo less crushing compared to Ceramic NRT and Ottawa sand at [2]. Thus, loading rate and AE rate can be used as qualitative indicator for identifying σ_{crit}.

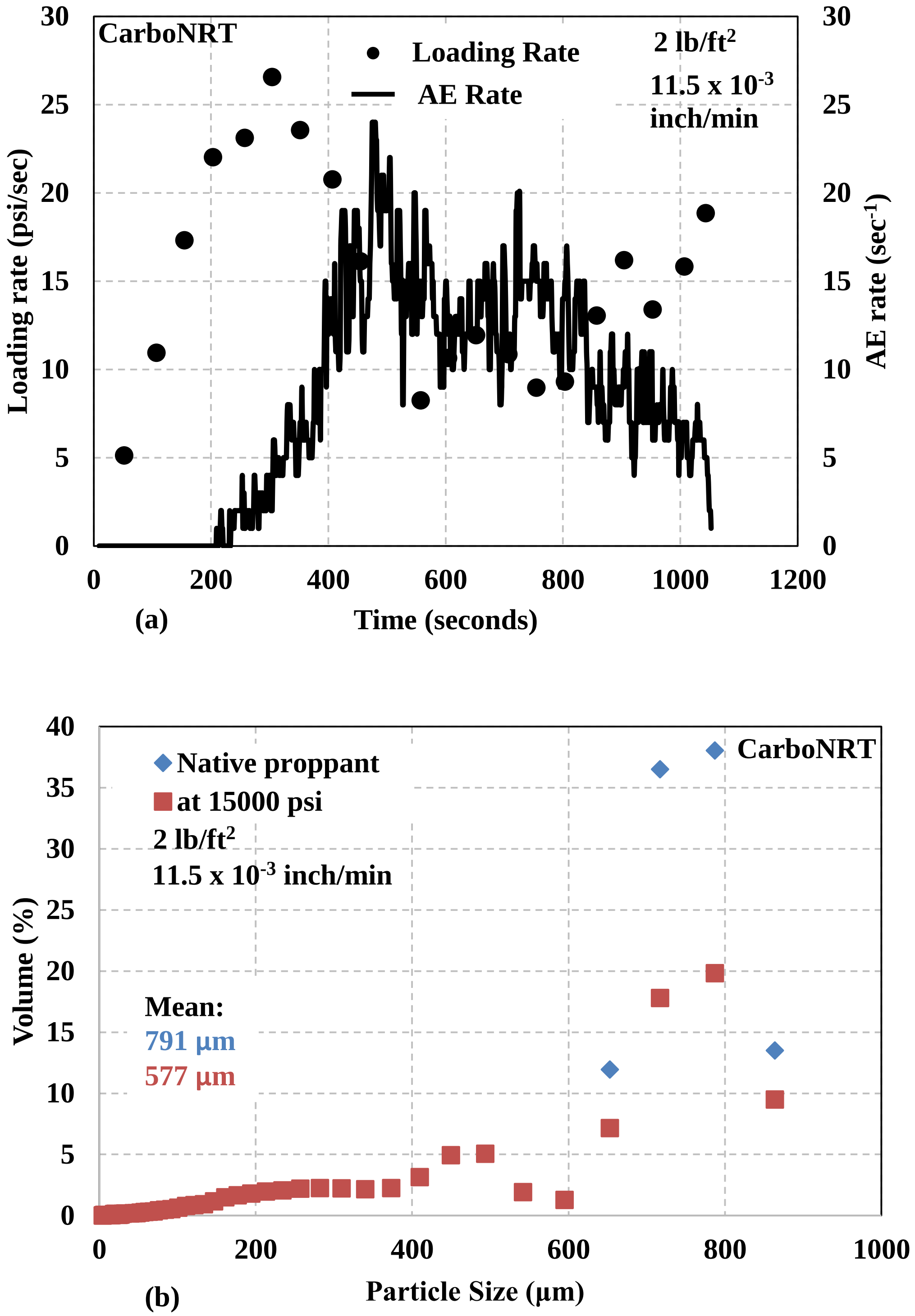

Figure 46: (a) Loading rate (circle) and AE rate (line) as function of time for CarboNRT proppant at concentration of 2 lb/ft^2. Loading rate just starts to decrease at σ_{crit} = 5000 psi. (b) Particle size analysis at 15000 psi and native proppant for CarboNRT. Fines start generating well before 15000 psi. At 15000 psi, the mean particle size reduces from 791 µm to 577 µm.

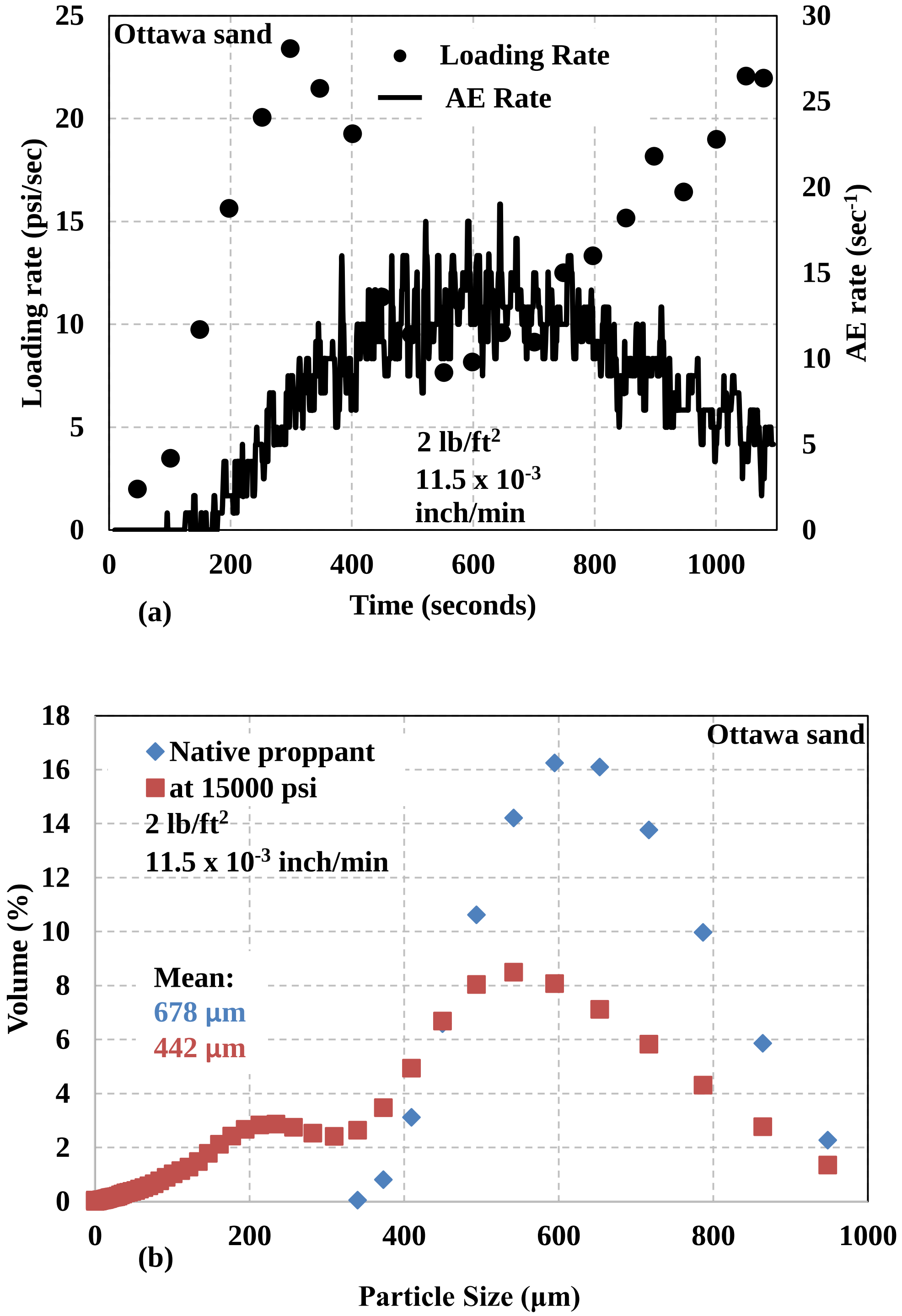

Figure 47: (a) Loading rate (circle) and AE rate (line) as function of time for Ottawa sand at concentration of 2 lb/ft^2. Loading rate starts to decrease at $\sigma_{crit} \approx$ 4000 psi. (b) Particle size analysis at 15000 psi and native proppant for Ottawa sand. Fines start generating well before 15000 psi. At 15000 psi, the mean particle size reduces from 678 µm to 442 µm.

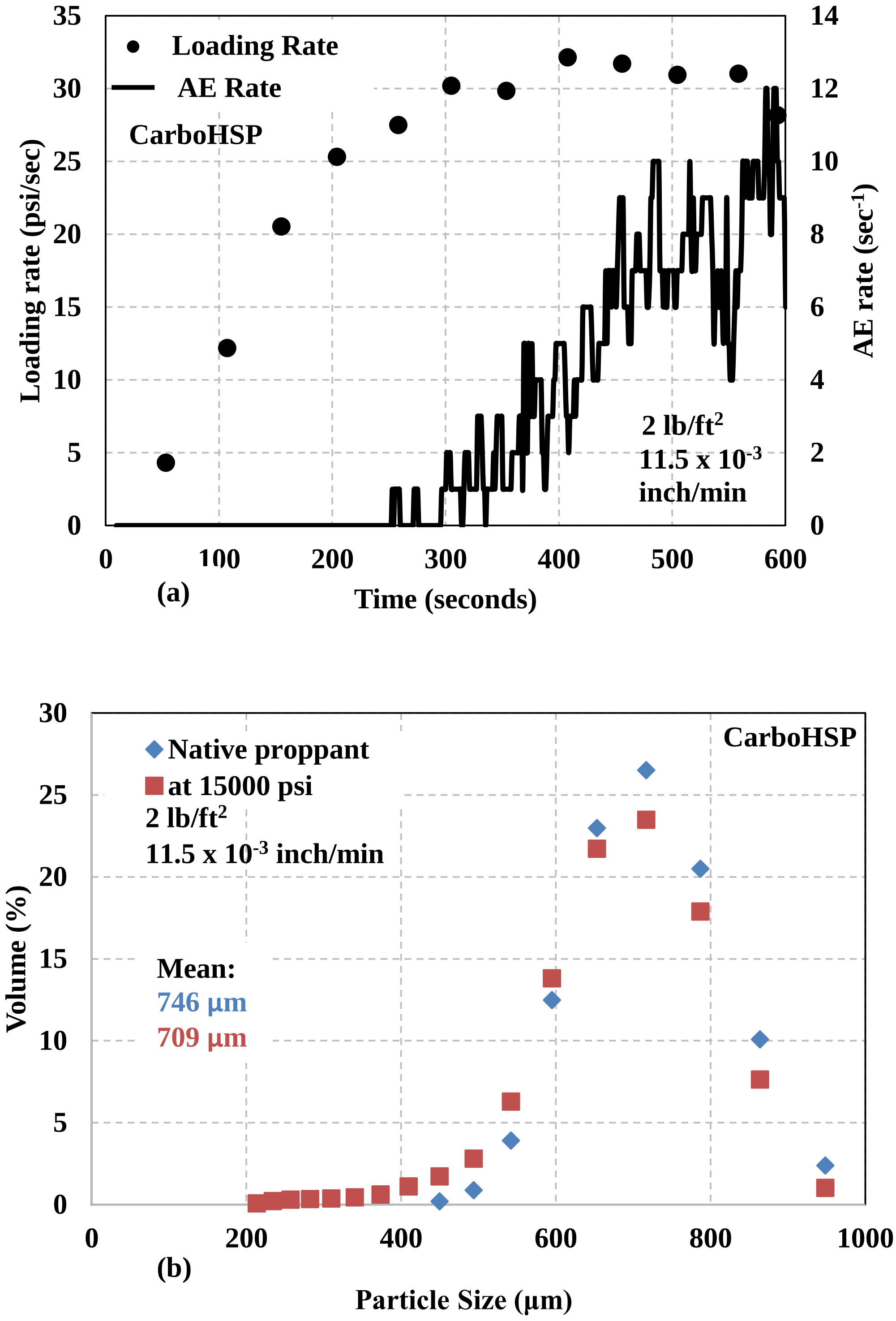

Figure 48: (a) Loading rate (circle) and AE rate (line) as function of time for CarboHSP proppant at concentration of 2 lb/ft^2. Loading rate just starts to decrease at σ_{crit} ≈ 14000-14500 psi. (b) Particle size analysis at 15000 psi and native proppant for CarboHSP. Fines start generating around 14000 psi.

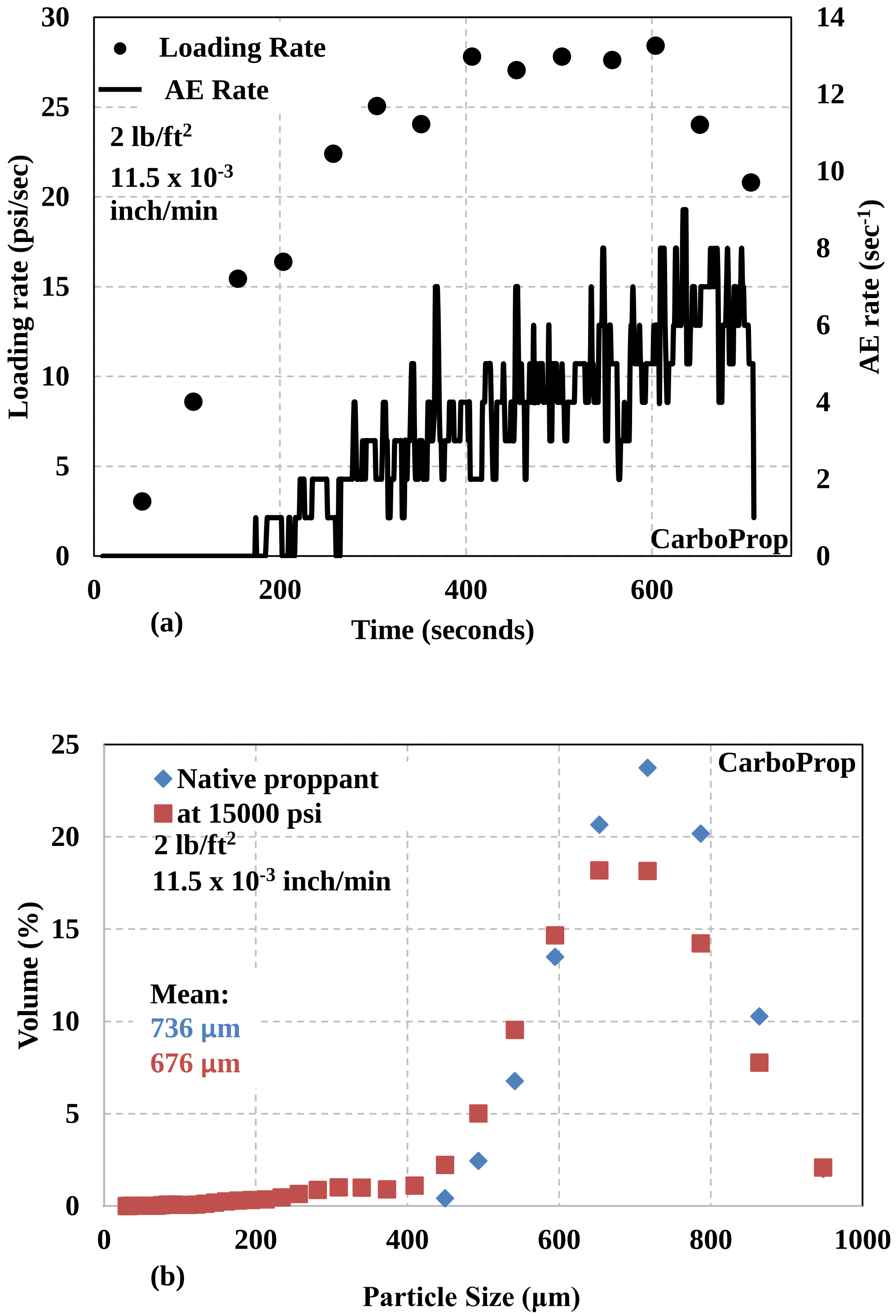

Figure 49: (a) Loading rate (circle) and AE rate (line) as function of time for CarboProp proppant at concentration of 2 lb/ft^2. Loading rate just starts to decrease at $\sigma_{crit} \approx$ 14000-14500 psi. (b) Particle size analysis at 15000 psi and native proppant for CarboProp. Fines start generating around 15000 psi.

3.8 Effect of cyclic loading

3.8.1 Results

20/40 mesh Ottawa sand at [4] was used to study the effect of cyclic loading. Proppant was loaded to 15000 psi at constant $\Delta_{11.5}$ twice. Higher displacement rate was used to reduce testing time without sacrificing behavior. **Figure 50** shows pressure and AE rate as function of time for both the 1st and 2nd cycle.

For 1st cycle, pressure was increased to 15000 psi and unloaded at constant $\Delta_{11.5}$ (shown by dotted blue, see **Figure 50**). AE rate corresponding to this cycle is shown by solid blue in **Figure 50**. Note pressure and AE rate show similar signature as previous tests (see **Sections 3.5** and **3.6**). Also, there are relatively few AE events while unloading. Particle size analysis was performed after the proppant pack was unloaded and the point after unloading is denoted as “1” in **Figure 50.** Particle size distribution corresponding to “1” is shown in **Figure 51** (denoted as “1”).

A 2nd test was carried out to reproduce the 1st cycle. For the 2nd cycle, pressure was increased to 15000 psi and unloaded at constant $\Delta_{11.5}$ (shown by dotted blue, see **Figure 50**). AE rate was monitored during the 2nd cycle and is shown by solid blue in **Figure 50**. Note there are relatively fewer AE events during 2nd cycle compared to cycle 1. Particle size analysis was performed once the proppant pack was unloaded after cycle 2 and the point after unloading is denoted as “2” in **Figure 50.** Particle size distribution corresponding to “2” is shown in **Figure 51** (denoted as “2”). There is a insignificant increase in volume of fines due to stress cycling.

Another single cycle crush test was carried out, but, proppant was removed from the crush cell and mixed (no new proppant was added). Mixing was done to achieve different proppant packing inside the crush cell. The mixed crushed proppant was poured in crush cell and pressure was increased to 15000 psi and unloaded at the constant $\Delta_{11.5}$ (shown by dashed green, see **Figure 50**). AE rate was monitored and is shown by solid green in **Figure 50**. Again, we observe relatively fewer AE events compared to cycle 1. Particle size analysis was performed once the proppant pack was unloaded and the point after unloading is denoted as “3” in **Figure 50.** Particle size distribution corresponding to “3” is shown in **Figure 51** (denoted as “3”).

There is a significant difference in particle size distribution between native and post-test proppant pack obtained after cycle 1. However, there is insignificant difference in particle size distribution for “1”, “2” and “3”. Cyclic loading does not appear to have a significant effect on mean particle size of post-test proppant. We observe that AE rate is correlated with proppant crushing. More experimental work as function of proppant concentration, type, displacement rate and target stress needs to be done to establish that stress cycling does not affect proppant crushing.

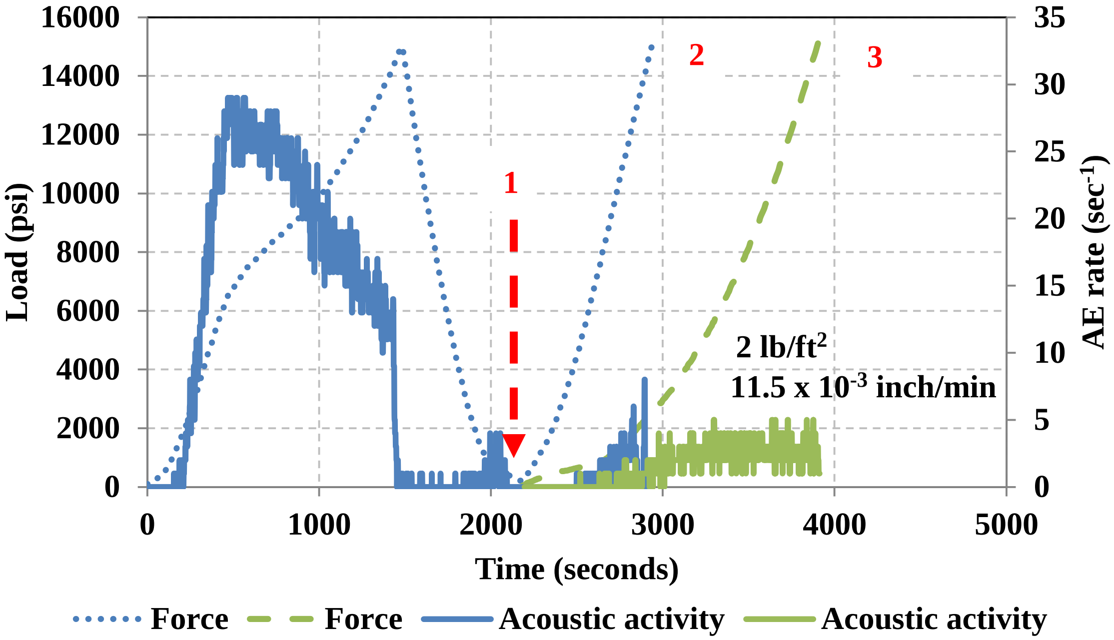

Figure 50: Load and AE rate as function of time at concentration of 2 lb/ft^2 of 20/40 mesh Ottawa sand. Dotted blue represents pressure increase to 15000 psi, then decrease to 15000 psi and then, increase to 15000 psi at constant $\Delta_{11.5}$. Solid blue is AE rate corresponding to dotted blue. Dashed green represents increase in load to 15000 psi on the proppant pack in which crushed proppant was taken out of crush cell and mixed. Solid green is AE rate corresponding to dashed green.

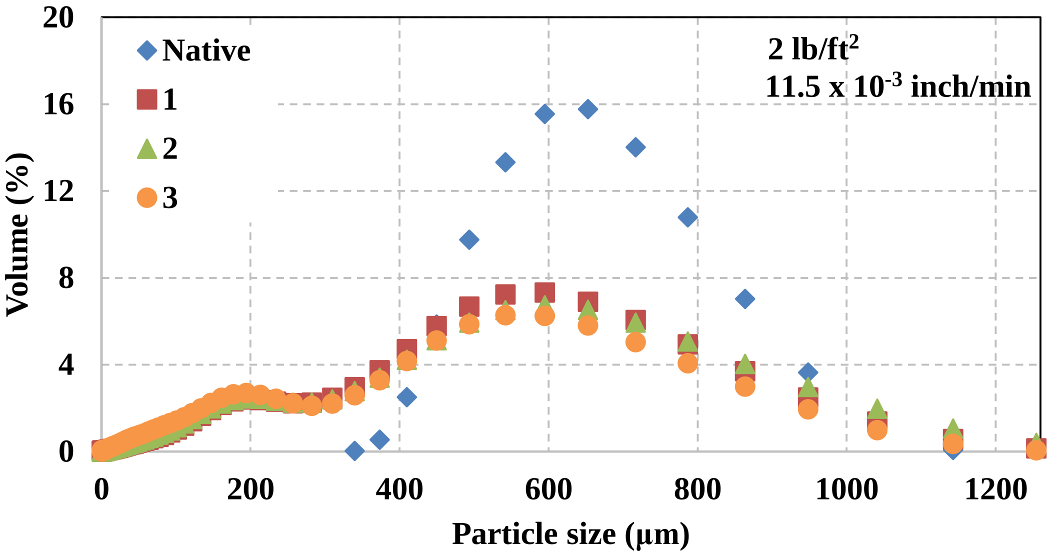

Figure 51: Particle size distribution for post-test proppant (concentration of 2 lb/ft^{2}of 20/40 mesh Ottawa sand) obtained at “1”, “2” and “3” compared to native particle size distribution. Proppant is significantly crushed at “1” compared to native proppant size distribution. No significant difference in proppant crushing in post-test proppant obtained at “1”, “2” and “3”.

3.8.2 Discussion

Schubarth et al., (2004) investigated the effect of stress cycling on median particle diameter (MPD) by conducting API test (see **Section 1.4.2**). Plot of retained MPD as function of closure pressure for stress cycles 1, 5 and 20 is shown in **Figure 52**. Note that the stress cycles do change the MPD. **Figure 50** presents two stress cycles compared to 5 and 20 stress cycles performed by Schubarth et al., (2004). Schubarth et al., (2004) found that the change in MPD does not affect permeability significantly using correlation provided by Berg, (1970), not by direct measurement.

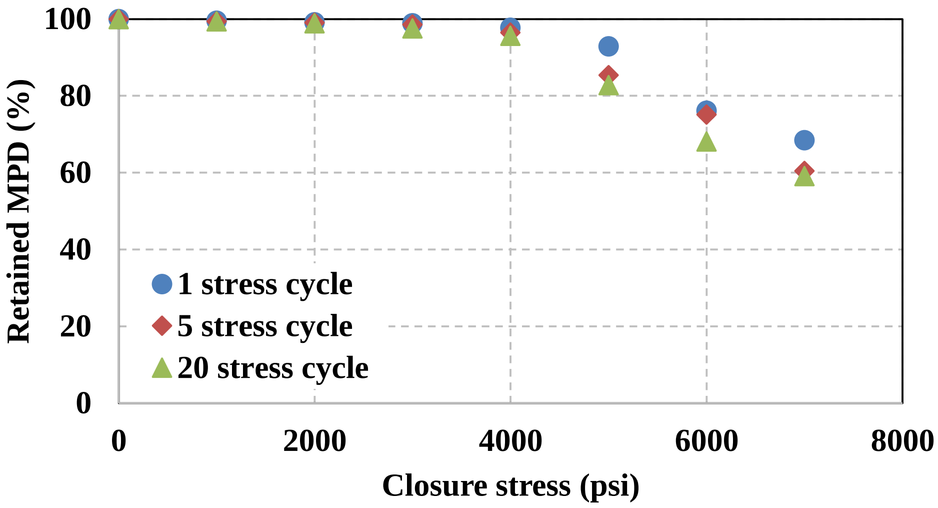

Figure 52: Retained median particle diameter (MPD) as function of closure stress and stress cycles for 20/40 mesh sand with MPD of 0.52 mm(Schubarth et al., 2004).

3.9 Effect of fracture morphology

3.9.1 Motivation

Proppant is used to maintain fracture conductivity after fracture initiation. But, hydraulic fractures often have an undocumented surface topography caused by asperities. Schematic of a fracture with exaggerated surface roughness is shown in **Figure 53** (adapted from Kassis and Sondergeld, 2010).

Scanning Electron Microscope (SEM) images of hydraulically fractured Tennessee sandstone created by using 50 cP fracturing fluid flowing at 10 cc/min under triaxial conditions is shown in **Figure 54**. SEM images support our schematic of fracture surface shown in **Figure 53**. Stress conditions for the test are shown in **Table 4**. Damani et al., (2012) describes the hydraulic fracture experiment for Tennessee sandstone. **Figure 55** shows the hydraulically fractured Tennessee sandstone with borehole indicated.

Fracture width (see **Figure 55**) was measured using SEM images after stresses were released. Note that the fracture width varies as function of distance away from the injection borehole. Fracture width varies from 46.6 μm to 3.3 μm causing differential proppant placement. There is a possibility of that the two mating surfaces (see **Figure 53**) are rough leading to changes in fracture width locally which can cause placement of a monolayer of proppant. Note it is possible that asperities act as barrier to proppant flow. Variation in local proppant concentration can lead to preferential deformation under stress. We carried out a study to investigate the effect of fracture morphology i.e. differential or variable proppant concentration on proppant crushing.

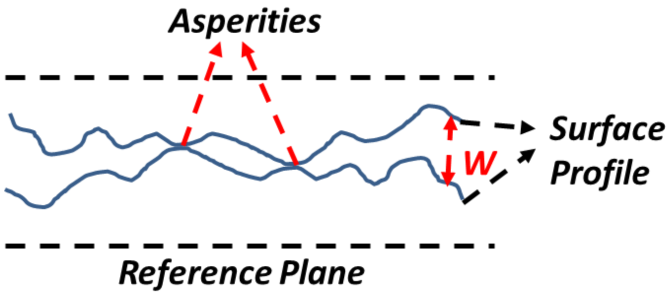

Figure 53: Schematic of a hydraulic fracture with mating surface showing exaggerated roughness (adapted from Kassis and Sondergeld, 2010). Width varies along the fracture causing proppant concentration variation.

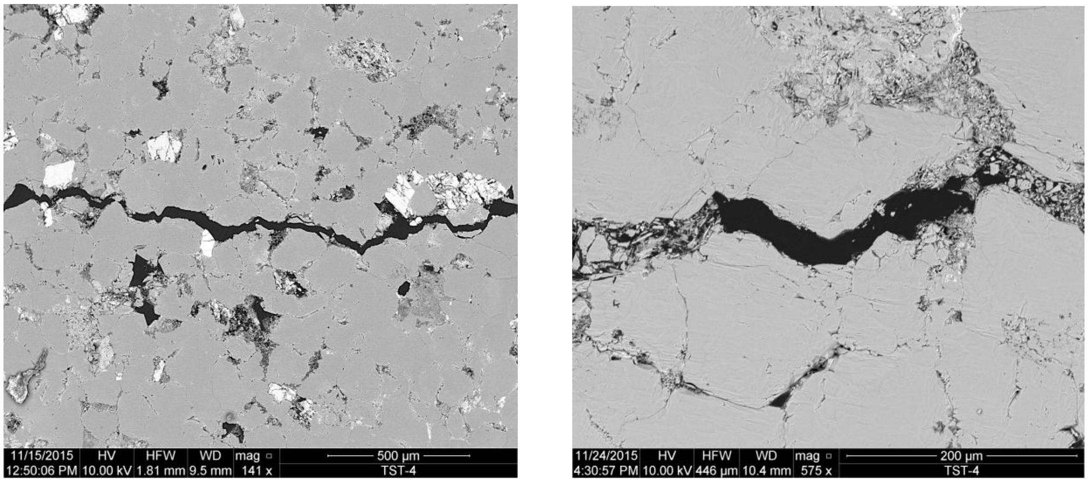

Figure 54: SEM image of hydraulically fractured Tennessee sandstone Left: 32 mm away from the injection borehole. Fracture with is fairly uniform. Right: 25 mm away from center of injection. Fractured quartz grains obstructing the flow path of proppant (Damani, 2015).

Table 4: Stress state for triaxial hydraulic fracturing test performed on Tennessee sandstone. Stresses are color coded to compare with arrows showing orientation of stresses in figure 54 (Damani, 2015).

Stress State	
σ_V	3000 psi
σ_H	2000 psi
σ_h	500 psi

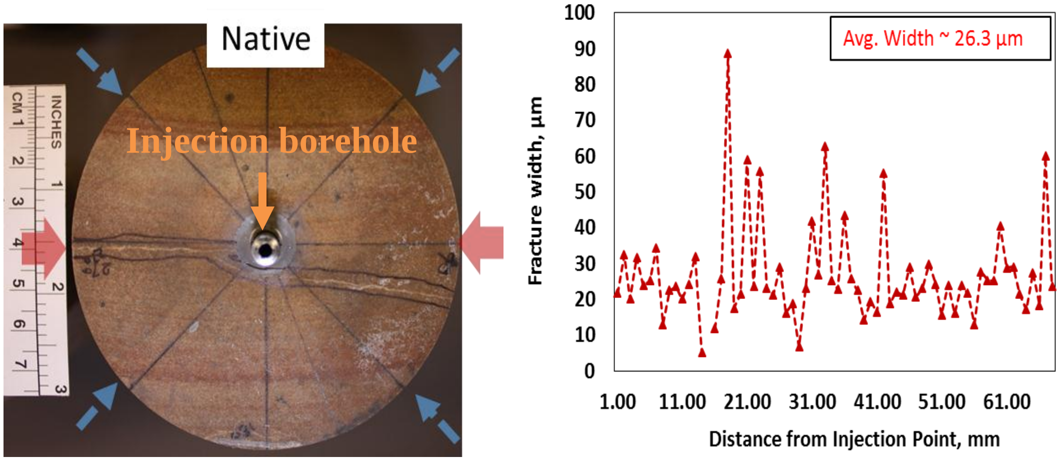

Figure 55: Left: Dry Tennessee sandstone with arrows indicating stress orientation and injection borehole (thicker arrows = σ_H, smaller arrows at 45^o indicate a fluid pressure = σ_h). Hydraulic fracture is visible. Right: Fracture width as function of distance away from injection borehole. Fracture width varies from 46.5 µm to 3.3 µm (Damani, 2015).

3.9.2 Crush cell modification

The piston of the crush cell was modified from a flat-surface face to a face with curvature (see **Figure 56**). Both faces were made from stainless steel to keep boundary conditions - mechanical interaction between proppant grains and face were the same. It was designed such that thickness in the middle of the curved piston is 4 times the mean diameter of the 20/40 mesh Ottawa sand (≈700 µm). It can be thought of as 4 proppant grains less in the middle than on the sides of the curved piston (assuming cubic packing).

3.9.3 Results

20/40 mesh Ottawa sand was tested at two different concentrations - [1] and [4] with constant displacement rate, to study the effect of fracture morphology on σ_{crit} (see test matrix in **Table 5**). Loading rate and AE rate were studied as function of time and are shown in **Figure 57** for concentration of [1] and [4]. The loading rate and AE rate with time show similar characteristics to those observed in previous tests carried out using a flat-surface pistons (see **Sections 3.5** and **3.6**). The decrease in loading rate after reaching peak loading rate in **Figure 57** can be interpreted as the proppant pack undergoing grain crushing and subsequent compaction (see **Section 3.5.1**).

Table 5: Test matrix for the crush test showing the proppant type and Δ used for 3 different concentrations of 20/40 mesh Ottawa sand: [1] and [4].

Proppant type →	**20/40 mesh Ottawa sand**		
Displacement rate ↓	**[1]**	**[2]**	**[4]**
$\Delta_{3.8}$	✓		✓

Crush test results conducted using curved face pistons are compared to those conducted using flat-surface face pistons: loading rate as function of load and particle size analysis as function of pressure are shown in **Figures 58** and **59** for [1] and [4], respectively. For

[1], the response to loading rate after reaching peak loading rate is different for test conducted using curved face and flat-surface face (see **Figure 58(a)**). Note the loading rate decrease for curved piston is steeper compared to flat-surface piston. This indicates that proppant undergoes crushing relatively easily for the curved piston and particle size analyses confirms this (in terms of particle size; see **Figure 58(b)**). Particle size distributions at 5000 psi indicates that smaller size fines are generated for curved piston compared to flat-surface piston (see **Figure 58(c)**). But, particle size distributions are nearly similar at 9000 psi (in terms of particle size but not quantity; see **Figure 58(d)**); it indicates that proppant crushing is independent of fracture geometry beyond certain pressure. For [4], response of loading rate after reaching peak loading rate is similar for test conducted using either curved piston or flat-surface piston (see **Figure 59(a)**). This indicates that proppants undergo similar crushing and particle size analyses confirms this (in terms of particle size; see **Figure 59(b)** and **(c)**). Fracture face morphology effects are observed (in terms of particle size) at lower proppant concentration i.e. [1] compared to no effects observed at higher concentration i.e. [4].

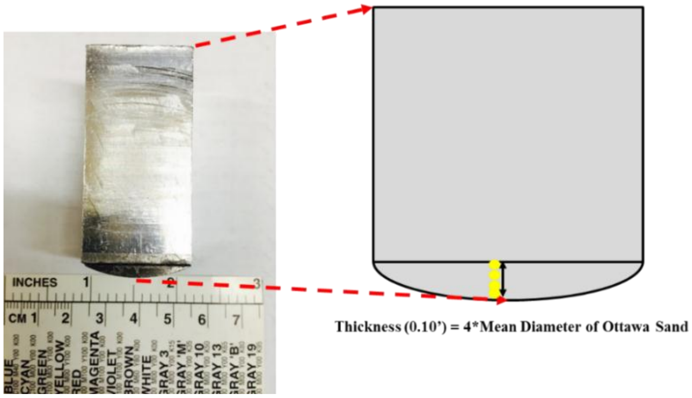

Figure 56: Modified crush cell piston to test proppant crushing when proppant concentration is variable. Thickness in middle is 4 times the mean diameter of 20/40 mesh Ottawa sand (≈700 µm).

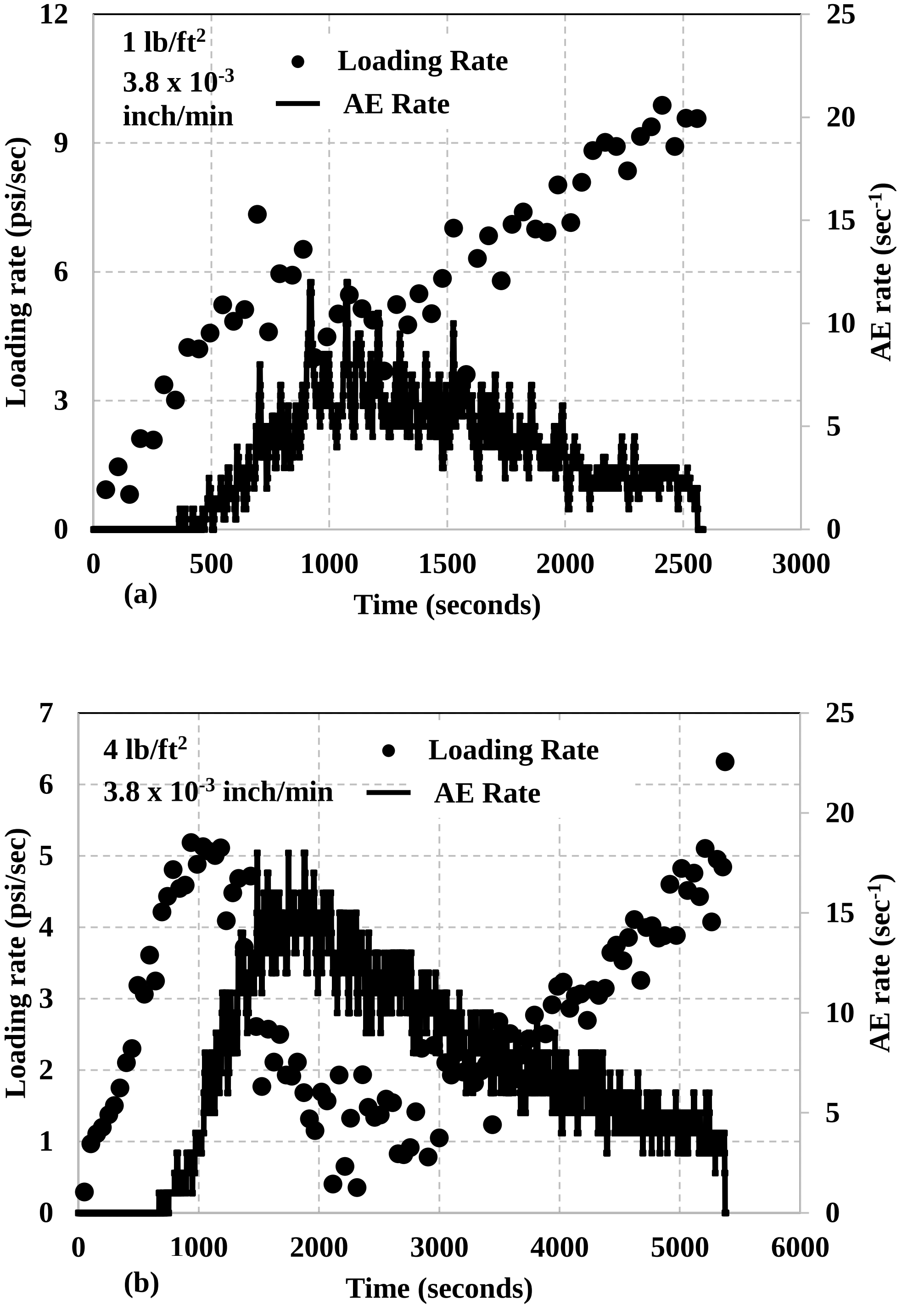

Figure 57: Loading rate (circle) and AE rate (line) as function of time for concentration of: (a) 1 lb/ft^2 and (b) 4 lb/ft^2. Duration of the test is longer with increase in proppant concentration.

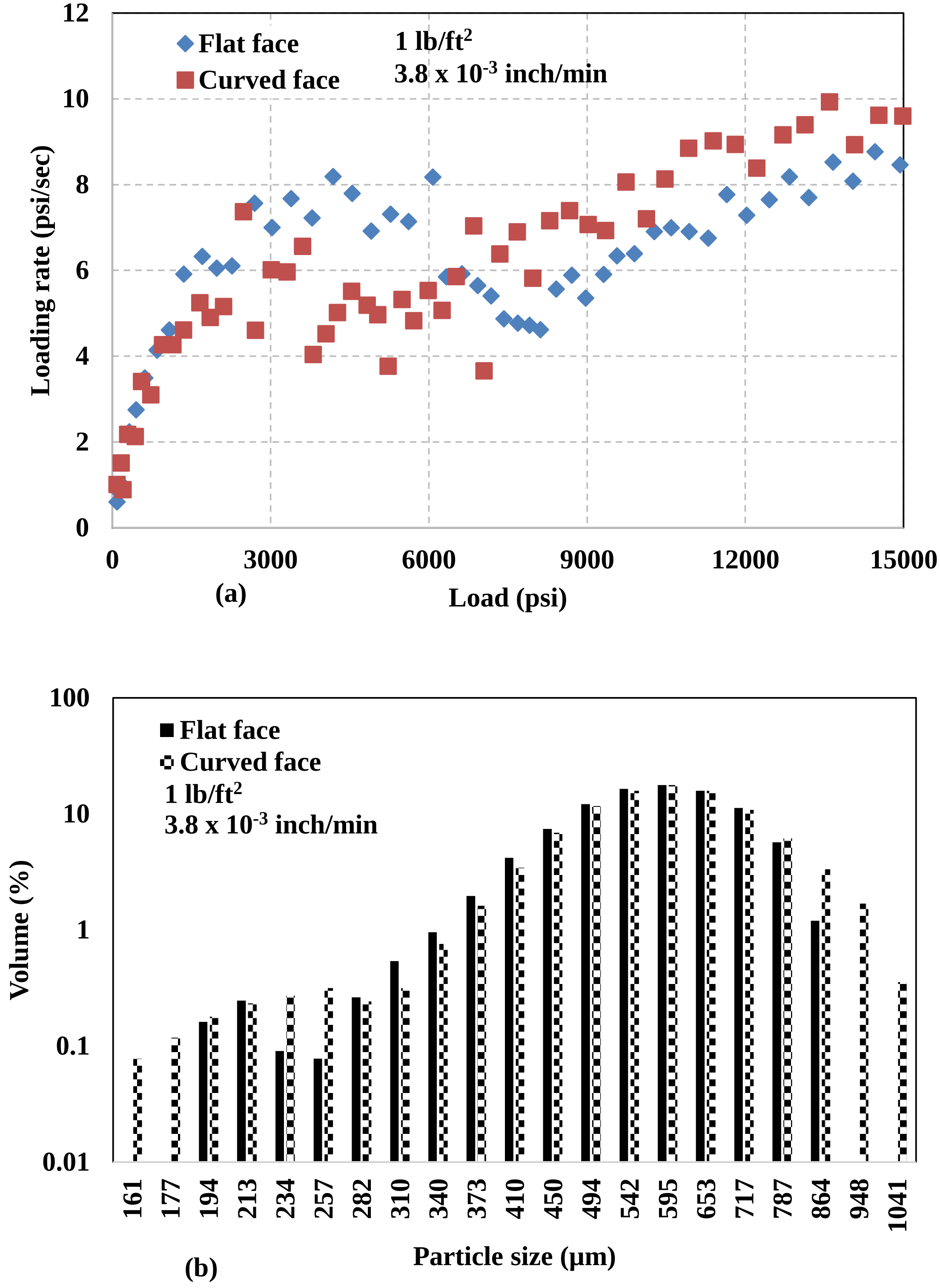

(Caption on page 76)

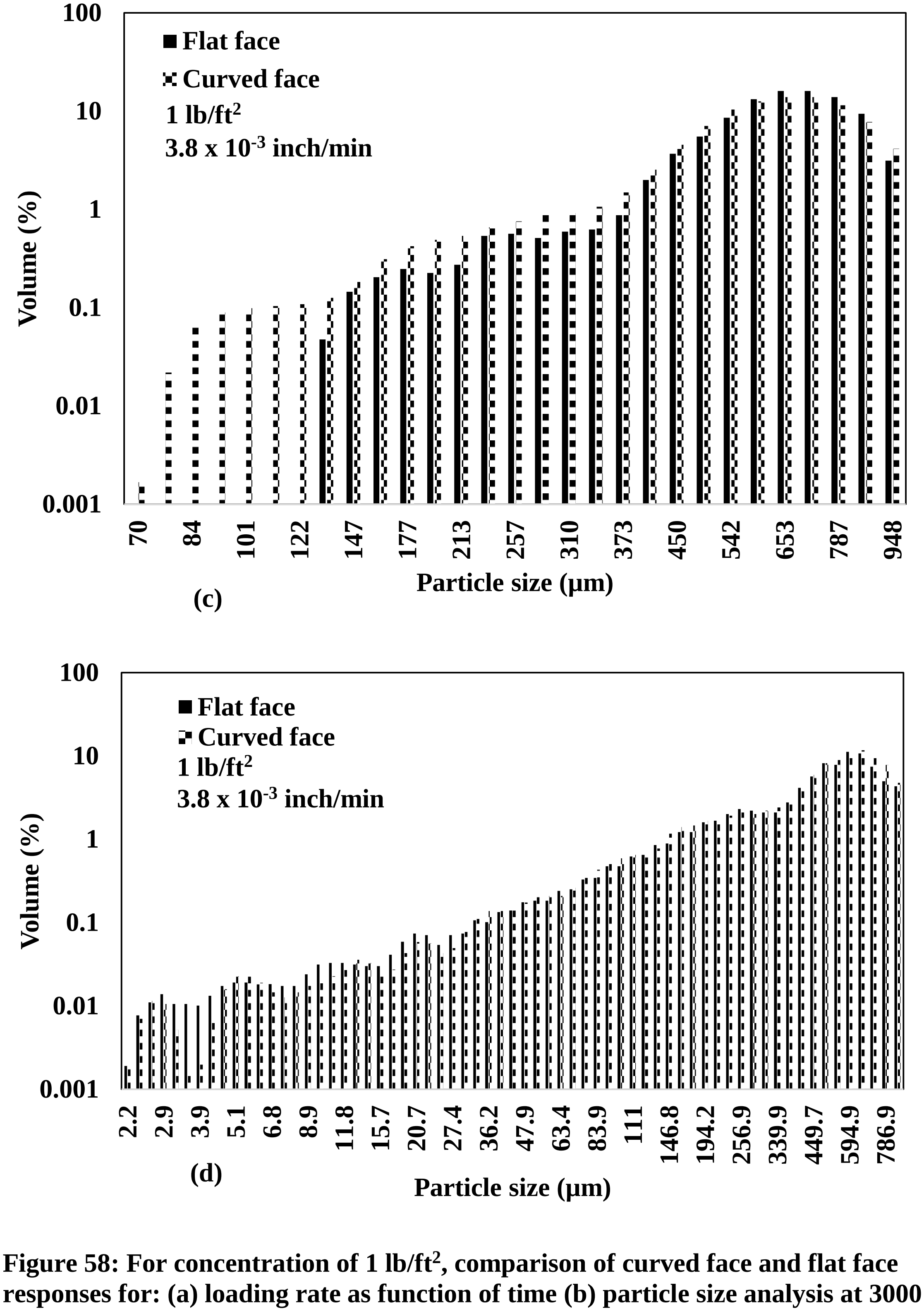

Figure 58: For concentration of 1 lb/ft^2, comparison of curved face and flat face responses for: (a) loading rate as function of time (b) particle size analysis at 3000 psi (c) particle size analysis at 5000 psi (d) particle size analysis at 9000 psi.

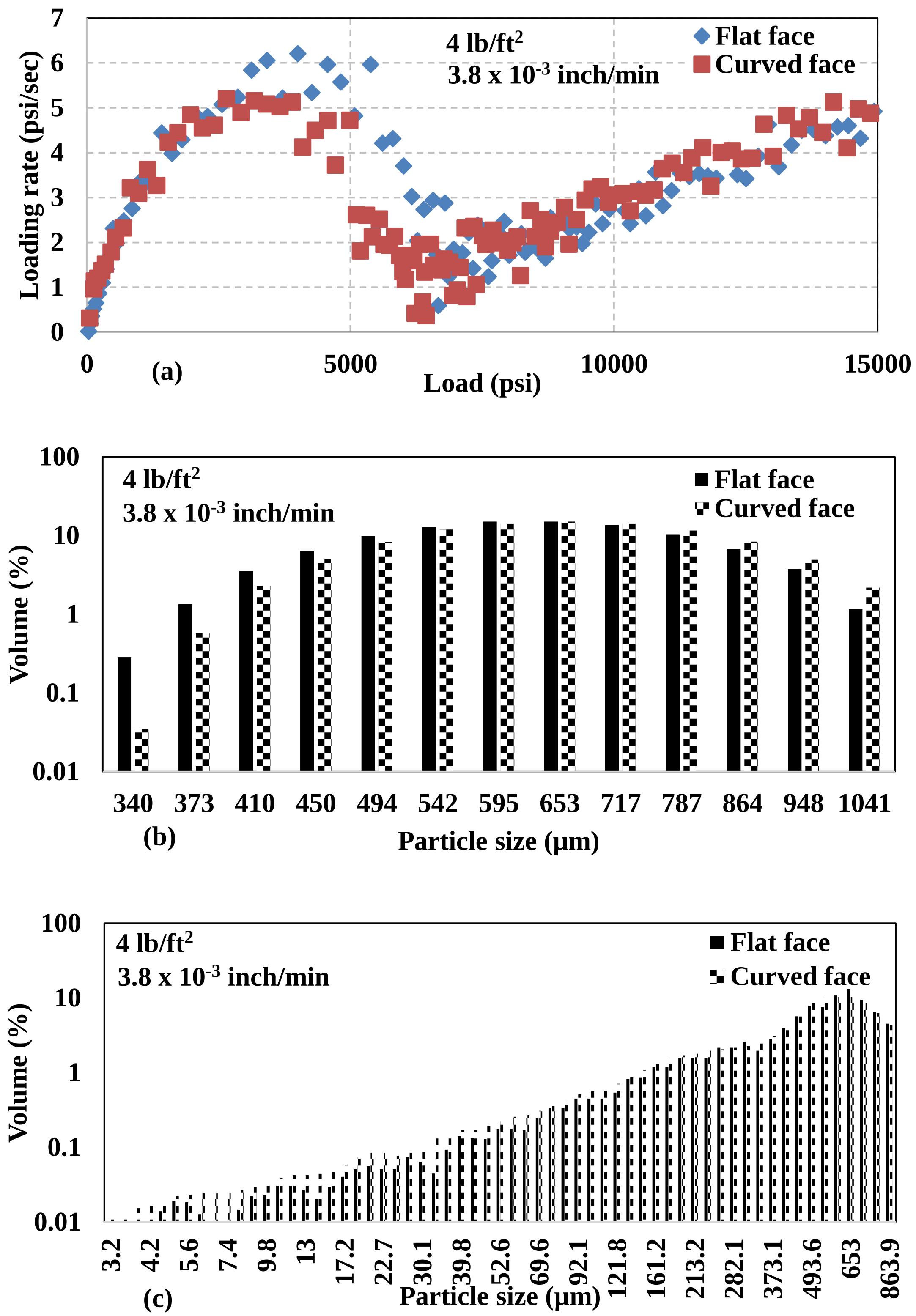

Figure 59: For concentration of 4 lb/ft^2, comparison of curved face and flat face responses for: (a) loading rate as function of time, (b) particle size analysis at 5000 psi and (c) particle size analysis at 9000 psi.

Microscope images of tests on [1] and [4] proppant pack using curved piston were captured as function of pressure and are shown in **Figure 60**. The [1] proppant pack shown in **Figure 60** starts to crush at 3000 psi. At 7000 psi, proppant crushes non-uniformly and crushing is concentrated at the steel-proppant interface in the region (middle) where stresses are the greatest and proppant concentration is the lowest. This microscopic crushing behavior is different from that observed using flat-surface piston. For [4], proppant starts to crush at 7000 psi; proppant pack crushes non-uniformly and crushing is concentrated at steel-proppant interface and in the region (middle) where stresses are the greatest and proppant concentration is the lowest. Note that particle size analyses agree with visual observations.

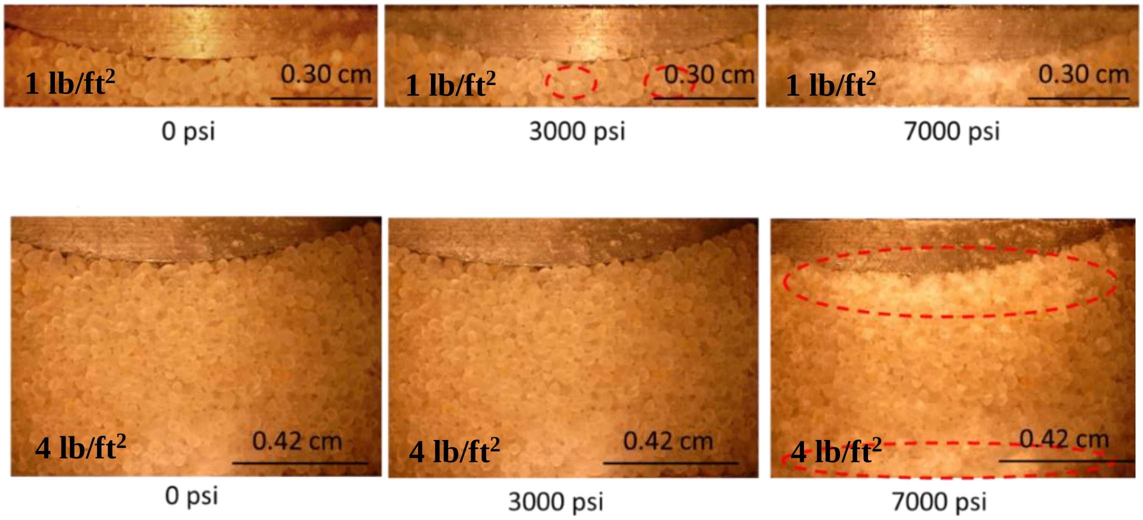

Figure 60: Microscope images as function of pressure for a curved piston: Top – 1 lb/ft^2 and Bottom – 4 lb/ft^2. Crushing for both concentration of 1 and 4 lb/ft^2 is non-uniform and concentrated at steel-proppant interface and in the region where proppant concentration is the lowest and stresses are the greatest.

3.10 Summary

Observations from study of effects of concentration, displacement rate, proppant type, cyclic loading and fracture morphology are summarized below:

	Effects of	**Observations from**	
		Load/AE data	**Microscope images/ Particle size analysis**
1)	**Concentration**	Loading rate as function of load is indicator of σ_{crit} and compaction	• Images: uniform for [1], non-uniform for [4] and at steel-proppant interface • Particle size analysis supports interpretation from load data
2)	**Displacement rate**		
3)	**Proppant type**	σ_{crit} determined using loading rate methodology	Particle size analysis supports interpretation from load data
4)	**Cyclic loading**	AE related to proppant crushing	Particle size analysis supports interpretation from load data
5)	**Fracture morphology (curved piston)**	Smaller sized fines for [1], similar crushing for [4] when compared to flat-surface face	• Images: crushing concentrated in region where stresses are the greatest and proppant concentration is the lowest • Particle size analysis supports inferences from load data

Chapter 4: Wet Proppant Crush Test

4.1 Introduction

Motivation for the study is defined in the next section, **Section 4.2**. This chapter describes the test conducted with distilled water present in the pore space (referred to as saturated proppant pack tests, see **Section 4.3**) and another test conducted on proppant which was exposed to distilled water at 100 ^{o}C for 3 days prior to testing (referred to as heat water treated proppant pack tests, see page 92 “treated proppant” in **Section 4.3**).

4.2 Motivation

The motivation of the study was to investigate proppant performance under more realistic field conditions. The saturated proppant pack tests were conducted to compare compaction trends, and particle size analyses between tests conducted on dry and wet proppant packs. The heat and water treated proppant pack tests provide insight into the extent of the silica water wakening effect on σ_{crit}. Note that silica present in quartz-rich proppant undergoes dissolution especially at high pH. Previous researchers (Lawn, 1993; Irwin, 1958 and Wong et al., 2004) have modeled the chemical effect of water on mechanics of fracture. Wong et al., (2004) found that chemical effect reduces the fracture toughness and thereby, lowers the σ_{crit} for grain crushing.

Laboratory studies of proppant conductivity indicate that silica-rich proppant undergoes dissolution when exposed to distilled water for extended periods of time (Ghosh et al., 2013). Ghosh et al., (2013) conducted tests using brine at high temperature - 225^{o}F on 20/40 mesh Ottawa sand placed between samples of Barnett shale. Petrophysical and mechanical properties of Barnett shale are shown in **Figure 61**. Silicon ion concentration was determined as function of time using Inductively Coupled Plasma (ICP) technology on the outlet brine. **Table 6** shows the test conditions used in the study by Ghosh et al., (2013). Silicon concentration as function of time for tests 1 and 2 in **Table 6** are shown in **Figure 62**.

Figure 61 shows that the quartz content in the Barnett shale sample varied from 2% (by wt.) to as much as 33% (by wt.), possibly contributing to the variation in silicon ion concentration in the outlet brine (see **Figure 62**). Another possible source for silicon ion is the leaching of silica from quartz-rich 20/40 mesh Ottawa sand. Interestingly, the test conducted with shale 1 (lower quartz content) shows higher silicon ion concentration in the outlet brine compared to shale 2.

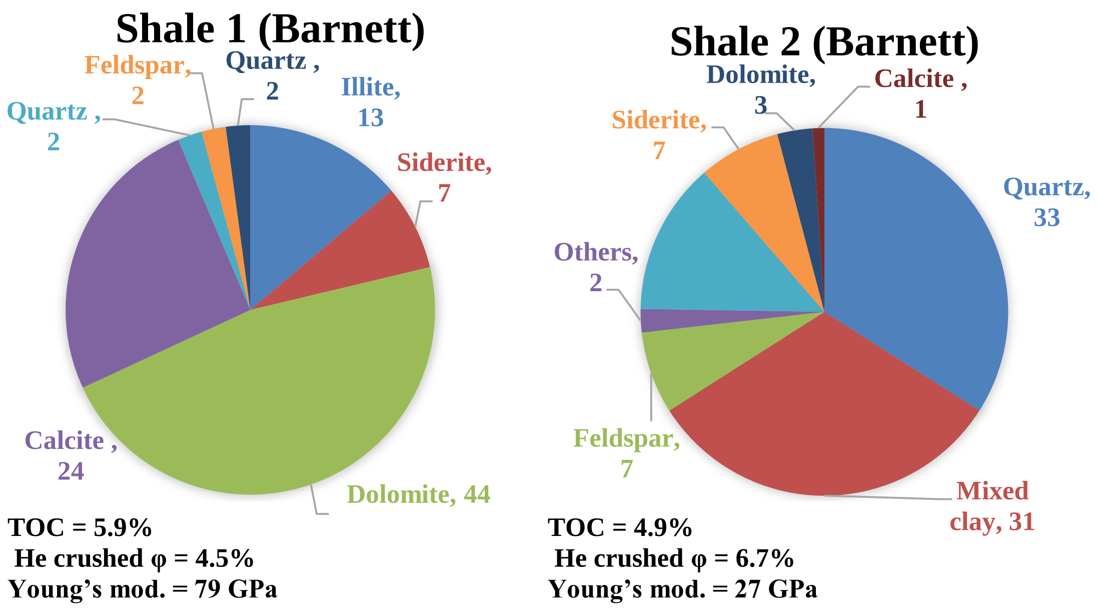

Figure 61: Petrophysical and mechanical properties of Barnett shale used to study long-term proppant pack conductivity. Shale 1 is carbonate-rich and shale 2 is clay-rich. Shale 2 has relatively higher porosity and lower Total Organic Carbon (TOC) (Ghosh et al., 2013).

Table 6: Test conditions used by Ghosh et al. (2013) to track silicon ion concentration as function of time. St.* - refers to stainless steel.

Test	Duration (days)	Temp. (°F)	Proppant type	Shale	Sieve	End Plugs	Brine	Flow rate (ml/min)
1	30	225	20/40 Ottawa	1	St.	St.*	2% KCl	0.12
2	60	225	20/40 Ottawa	2	St.	St.*	2% KCl	0.12

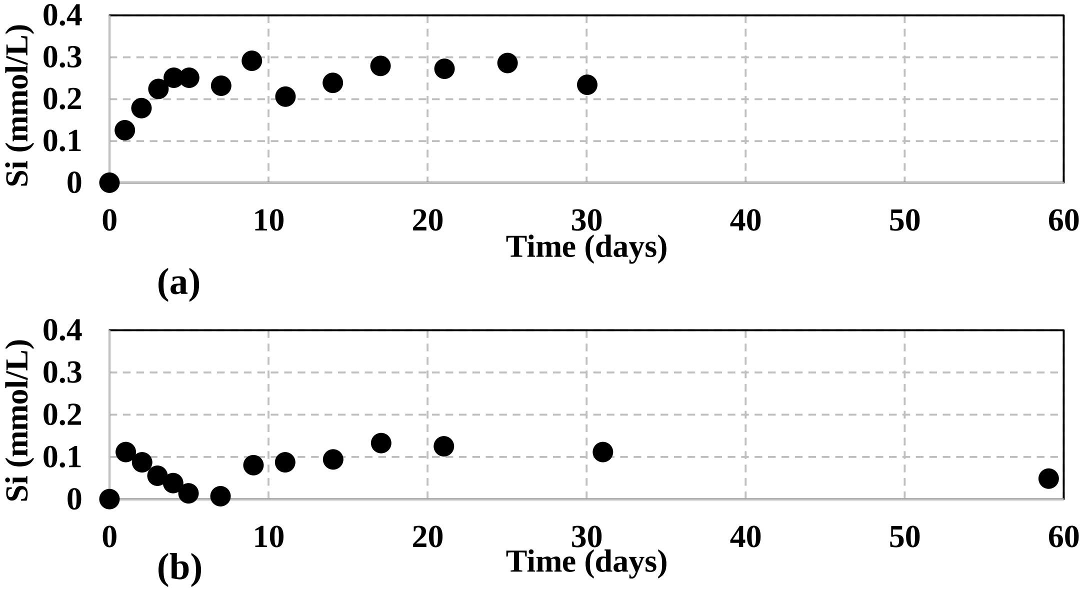

Figure 62: Silicon ion concentration as function of time for (a) Test 1 (b) Test 2. Concentration stabilizes for the tests in the long run (Ghosh et al., 2013).

Weaver et al., (2009) has indicated that dissolution of silica from proppant can occur rapidly over a fraction of a year under reservoir conditions. Silica dissolution can lead to rapid degradation of proppant pack porosity through pressure solution and compaction. **Figure 63** (Weaver et al., 2009) illustrates the pressure solution and compaction mechanism. Mineral dissolution leading to proppant grain diameter reduction along the load-bearing axis and thereby, compacting the proppant pack. Stress causes silica-saturated water to diffuse into pore space (Weaver et al., 2009). The solution in the pore space becomes supersaturated subsequently precipitating which leads to reduction in porosity. Lee et al. (2009) studied reduction in porosity as function of temperature and time using a specific stress level and particle size in a pressure solution and compaction model. As evident from the results shown in **Figure 64**, porosity degrades faster at higher temperature because it is an Arrhenius process descibed:

$$k = \frac{-E_O \sigma}{RT} + lnA \quad \ldots\ldots\ldots\ldots\ldots\ldots\ldots\ldots\ldots\ldots\ldots\ldots\ldots\ldots\ldots\ldots\ldots\ldots\ldots\ldots\ldots\ldots\ldots\ldots \text{(3)}$$

Where:

k: rate constant,

E_O: activation energy,

R: gas constant,

T: temperature,

A: Arrhenius constant.

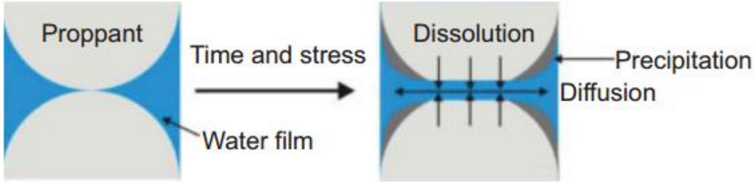

Figure 63: Illustration of pressure solution and compaction mechanism. High stresses at grain-grain contact leads to dissolution of silica and then precipitation in pore space leading to reduction in porosity (Weaver et al., 2009).

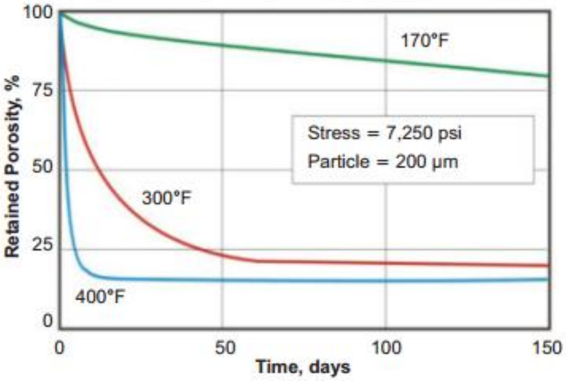

Figure 64: Pressure solution and compaction model simulation to obtain porosity loss in quartz pack as a function of time (Lee et al., 2009).

4.3 Effect of saturation

4.3.1 Crush cell modification

The windowed crush cell was modified to eliminate fluid leakage. Teflon seals were designed and machined for upper piston and fused silica window subsequently sealant was applied to prevent fluid leakage. A 1/8 inch hole was drilled on a side of the crush cell and a metering pump was attached to maintain pore pressure at 50 psi. **Figure 65** shows the modified crush cell. **Figure 66** shows schematically how the modified crush cell was assembled; bottom face was inserted followed by installing the top piston equipped with a teflon seal. Proppant was poured into the crush cell from the side. Fused silica window with teflon seal was clamped to the outside of the crush cell. Pressure was increased to 2000 psi before applying pore pressure of 50 psi and the reasons for this will be discussed in experimental procedure section.

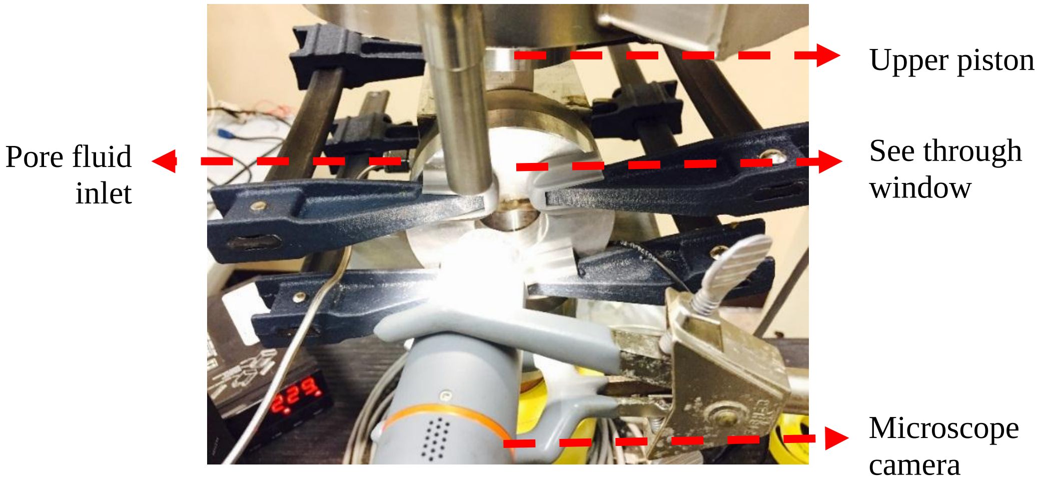

Figure 65: Modified crush cell in use. Pore fluid inlet, microscope camera, upper piston and window are shown.

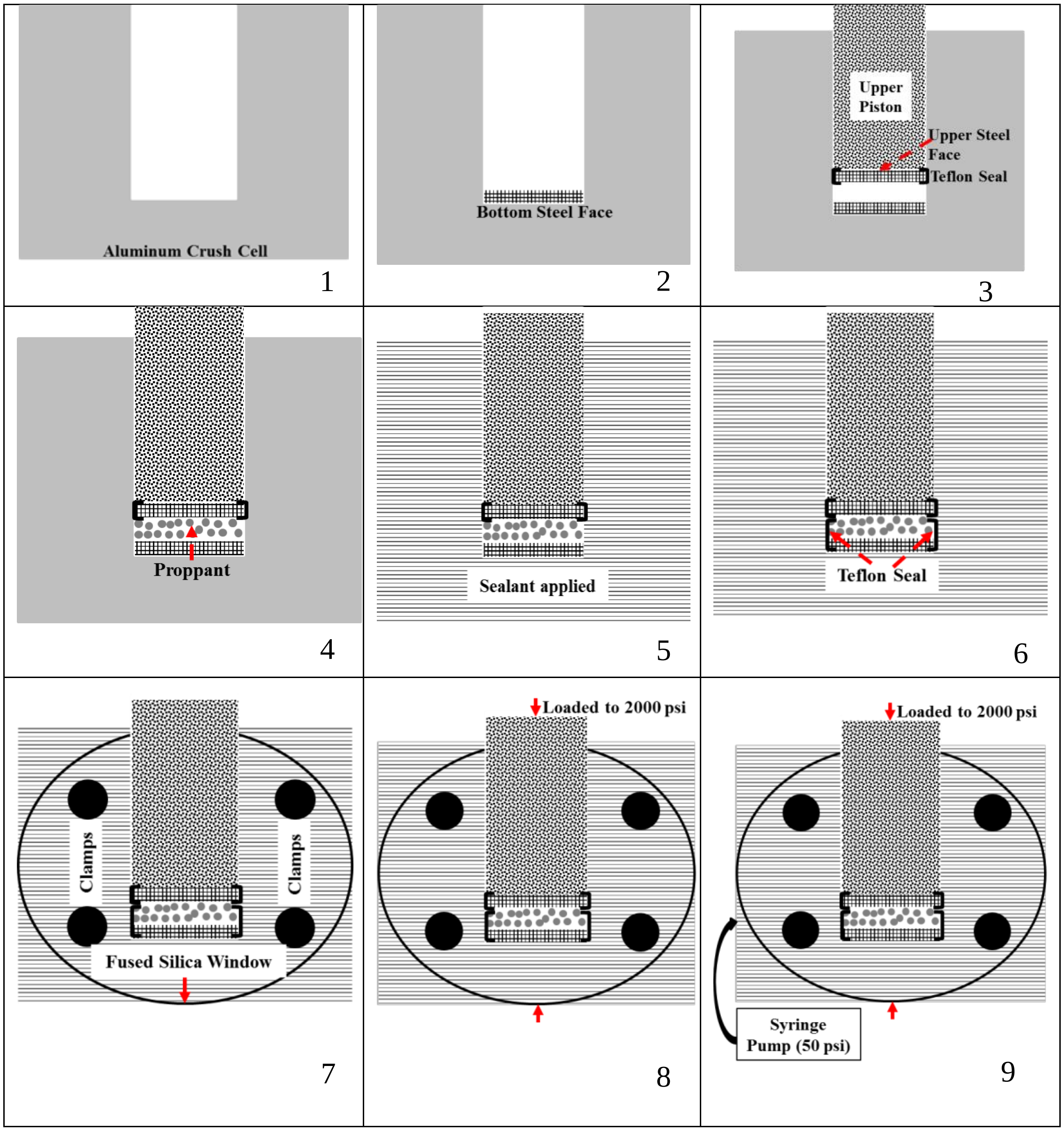

Figure 66: Steps for assembling the modified crush cell. Teflon seal and sealant was used to minimize fluid leakage. 1: Schematic cross-section of crush cell. 2: Bottom steel face is inserted. 3: Upper piston and face with teflon seal is inserted 4: Proppant is poured from the side. 5: Sealant is applied. 6 and 7: Fused silica window is clamped to outside of crush cell. 8: Axial pressure is increased to 2000 psi. 9: Pore pressure is increased to 50 psi using distilled water.

4.3.2 Test matrix

Only one test was conducted at [4] of 20/40 mesh Ottawa sand at $\Delta_{3.8}$ with distilled water. Further tests need to be done to systematically study the effect of pore fluid and pH on crushing and compaction.

4.3.3 Experimental procedure

Similar to dry proppant pack crush tests, proppant pack was sieved to specific sieve sizes and then poured in to modified crush cell from the side as shown in **Figure 66**. The dry tests showed that 20/40 mesh Ottawa sand at [4] and $\Delta_{3.8}$ does not start to crush till 2000 psi. This allowed us to increase the axial pressure to 2000 psi to seal the cell from top to reduce leaks when pore pressure is increased to 50 psi. Note that proppant does undergo compaction solely due to grain rearrangement. Particle size distribution of native proppant and post-test proppant at 3000 psi is shown in **Figure 67**.

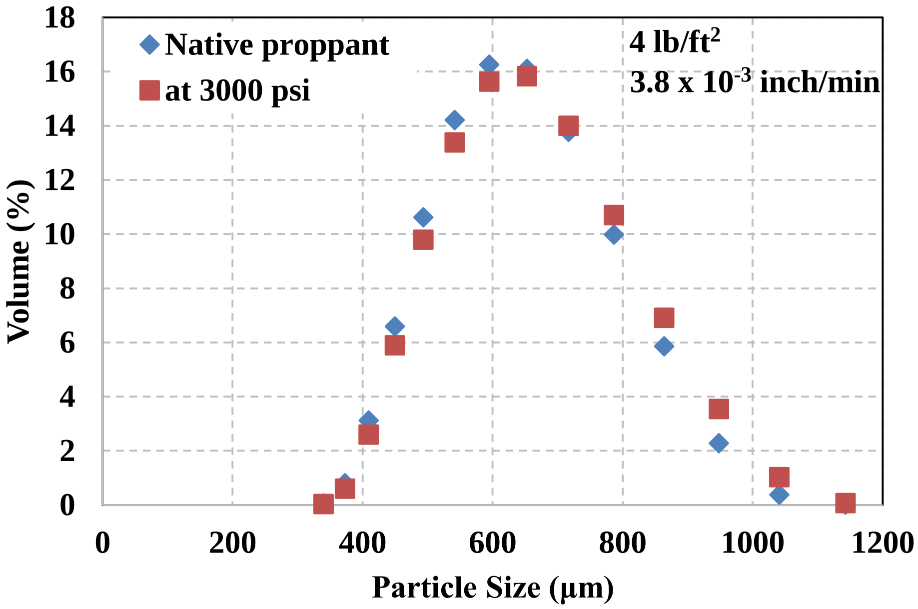

Figure 67: Particle size distribution for unstressed proppant and dry proppant at concentration of 4 lb/ft^2 of 20/40 mesh Ottawa sand with the $\Delta_{3.8}$ at 3000 psi. No significant difference in particle size distribution.

Axial pressure is maintained at 2000 psi and pore fluid, distilled water, enters through the inlet to increase the pore pressure to 50 psi. Minimal pore pressure was applied as it was difficult to seal an assembled windowed crush cell to higher pore pressures. Pore pressure was gradually increased in increments of 10 psi. Microscope images of proppant pack saturated with distilled water were captured as function of pore pressure (see **Figure 68**) and these confirmed the uniform distribution of water in pores. The proppant pack was loaded to 11000 psi at $\Delta_{3.8}$ while maintaining pore pressure at 50 psi. It was difficult to prevent a leak above 11000 psi and therefore, axial pressure was limited to 11000 psi. Post-test proppants are dried in an oven at 100 ^{o}C for 4-5 hours before determining particle size distribution of dry proppant.

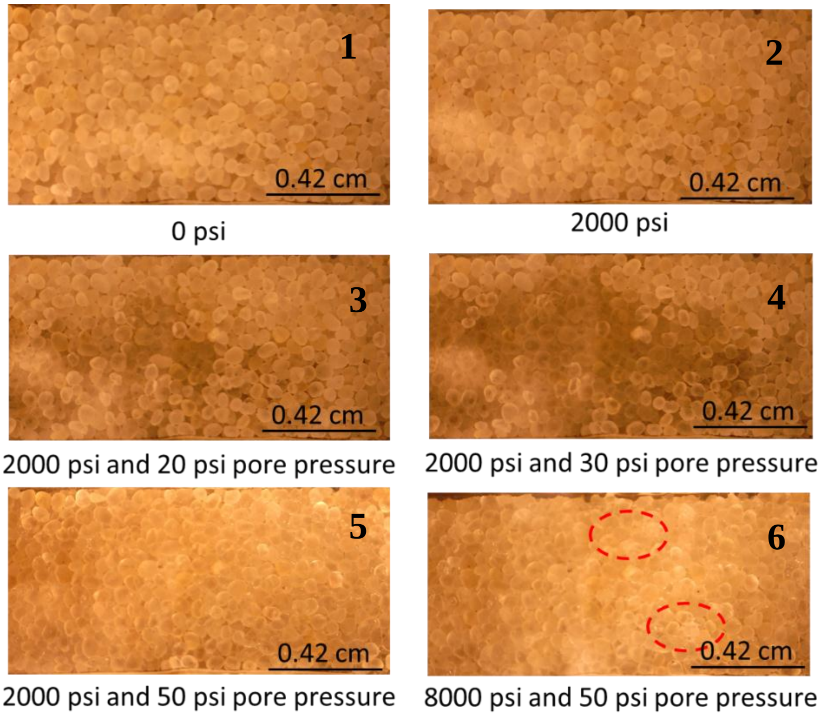

0 psi

2000 psi

2000 psi and 20 psi pore pressure

2000 psi and 30 psi pore pressure

2000 psi and 50 psi pore pressure

8000 psi and 50 psi pore pressure

4 lb/ft^2 3.8 x 10^{-3} inch/min

Figure 68: Microscope images as function axial load and pore pressure. 1 and 2 are captured as function of axial load increase. The proppant pack underwent compaction with increase in axial load. 3, 4 and 5 are captured as function of increase in pore pressure. 6 confirms uniform distribution of pore fluid at 50 psi. Minimal crushing, marked by red circles, is observed at 8000 psi.

4.3.4 Results

Pressure and AE rate were monitored for saturated proppant pack test (see **Figure 69**) which were compared to tests conducted on dry proppant pack at a similar concentration and displacement rate. There is minimal AE activity when the load is increased to and maintained at 2000 psi which is indicative of the absence of crushing. The axial pressure is maintained at 2000 psi till pore pressure is increased to 50 psi. Axial pressure is increased at a constant $\Delta_{3.8}$ to 11000 psi. Note that AE are relatively few over the entire duration of the test compared to test conducted on dry proppant.

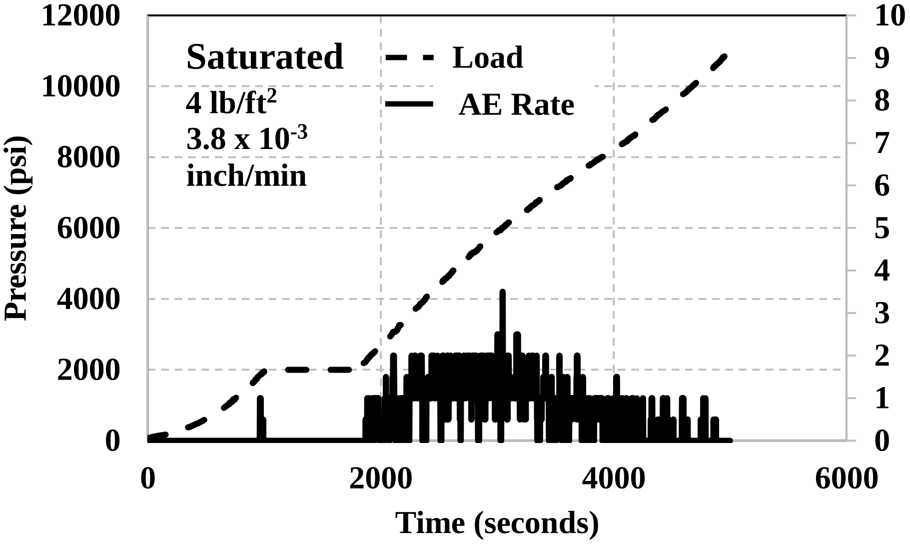

Figure 69: Pressure (dash) and AE rate (solid) as function of time. Pore pressure was increased to 50 psi when the axial load was maintained stable at 2000 psi. AE rate is found to be minimal compared to dry proppant experiments.

Loading rate is plotted as function of load for dry and saturated proppant pack tests in **Figure 70**. The loading rate for dry proppant tests shows a characteristic response, i.e., loading rate increases to a peak, then decrease to reach a minimum and finally increases at a lower rate than initial increase. But we do not observe significant variation in loading rate for saturated proppant pack tests; there is a gradual decrease and then a gradual increase with increase in load. Further research is needed to ascertain the behavior of loading rate with load and time.

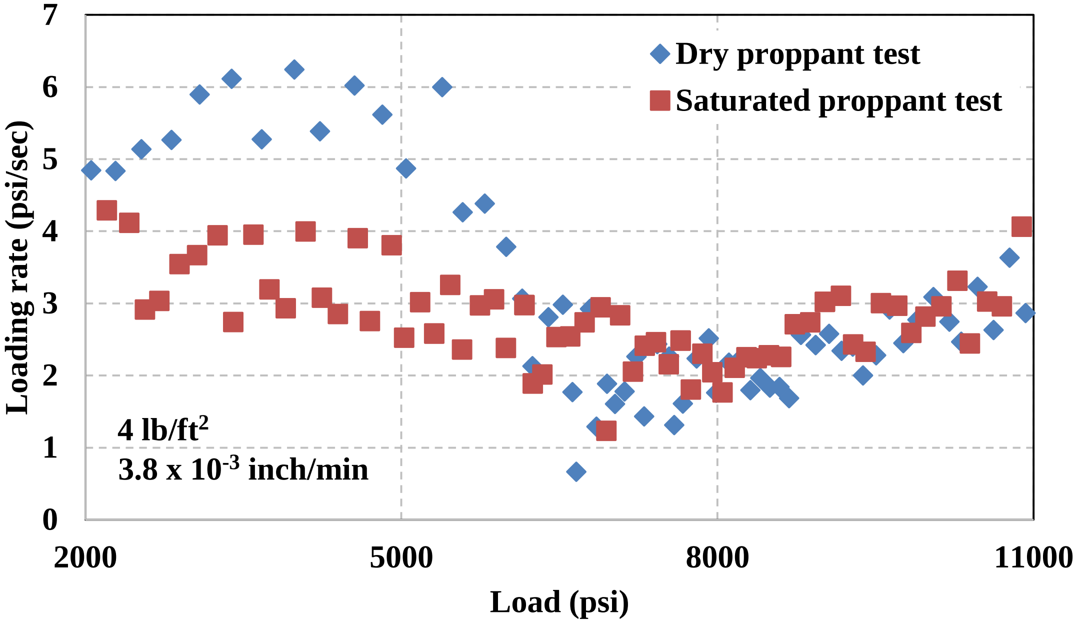

Figure 70: Loading rate as function of load for tests conducted dry and saturated at concentration of 4 lb/ft^2. For test conducted saturated, loading rate does not show significant variation as function of load.

Microscope images were captured as function of axial pressure. Images at 0, 2000 and 8000 psi axial pressure are shown in **Figure 68**. Minimal proppant crushing is observed. Compaction is calculated through height measured from images and is plotted as function of pressure for dry and saturated proppant tests in **Figure 71**. The compaction trend for the saturated proppant test is different from that of dry proppant test. Trends for dry and saturated proppant tests match till 2000 psi at which water is introduced to the pack. The introduction of water reduces frictional resistance at grain to grain contacts causing saturated proppant pack to compact significantly between 2000 and 5000 psi. Reduction in friction allows relative grain movement leading to a more dense packing without grain crushing. The saturated proppant pack does not undergo significant additional compaction and note the gradual change in compaction at pressures beyond 5000 psi (see **Figure 71**). For the dry tests, the proppant pack does not undergo significant compaction between 2000 and 5000 psi. We observe that dry pack compacts when proppant starts to crush. Note there is a good correlation between particle size analysis and compaction for dry proppant test (see **Sections 3.4** and **3.5**).

Particle size analysis of post-test proppant at 11000 psi was done after drying proppant in an oven at 100 °C for 4-5 hours. Comparison of particle size analyses for dry and saturated proppant is shown in **Figure 72**. Difference in particle size distribution may be interpreted as an effect of presence of water which promotes grain movement. However, there is no significant difference in volume percentage of particles crushed.

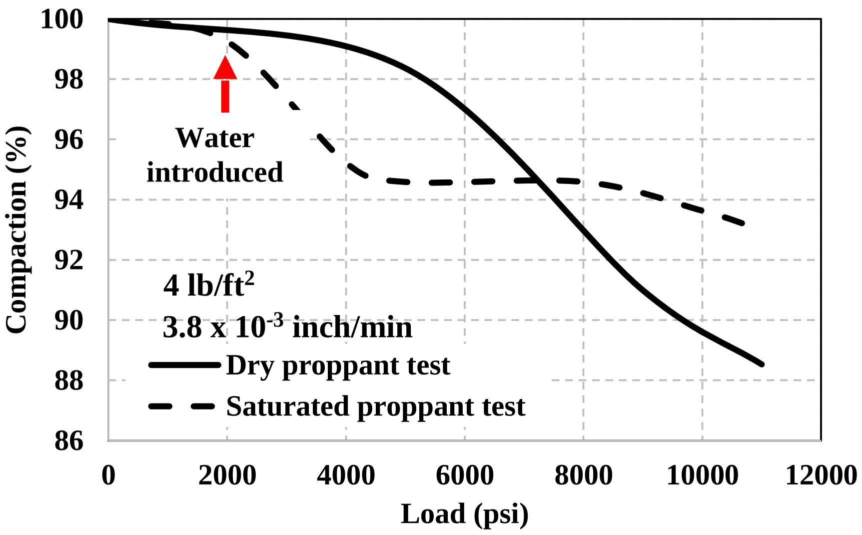

Figure 71: Compaction for dry and saturated tests at concentration of 4 lb/ft^2. Trends are significantly different and may be attributed to reduced friction at grain to grain contacts in saturated test.

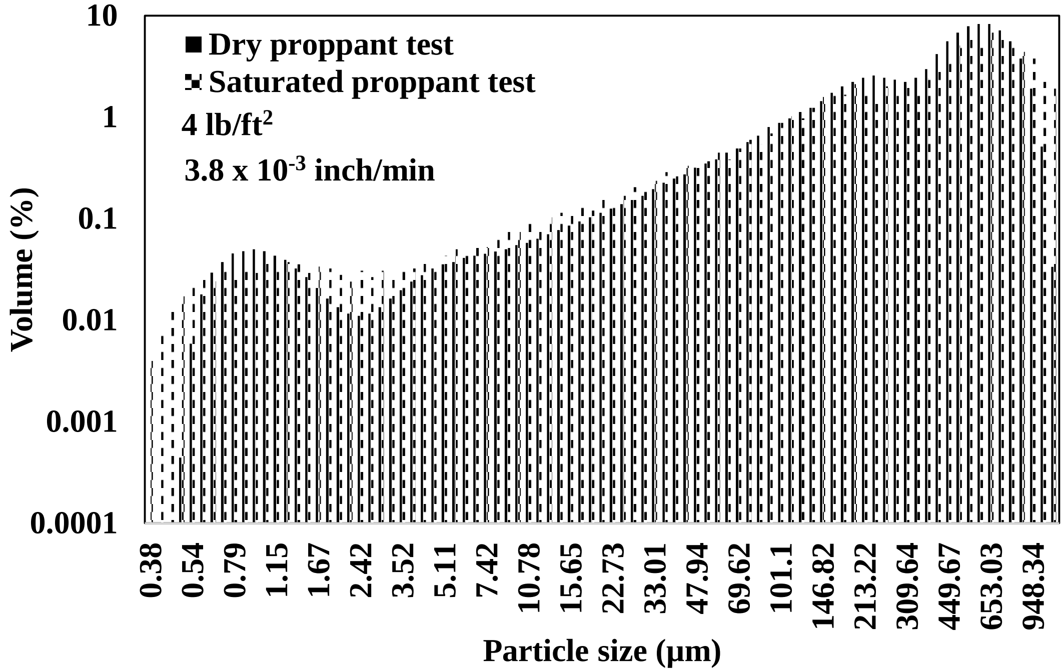

Figure 72: Particle size distribution for dry and saturated test at concentration of 4 lb/ft^2. Very little difference between saturated and dry crush tests particle size.

4.4 Effect of pre-test treatment

4.4.1 Experimental Apparatus

Apparatus used for dry proppant tests was used to study the water treatment effect and is shown in **Figure 18**. **Figure 19** shows how the crush cell was assembled. The procedure used to assemble crush cell for dry tests is different from that for modified crush cell used for saturated tests; the significant difference between the two procedures is how sieved proppant was poured into the cell. Proppant was poured in from side of the crush cell after the top piston was inserted for saturated tests. But, proppant was poured in from the top after the window was clamped for dry tests. Small changes in how proppant was poured into the crush cell can cause significant changes in proppant packing and thereby effect proppant behavior.

4.4.2 Test matrix

20/40 mesh Ottawa sand was tested at two different concentrations – [1] and [4] with constant displacement rate to study the treatment effects on σ_{crit} (see **Table 7**).

Table 7: Test matrix for the crush test showing the proppant type and displacement rate used for 3 different concentrations of 20/40 mesh Ottawa sand: 1 lb/ft^2 and 4 lb/ft^2.

Proppant type → **Displacement rate ↓**	**20/40 mesh Ottawa sand**		
	[1]	**[2]**	**[4]**
$\mathbf{\Delta_{3.8}}$	✓		✓

4.4.3 Experimental procedure

Proppant is sieved and exposed to distilled water at 100 ^{o}C for 3 days in an oven. **Figure 73** shows a container containing 20/40 mesh Ottawa sand in distilled water. Heat and water treated proppant (referred to as "treated proppant") is dried through evaporation. The crush test is performed according to the methodology discussed in **Chapter 2**. Particle size analysis is performed on the post-test proppant.

4.4.4 Results

Loading rate and AE rate for treated proppant was studied as function of time and are shown in **Figure 74** for [1] and [4]. The loading rate and AE rate with time show similar characteristic responses as dry tests; loading rate increases to a peak, then decrease to reach a minimum and finally increases at a lower rate than initial increase (see **Sections 3.4** and **3.5**). The decrease in loading rate after reaching peak loading rate in **Figure 57** can be interpreted as the proppant pack undergoing grain crushing and subsequent compaction.

Treated proppant tests results are compared to dry tests in **Figures 75** and **76** for [1] and [4] respectively. For [1], the response of loading rate after reaching peak loading rate is different for treated and un-treated proppant packs (see **Figure 75(a)**). Note the loading rate decrease for treated test is steeper compared to dry test. This indicates that proppant undergoes crushing relatively easily for treated proppant test and particle size distribution confirms this (see **Figure 75(b)**). Particle size distributions at 5000 psi indicate that smaller fines are generated for treated tests compared to dry tests. But, particle size distributions are nearly similar at 9000 psi (in terms of particle size; see **Figure 75(c)**) suggesting that proppant crushing is independent of treatment effects beyond certain pressure. For [4], response of loading rate after reaching peak loading rate is similar for treated test and dry test (see **Figure 76(a)**). This indicates that proppants undergo similar crushing; the particle size distribution confirms this (see **Figures 76(b)** and **76(c)**). Treatment effects are observed at low proppant concentration i.e. [1] compared to no effects observed at higher concentration i.e. [2].

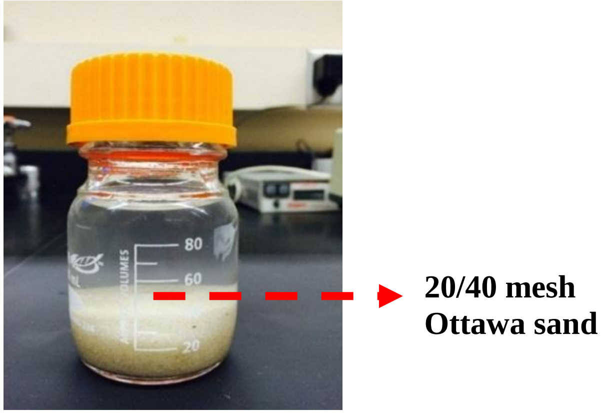

Figure 73: Container filled with 20/40 mesh Ottawa sand and distilled water used to study pre-test treatment effects.

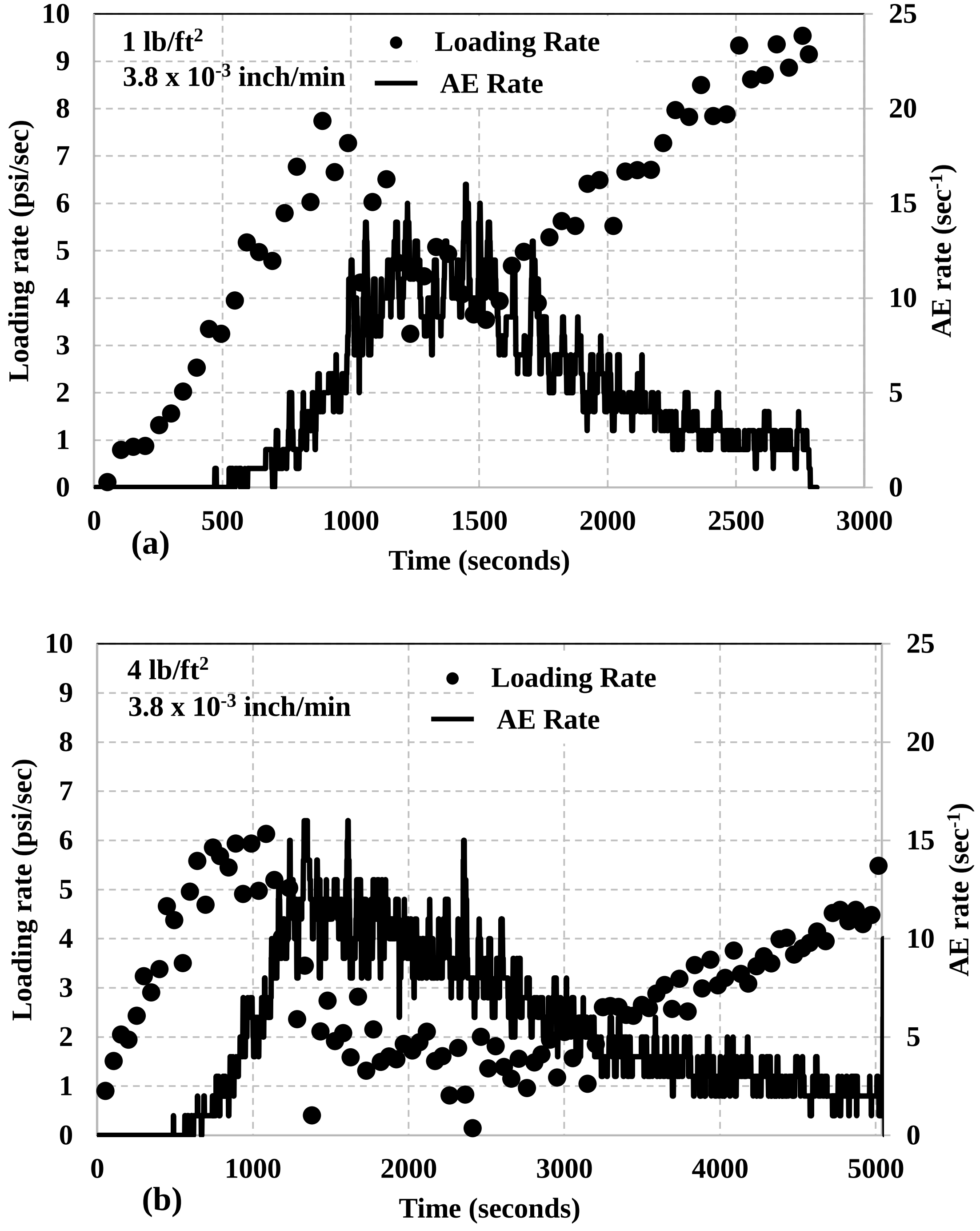

Figure 74: Loading rate (circle) and AE rate (line) as function of time for treated proppant at concentration of (a) 1 lb/ft^2 (b) 4 lb/ft^2.

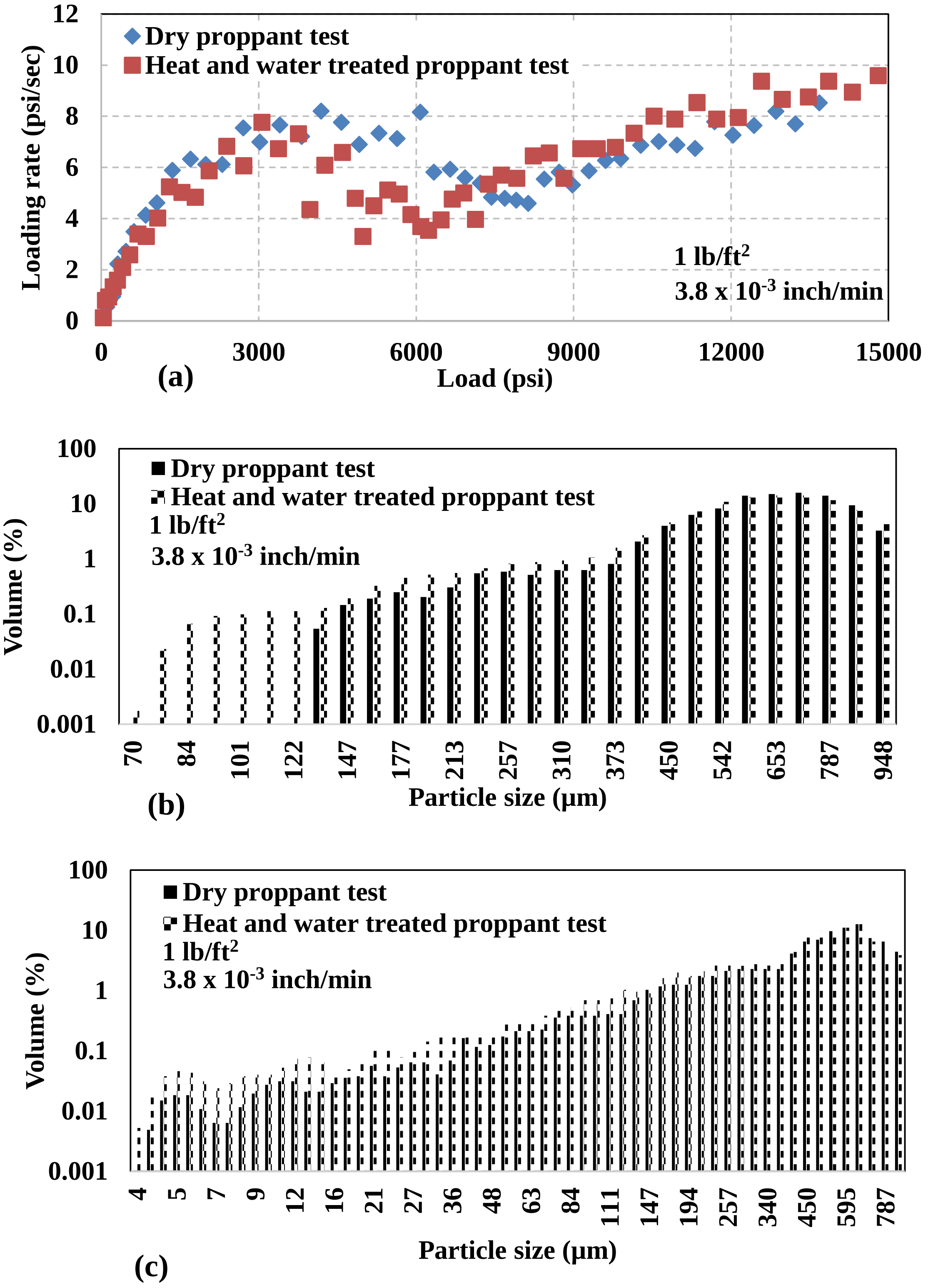

Figure 75: For concentration of 1 lb/ft^2, comparison of treated and dry proppant test responses for: (a) loading rate as function of time (b) particle size analysis at 5000 psi and (c) particle size analysis at 9000 psi.

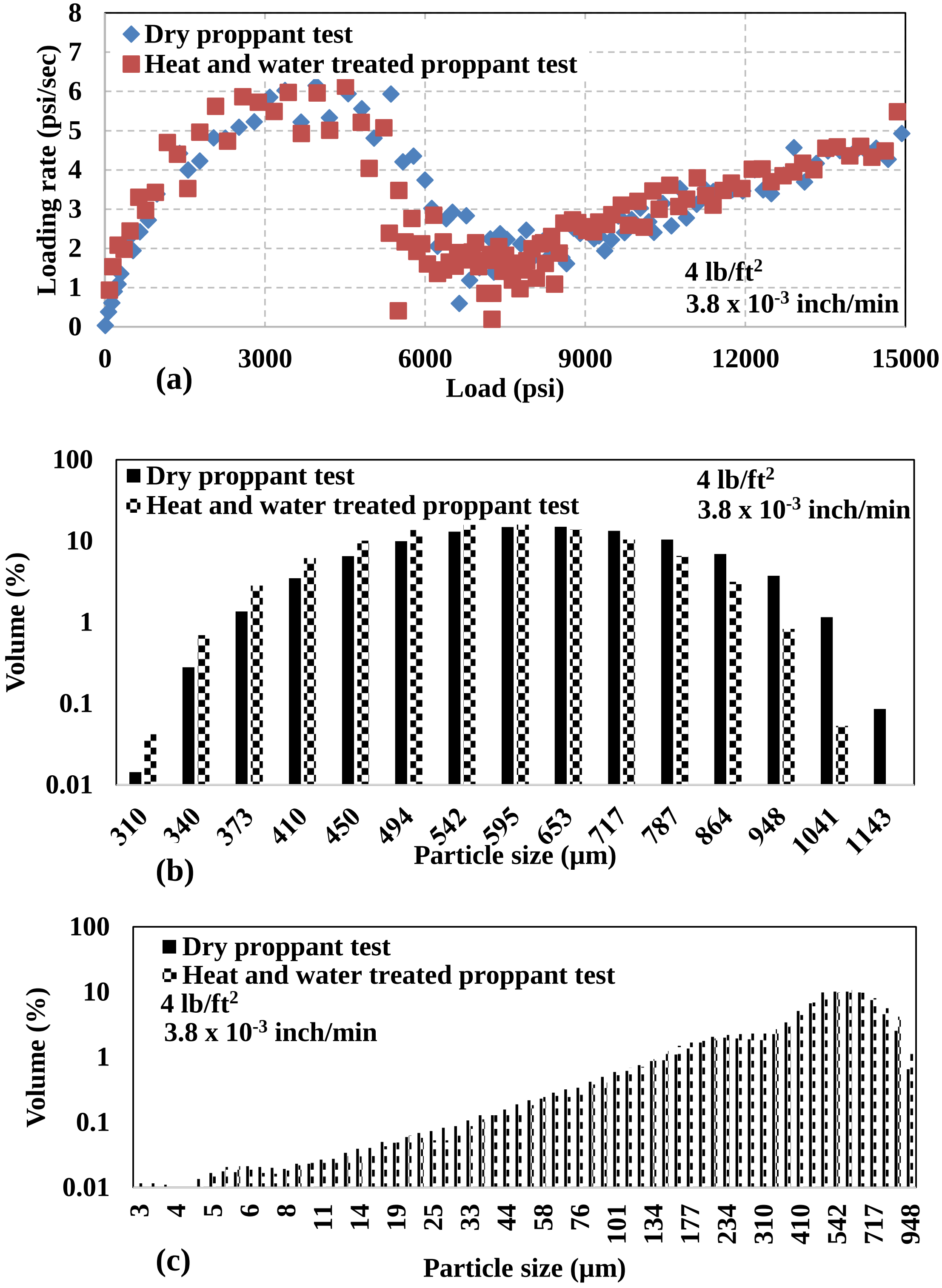

Figure 76: For concentration of 4 lb/ft^2, comparison of treated and dry proppant test responses for: (a) loading rate as function of time (b) particle size analysis at 5000 psi and (c) particle size analysis at 9000 psi.

4.5 Summary

Observations from study of effects of saturation and pre-test treatment:

	Effects of	**Observations from**	
		Load/AE data	**Microscope images/Particle size analysis**
1)	**Saturation**	Load/AE data is inconclusive	• Images show few particles being crushed. Compaction trend different from dry tests. • Particle size analysis show crushing is similar to dry tests
2)	**Pre-test treatment**	Greater crushing for [1], similar crushing for [4] when compared to dry tests	Particle size analysis supports inferences from load data

Chapter 5: Conclusions

1. Loading rate and AE rate can be used to determine stress (σ_{crit}) for the onset of grain crushing in dry crush tests; these constitute qualitative indicators. Proppant packs undergoing crushing and subsequent compaction would display the following characteristic response for loading rate and AE rate:
   a. Loading rate peaks, then decreases to a minimum and finally increases at a lower rate than initial increase.
   b. AE rate shows a delayed start, then increases to a peak and finally decreases monotonically.
2. σ_{crit} can aid in comparing different proppant types and concentrations when tests are conducted dry. Concentration reduction from 4 lb/ft^2 to 1 lb/ft^2 significantly reduces σ_{crit} by a factor of 2 for 20/40 mesh dry Ottawa sand.
3. Images (for dry crush tests using a flat-surface piston) show 20/40 mesh Ottawa sand crushed uniformly at 1 lb/ft^2; while at 4 lb/ft^2, grains crushed non-uniformly and preferentially at the steel-proppant interface. We also conclude that lower proppant (Ottawa sand) concentration (1 lb/ft^2) experiences greater compaction by 3.7% and greater percentage decrease in porosity by 8.3%.
4. Four different proppants were tested dry at 2 lb/ft^2 to determine dependence of σ_{crit} on proppant type.

Critical pressure	Proppant type			
	Carbo NRT	Ottawa sand	CarboHSP	CarboProp
σ_{crit} (psi)	5000	4000	14000 - 14500	14000 - 14500

5. Loading rate from dry crush tests conducted to study effects of fracture width modulation show that (20/40 mesh) Ottawa sand at 1 lb/ft^2 undergoes crushing relatively easily for the curved piston compared to flat-surface piston, and particle size analyses confirms this. For 4 lb/ft^2, loading rate shows that pack undergoes similar crushing for curved and flat-surface pistons; the particle size distribution confirms this.
6. Water saturated (20/40 mesh) Ottawa sand pack at 4 lb/ft^2 compacts significantly between 2000 and 5000 psi as the introduction of water reduces frictional resistance at grain to grain contacts causing to a more dense packing without grain crushing. However, dry (20/40 mesh) Ottawa sand pack at 4 lb/ft^2 does not undergo significant compaction between 2000 and 5000 psi. We observe that dry pack at 4 lb/ft^2 undergoes synchronous crushing and compaction when Ottawa sand starts to crush at 5500 psi.
7. Loading rate from tests conducted to study pre-test treatment effects show that heat and water treated (20/40 mesh) Ottawa sand at 1 lb/ft^2 undergoes crushing relatively easily compared to untreated proppant, and particle size analyses confirms this. For 4 lb/ft^2, loading rate shows that pack undergoes similar crushing for treated and untreated proppant; the particle size distribution confirms this.

Application to the Industry

1. Fracture conductivity can degrade over time through several mechanisms. Proppant crushing, in bulk, controls flow behavior and compaction of these packs. Compaction at realistic field conditions can be incorporated in reservoir simulation models to

estimate the time dependence of fracture conductivity and production more accurately.

2. Simulation models predict production based on simple permeability models considering fluid flow from reservoir to these thick proppant packs. However, images (for dry crush tests using flat-surface piston) showed 20/40 mesh Ottawa sand at 4 lb/ft^2 crushed grains crushed non-uniformly and preferentially at steel-proppant interface. The dense zones (known as compaction bands) will act as barrier to fluid flow from reservoir to the fracture. Issen and Rudnicki, (2001), and Aydin and Ahmadov, (2009) have observed similar compaction band occurrence in highly porous sandstones. Aydin and Ahmadov, (2009) concluded that the porosity and permeability of the compaction band was significantly lower than the native rock in aeolin sandstones. Thus, simulation model incorporating permeability of the compaction bands would yield production more accurately. This “banding” might reduce the apparent skin calculated for a completion.

3. We observe that concentration reduction from 4 lb/ft^2 to 1 lb/ft^2 significantly reduces σ_{crit} by a factor of 2 for dry 20/40 mesh Ottawa sand. The reason for influence of proppant pack on σ_{crit} is that a higher proppant concentration will distribute the stress among a greater number of grains in comparison to lower proppant concentration and change the pack response. However, we are limited by fracture width in the field which gives rise to the question whether smaller mesh particles would allow better stress distribution across greater number of particles than larger mesh particles?

4. Proppant crushing, in field, can be interpreted as skin while performing rate transient analysis. This analysis monitors time dependence of proppant's performance and allows to alter proppant type and concentration to improve well deliverability for the next well completion.

References

1. *API RP 56, Recommended Practices for Testing Sand Used in Hydraulic Fracturing Operation*. 1995. Washington, DC: API.

2. *ASTM C1239-07, Standard Practice for Reporting Uniaxial Strength Data and Estimating Weibull Distribution Parameters for Advanced Ceramics*. 2007. Pennsylvania: ASTM International. http://dx.doi.org/10.1520.C1239-07.

3. Aydin, A. and Ahmadov, R. 2009. Bed-parallel compaction bands in aeolian sandstone: Their identification, characterization and implications. *Tectonophysics* **479** (3–4): 277-284. http://dx.doi.org/10.1016/j.tecto.2009.08.033.

4. Beckman Coulter. 2011. LS 13 320 Laser Diffraction Particle Size Analyzer. Beckman Coulter, Brea, California.

5. Berg, R.R. 1970. Method for Determining Permeability from Reservoir Rock Properties. *Trans., Gulf Coast Association of Geological Societies* **20**: 303-335.

6. Brace, W.F. 1978. Volume changes during fracture and frictional sliding: a review. *Pure Applied Geophysics* **116**: 603-614.

7. Damani, A. 2013. Acoustic Mapping And Fractography of Laboratory Induced Hydraulic Fractures. MS Thesis, University of Oklahoma, Norman, Oklahoma.

8. Damani, A. 2015. Effect of Fluid Saturation on Fracture Propagation in Tennessee sandstone. Presented at the Unconventional Shale Gas Consortium, University of Oklahoma, Norman, Oklahoma.

9. David, C., Menendez, B. and Bernabe, Y. 1998. The mechanical behavior of synthetic sandstone with varying brittle cement. *International Journal of Rock Mechanics and Mining Science* **35** (6): 759–770.

10. den Brok, S., David, C., Bernabé,Y. 1997. Preparation of synthetic sandstones with variable cementation for studying the physical properties of granular rocks. Comptes Rendus de l'Académie des Sciences - Series IIA - Earth and Planetary Science **325** (7):487-492. http://dx.doi.org/10.1016/S1251-8050(97)89866-7.

11. Duenckel, R., Conway, M. W., Eldred, B., and Vincent, M. C. 2012. Proppant Diagenesis--Integrated Analyses Provide New Insights into Origin, Occurrence, and Implications for Proppant Performance. *SPE Prod & Oper* **27** (2). http://dx.doi.org/10.2118/139875-PA.

12. Freeman, E. R., Anschutz, D. A., Rickards, A. R., and Callanan, M. J. 2009. Modified API/ISO Crush Tests With a Liquid-Saturated Proppant Under Pressure Incorporating Temperature, Time, and Cyclic Loading: What Does It Tell Us?

Presented at SPE Hydraulic Fracturing Technology Conference, The Woodlands, Texas, 19-21 January. SPE-118929-MS. http://dx.doi.org/10.2118/118929-MS.

13. Gallagher, J. J., Friedman, M., Handin, J. and Sowers, G. M. 1974. Experimental studies relating to microfracture in sandstone. *Tectonophysics* **21**: 203–247.

14. Ghosh, S., Rai, C. S., Sondergeld, C. H., and Larese, R. E. 2014. Experimental Investigation of Proppant Diagenesis. Presented at SPE/CSUR Unconventional Resources Conference – Canada, Calgary, Alberta, Canada, 30 September–2 October. SPE-171604-MS. http://dx.doi.org/10.2118/171604-MS.

15. Guo, J., and Liu, Y. 2012. Modeling of Proppant Embedment: Elastic Deformation and Creep Deformation. Presented at PE International Production and Operations Conference & Exhibition, Doha, Qatar, 14-16 May. SPE-157449-MS. http://dx.doi.org/10.2118/157449-MS.

16. Howard, G. C. and Fast, C. R. 1970. *Hydraulic fracturing*, first edition. New York: Henry L. Doherty Memorial Fund of AIME.

17. Irwin, G.R. 1958. *Fracture*. Berlin: Handbuck der Physik, second edition, Flugge, Springer-Verlag.

18. *ISO 13503-2:2006, Measurement of Properties of Proppants used in Hydraulic Fracturing and Gravel-Packing Operations*. Geneva, Switzerland: ISO.

19. Issen, K. A. 2000. Conditions for Localized Deformation in Compacting Porous Rocks. Ph. D. thesis. Northwestern University, Evanston, IL.

20. Issen, K. A., and Rudnicki, J. W. 2001. Theory of compaction bands in porous rocks. *Physics and Chemistry of the Earth* Part A **26**: 95–100.

21. Karastathis, A. 2007. Petrophysical Measurements on a Tight Gas Shale. MS Thesis, University of Oklahoma, Norman, Oklahoma.

22. Kassis, S. M., and Sondergeld, C. H. 2010. Gas Shale Permeability: Effects of Roughness, Proppant, Fracture Offset, and Confining Pressure. Presented at International Oil and Gas Conference and Exhibition in China, Beijing, China. SPE-131376-MS. http://dx.doi.org/10.2118/131376-MS.

23. LaFollette, R. F., and Carman, P. S. 2010. Proppant Diagenesis: Results So Far. Society of Petroleum Engineers. Presented at SPE Unconventional Gas Conference, Pittsburgh, Pennsylvania, 23-25 February. SPE-131782-MS. http://dx.doi.org/10.2118/131782-MS.

24. Lawn, B. 1993. *Fracture of Brittle Solids*, second edition. Cambridge: Cambridge University Press.

25. Lee, D. S., Elsworth, D., Yasuhara, H., Weaver, J., & Rickman, R. 2009. An Evaluation of the Effects of Fracture Diagenesis On Fracture Treatments: Modeled Response. Presented at 43rd U.S. Rock Mechanics Symposium & 4th U.S. - Canada Rock Mechanics Symposium, Asheville, North Carolina, 28 June-1 July. ARMA-09-104.

26. Palisch, T. T., Duenckel, R. J., Bazan, L. W., Heidt, J. H., and Turk, G. A. 2007. Determining Realistic Fracture Conductivity and Understanding its Impact on Well Performance - Theory and Field Examples. Presented at SPE Hydraulic Fracturing Technology Conference, College Station, Texas, 29-31 January. SPE-106301-MS. http://dx.doi.org/10.2118/106301-MS.

27. Palisch, T. T., Duenckel, R. J., Chapman, M. A., Woolfolk, S., and Vincent, M. C. 2009. How to Use and Misuse Proppant Crush Tests -- Exposing the Top 10 Myths. Presented at SPE Hydraulic Fracturing Technology Conference, The Woodlands, Texas, 19-21 January. SPE-119242-MS. http://dx.doi.org/10.2118/119242-MS.

28. Palisch, T. 2015. Putting it All Together – Proppant selection, Conductivity and Their Inpact on Well Performance. Presented at University of Oklahoma, Norman, Oklahoma.

29. Pearson, C. M., Griffin, L., and Chikaloff, J. 2014. Measuring Field Supplied Proppant Conductivity: Issues Discovered in an Operator. Presented at SPE Hydraulic Fracturing Technology Conference, The Woodlands, Texas, 4-6 February. SPE-168641-MS. http://dx.doi.org/10.2118/168641-MS.

30. Raysoni, N., Pinto, M., and Kothamasu, R. 2013. Insights into the Relationship between Single Grain and API/ISO Crush Strength when applied to Proppants with or without Diagenesis. Presented at 47th U.S. Rock Mechanics/Geomechanics Symposium, San Francisco, California, 23-26 June. ARMA-2013-171.

31. Retsch GmbH Haan. 2015. Sieve Analysis. Expert Guide, Retsch, Haan, Germany.

32. Schubarth, S., and Milton-Tayler, D. 2004. Investigating How Proppant Packs Change Under Stress. Presented at SPE Annual Technical Conference and Exhibition, Houston, Texas, 26-29 September. SPE-90562-MS. http://dx.doi.org/10.2118/90562-MS.

33. Shukla, P. 2013. Nanoindentation Studies on Shales. MS Thesis, University of Oklahoma, Norman, Oklahoma.

34. Simo, H., Sondergeld, C., and Pournik, M. 2013. Proppant Crush Test: A New Approach. Presented at SPE Production and Operations Symposium, Oklahoma City, Oklahoma, 23-26 March. SPE-164506-MS. http://dx.doi.org/10.2118/164506-MS.

35. Talwani, P., Nur, A. and Kovach, R. L. 1973. Compressional and shear wave velocities in granular materials to 2.5 kilobars. *Journal of Geophysical Research* **78**: 6899-6909.

36. Tang, C. and Hudson, J. 2010. In *Rock Failure Mechanisms: Explained and Illustrated*, ed. C. Tang and J. Hudson, Chap. 19, 273-295. Boca Raton, FL: CRC Press.

37. Weaver, J. D., Parker, M., van Batenburg, D. W., and Nguyen, P. D. 2007. Fracture-Related Diagenesis May Impact Conductivity. *SPE J* **12** (3). SPE-98236-PA. http://dx.doi.org/10.2118/98236-PA.

38. Weaver, J. D., Rickman, R. D., Luo, H., and Logrhy, R. 2009. A Study of Proppant Formation Reactions. Presented at SPE International Symposium on Oilfield Chemistry, The Woodlands, Texas, 20-22 April. SPE-121465-MS. http://dx.doi.org/10.2118/121465-MS.

39. Wong, T.-F., David, C., and Menéndez, B. 2004. In *Mechanical compaction*, Vol. 89, ed. Y. Guéguen and M. Boutéca, Chap. 2, 55-114. International Geophysics, Academic Press. http://dx.doi.org/10.1016/S0074-6142(03)80018-9.

40. Wyatt, W. 2015. Application of Nanoindentation for Creep Properties and Saturation Effects. MS Thesis, University of Oklahoma, Norman, Oklahoma.

41. Zhang, J., Wong, T.-F. and Davis, D. M. 1990. Micromechanics of pressure-induced grain crushing in porous rocks. *Journal of Geophysical Research* **95**: 341–352.

42. Zoback, M. D. and Byerlee, J. D. 1976. Effect of high-pressure deformation on permeability of Ottawa Sand. *American Association of Petroleum Geologists Bulletin* **60**: 1531–1542.